THERMOMECHANICAL PROCESSING OF MICROALLOYED STEELS: EXPERIMENTS AND MODELLING

BY

SHENGLONG LIANG

B. E., UNIVERSITY OF SCIENCE & TECHNOLOGY BEIJING, 2010
M. A. SC., MCMASTER UNIVERSITY, 2012

A THESIS SUBMITTED TO THE SCHOOL OF GRADUATE STUDIES
IN PARTIAL FULFILLMENT OF THE REQUIREMENTS FOR
THE DEGREE OF
DOCTOR OF PHILOSOPHY

JANUARY 2020

DOCTOR OF PHILOSOPHY (2020) **MCMASTER UNIVERSITY**
(MATERIALS SCIENCE & ENGINEERING) **HAMILTON, ONTARIO**

TITLE: THERMOMECHANICAL PROCESSING OF MICROALLOYED STEELS: EXPERIMENTS AND MODELLING

AUTHOR: SHENGLONG LIANG, M. A. SC.

SUPERVISOR: PROF. HATEM S. ZUROB

NUMBER OF PAGES: XXI, 150

ABSTRACT

Recovery, recrystallization, grain growth and precipitation constitute the fundamentals of thermomechanical controlled processing (TMCP) of microalloyed steels. In-depth understanding of these phenomena is indeed needed. In this work, the individual components and some of the potential mutual interactions have been investigated deliberately.

The effect of alloying elements of Mn, Si, and Al on recovery and recrystallization has been systematically studied by conducting the stress relaxation tests on binary Fe-0.1%C and ternary Fe-0.1%C-X alloys. The effect of temperature on recovery kinetics was also investigated. The effects were considered by fitting the recovery model through the activation volume term. Higher temperature or lower solute content will accelerate the recovery process and then facilitate the onset of recrystallization.

NbC precipitation behavior has been investigated using a nickel-based model alloy, having samples deformed at both room temperature and elevated temperature and subjected to annealing at 700°C for different times, in order to elucidate the stages of nucleation, growth and coarsening for precipitation. The microstructures preserved by water quenching were examined using transmission electron microscopy (with both metal foil and carbon replica specimens). Results from mechanical response and microstructural evolution are linked and discussed. The precipitate number density and size evolution show good agreements with predictions from a classical strain-induced precipitation model.

The in-situ laser-ultrasonics measurement of C-Mn steels provides a unique way to evaluate grain size evolution during TMCP, for different strains of 0.15, 0.25 and 0.35, at 950°C and 1050°C. Effects of temperature and strain on recovery, recrystallization and grain growth have been covered and elucidated. Higher strains facilitate the onset of recrystallization and grain size refinement. However, higher temperatures only shorten the onset of recrystallization but lead to larger grain size. The effect of microalloying element of Nb on softening kinetics was also investigated by comparing C-Mn/C-Mn-Nb steels at the same conditions. The solute drag effect of Nb can be seen by the onset-delays of recrystallization and larger grain sizes. The laser-ultrasonics results can match well with stress relaxation measurements. The in-situ grain size evolution data has given the possibility to develop robust thermomechanical processing (TMP) models combining deformation, recovery, precipitation, recrystallization and grain growth. The application and validation of the TMP models have been attempted and remain ongoing.

CONTENTS

LISTS OF FIGURES

LIST OF TABLES

LIST OF SYMBOLS

α	*Constant in Eqs. (1-32) & (3-5) ~ 1.05.*
α_T	*Constant in Eqs. (1-45), (2-3) & (5-3) ~ 0.15.*
α'	*Geometric constant for grain growth.*
a^*	*Activation distance.*
a_0	*Lattice parameter of austenite.*
$a_{[i]}$	*Activity of component* i.
b	*Burgers vector.*
β^*	*Atomic impingement rate.*
C	*Bulk concentration of solutes.*
C_j	*Solute j concentration.*
C_M^r	*Solute M concentration in equilibrium with precipitates of radius r.*
$C_M^{27/23\ r}$	*Solute M concentration in equilibrium with precipitates of radius 27/23 r.*
C_M^P	*Solute M concentration of precipitates.*
C_M^{eq}	*Solute M concentration in equilibrium with planar precipitates.*
D	*Grain size.*
D_0	*Original grain size.*
D	*Diffusion coefficient.*
D_{cb}	*Diffusion coefficient crossing grain boundary.*
D_{eff}	*Effective diffusion coefficient.*
D_{pipe}	*Pipe diffusion coefficient.*
D_{bulk}	*bulk diffusion coefficient.*
δ	*Grain boundary width.*
E	*Elastic modulus.*
E_b	*Binding energy of solute to grain boundary.*
ϵ_i^j	*Wagner interaction parameters.*

ε	*Strain.*
ε_e	*Elastic strain.*
ε_p	*Plastic strain.*
ε_{tot}	*Total strain.*
$\dot{\varepsilon_p}$	*Plastic strain rate.*
$\dot{\varepsilon}$	*Strain rate.*
F	*Force.*
f	*Frequency.*
f	*Volume fraction of precipitates.*
f_i	*Activity coefficient of component* i.
f_{coarse}	*Coarsening function.*
γ	*Surface energy.*
γ_b	*Grain boundary energy.*
$\dot{G}$	*Boundary migration rate.*
ΔG^*	*Critical activation energy for nucleation.*
ΔG_V	*Chemical free energy change in transformation per unit volume.*
$°G_i$	*Standard molar Gibbs free energy of component* i.
GS_{ave}	*Average grain size during recrystallization.*
GS_{rex}	*Recrystallized grain size.*
GS_{unrex}	*Equivalent grain size of unrecrystallized volume.*
k_s	*Equilibrium constant.*
k_b	*Boltzmann constant.*
K_{ad}	*Fitting parameter for subgrain growth.*
l	*Obstacle spacing.*
l_j	*Dislocation jog spacing.*
M	*High angle grain boundary mobility.*
M_i	*Intrinsic mobility of pure metals.*
M_T	*Taylor factor.*

N_0	*Number of atoms per unit volume.*
$\dot{N}$	*Recrystallization nucleation rate.*
N	*Number density of precipitates.*
N_c	*Instantaneous maximum precipitation nucleation sites.*
N_{rex}	*Number of recrystallized nuclei.*
N_{tot}	*Total precipitation nucleation sites.*
ω	*Constant in Eqs. (1-74) & (1-75) & (5-12) & (5-13) ~1.58.*
P	*Pressure.*
Q	*Apparent activation energy for hot deformation.*
Q_{rex}	*Apparent activation energy for recrystallization.*
r	*Precipitate radius.*
r^*	*Critical radius for precipitation nucleation.*
$r_c(t)$	*Critical subgrain size.*
$\overline{r(t)}$	*Average subgrain size.*
R_{core}	*Dislocation core radius.*
R	*Austenite grain radius.*
R	*Gas constant.*
$\bar{R}$	*Mean grain radius.*
R_{cr}	*Critical grain size in grain growth.*
ρ	*Dislocation density.*
σ	*Stress.*
σ_i	*Internal stress.*
σ_y	*Yielding stress.*
σ_{rec}	*Stress of recovered material.*
σ_{rex}	*Stress of recrystallized material.*
t	*Time.*
τ	*Incubation time for precipitate nucleation.*
T	*Absolute temperature.*

μ_i	*Chemical potential of component* i.
μ	*Shear modulus.*
U_0	*Self-diffusion activation energy.*
$U(\sigma_i)$	*Stress-alleviated activation energy.*
υ	*Boundary migration velocity.*
$\bar{\upsilon}$	*Average dislocation migration velocity.*
υ_D	*Debye frequency.*
V	*Volume of transformed nuclei.*
V	*Activation volume.*
V_P	*Molar volume of precipitates.*
χ	*Normalized subgrain size.*
χ_c	*Critical normalized subgrain size.*
X	*Recrystallization volume fraction.*
Z	*Zeldovich factor.*
Z	*Zener-Hollomon parameter.*

ACKNOWLEDGEMENT

Being always grateful, I would like to start by thanking the steel research centre (SRC) managed by Mr. John Thomson, within which our collaborative research project on the thermomechanical processing, sponsored by Evraz North America and Stelco, is launched and boosted. Discussions with Dr. Tom (Tihe) Zhou, Dr. Laurie Collins, Dr. Michael Gaudet are much appreciated. Frequent interactions with Dr. Nicolas Legrand from ArcelorMittal East Chicago are undoubtedly invaluable, especially for the laser ultrasonic data that provided a unique way to modify and guide our model development.

Experiments were mainly conducted at CanmetMaterials and characterized at the Canadian Centre for Electron Microscopy (CCEM) at McMaster University. I appreciate Dr. Fateh Fazeli and Mrs. Marta Aniolek greatly for conducting the hot-deformation and stress relaxation tests. The characterization contributions from CCEM staffs such as Dr. Andreas Korinek, Dr. Carmen Andrei, Dr. Brian Langelier, Mr. Andy Duft, Mr. Chris Butcher and Mr. Jhoynner Martinez are sincerely appreciated. I also want to thank Dr. Xiang Wang, a research associate in our group, for part of the amazing TEM work.

Scientific discussions and learnings are invaluable at McMaster University. I appreciate Prof. David Embury, Prof. Gary Purdy, Prof. Yves Bréchet and Prof. Jeffery Hoyt for stimulating discussions and emails. I also would like to thank Prof. Dmitri Malakhov, Prof. David Wilkinson and Prof. Gianluigi Botton for instructing fantastic courses. The terms as a teaching assistant for Prof. Dmitri Malakhov in three consecutive years are memorable. Postdocs at McMaster such as Dr. Hamid Azizi, Dr. Abu Khaled, Dr. Bosco Yu and Dr. Mohamad Nabeel are also quite helpful.

Technical and administrative assistances are acknowledged with my sincere gratitude to Mrs. Samantha Kandilas, Ms. Mary-Anne Bechamp, Ms. Chelsea Gregory, Mr. Edward McCaffery, Mr. Doug Culley and Dr. Xiaogang Li. They are incredibly nice department staffs who are turning MSE our home. Uncountable scientific and technical discussions with Dr. Li are valuable. And I still remember the superman-pose encouragement from Mary-Anne before my final oral examination.

Mental well-being matters. The thesis would not have been accomplished without support from my family and friends (both in China and Canada). I am so content that each of you is so encouraging and considerate. You all leave me a comfort zone so that I was able to focus on solving academic problems (it is painful dealing with them but fulfilling after). I would like to give my special thanks and wishes to my uncle. I hope and believe that he will like this manuscript.

Eventually, as the most important, I am indebted to my supervisor Prof. Hatem S. Zurob, the department Chair. I am very thankful for his consistent guidance and generous care during all three years of my Ph.D studies. He is such a knowledgeable researcher in metallurgy with gracious personality. Certainly, I will cherish every piece of those learning memories with him, probably for the rest of my life. I wish him a better and more successful career.

The following was inserted intentionally after the defense, when a state of emergency Ontario had been declared due to the ruthless spreading of the coronavirus (COVID-19).

A pandemic of the coronavirus was announced by the World Health Organization (WHO) on March 11th, the day right before the thesis defense, and the university has suspended all major activities on campus from March 13th to minimize the risks to the coronavirus for the faculty and students. I would sincerely like to thank all (my supervisor, the supervisory committee, Dr. Colin Scott, Dr. Sumanth Shankar and many graduate fellows and friends) for coming to my final oral examination, during such a frightening time. I also want to thank my friends/roommates helping me with most of my living necessities. The year 2020 is doomed to be special since my back visit to hometown in China this January. I greatly appreciate everyone helping each other, fighting against the coronavirus, as a family.

The coronavirus is the enemy of the entire human beings, no matter where it originates or outbreaks. The only thing that we should do is to work collaboratively worldwide, like our clinic doctors and nurses curing patients or medical scientists working tirelessly on vaccines. We all should thank them sincerely. And this is the meaning of conducting scientific research for unveiling what we do not know or what to see. Sincerely, I hope that everyone stays healthy and we will get through this together for victory.

Behind all the greatness is suffering.

CO-AUTHORSHIP STATEMENT

The current research work was conducted within the steel research centre (SRC) framework at McMaster University, which renders excellent interactive collaborations with R&D units such as ArcelorMittal East Chicago, Stelco, Evraz and CanmetMATERIALS. However, major contributions to the research work enclosed were made by the author (Shenglong Liang), under the fabulous supervision of Prof. Hatem S. Zurob.

For Chapter 2, the binary/ternary alloys were arc-melted and prepared by the author and Mr. James Garret. The stress relaxation tests were conducted by Dr. Fateh Fazeli at CanmetMATERIALS, a co-author of the paper. The post data analysis and mathematical modeling, as well as the original manuscript write-up, were accomplished by the author.

For Chapter 3, the author owned major contributions to the work, including the design of experiment, investigation methods (tensile test, microhardness and TEM), the model simulation and the original manuscript. Dr. Xiang Wang, a co-author of the precipitation paper, contributed partially to the TEM work.

For Chapter 4, the experiment was proposed by the author and the hot deformation was conducted by Dr. Fateh Fazeli. The microhardness test, microstructure characterizations (OM and TEM) and the modelling work, as well as the original manuscript, were accomplished by the author. Dr. Xiang Wang contributed partially to the TEM work.

For Chapter 5, the laser-ultrasonics (LUS) measurements of grain size were conducted at National Research Council Canada (NRC) by Dr. Daniel Lévesque. The author contributed to the model simulation work and the write-up of the original manuscript. Dr. Nicolas Legrand reviewed the manuscript and partially contributed to the discussion part.

CHAPTER 1: Introduction

1.1 Overview

According to the American Iron & Steel Institute (AISI), steel can be categorized into four basic groups based on the chemical compositions: carbon steel, alloy steel, stainless steel and tool steel. High-strength low-alloy steel (HSLA) is a type of alloy steels that provides better mechanical properties or greater resistance to corrosion compared to carbon steel. Applications of HSLA steels include oil and gas pipelines, heavy-duty highway and off-road vehicles, construction and farm machinery, industrial equipment, storage tanks, mine and railroad cars, barges and dredges, snowmobiles, lawn mowers, and passenger car components. Among the HSLA steels is the microalloyed steel exhibiting an equivalent high strength without increasing carbon and/or manganese contents [1].

Basically, microalloyed steels are developed by adding less than 0.1wt% of alloying elements, such as aluminium, niobium, titanium and vanadium. These microalloying elements are added, either singly or in combination, to attain yield strengths up to two or three times that of plain carbon-manganese steels, by forming relatively stable carbides, nitrides or carbonitrides [2]. The formation of these second phases may refine the austenite grain size and provide precipitation hardening. During the hot rolling of alloy steels, the microalloying elements in solution will segregate to the grain boundary and then slow down the migration velocity; on the other hand, strain-induced precipitate MX (M = Al, Nb, Ti, V; X = C, N) will form and exert extra pinning force to the high/low angle grain boundary migration. The softening kinetics will be stagnated, leading to a refined microstructure. Therefore, the alloy is strengthened through grain refinement and precipitation hardening.

However, interactions between recovery, recrystallization, grain growth, precipitation and solute drag effects are complicated [3-7]. Recovery and recrystallization are competing mechanisms which consume the stored energy (i.e. dislocations) of the deformed matrix.

The decreasing density of dislocations renders less nucleation sites available for precipitation; at the same time, precipitates exert pinning forces to the formation of subgrains and the migration of high/low angle grain boundaries. Moreover, precipitation removes solutes such as niobium and/or titanium from solid solution and thus reduces the solute drag effect of these microalloying elements on grain boundary migration [8]. Scientifically speaking, these interactions are indeed complicated and need critical assessments before the implementation of modelling during a single pass rolling. For the multi-pass scenario, the modelling comes with much more complication. The resultant features from the previous pass will be taken as initial inputs for the current pass such as austenite grain size, recrystallization fraction, dislocation density, precipitation distributions, effective solutes in solution, etc. In the case of incomplete recrystallization, for example, recrystallized and unrecrystallized regions are distinctive and should be treated properly. Therefore, the current work aims to put all together and make precise predictions of the rolling process for industrial production.

1.2 Literature review

1.2.1 TMCP

Thermomechanical controlled processing (TMCP) is the most cost-effective way to obtaining grain refinement that is exclusive to improve strength and toughness of steels simultaneously [9]. Typically, there are five main processing stages including reheating, soaking, roughing, finishing and controlled cooling. A typical rolling mill configuration can be found in Appendix I. The previous heat treatment will always influence the later ones. Thus, the optimization of the processing parameters is always anticipated.

The major heat treatment steps are illustrated below:

- Reheating (+ soaking): Reheating is the first step of heat treatment. For the hot rolling of HSLA steel, the as-received steel is heated up to a temperature between 1250°C and 1300°C (austenitization), in order to modify the microstructure and, meanwhile, to dissolve the microalloying precipitates so that all the solutes stay in solution. Soaking means the homogenization of temperature throughout the whole slab. The time for soaking is an important parameter to be controlled.

- Roughing: After a period of soaking, the slab is cooled down to temperatures from 1150°C to 1050°C [10]. Several passes and relatively high reductions are applied to break down the as-cast microstructure and remove heterogeneities of the microstructure. The entry temperature and reduction for each pass can be of importance to the final austenite grain size before transferred to the finishing rolling stage.
- Finishing: The grain size is preliminary refined and ready for pancaking and strain accumulation at this stage. This is the temperature range within which complete static recrystallization no longer takes place between rolling passes. Deformation in the low temperature austenite region (between the non-recrystallization temperature T_{nr}[1] and the austenite transformation temperature A_{r3}) leads to the strain retention, which is accompanied by the formation of pancaked grains and deformation bands. Consequently, increased numbers of nucleation sites are made available for the γ to α transformation. This further promotes the formation of a fine grained microstructure, fulfilling the requirements for both strength and toughness [9].
- Controlled cooling: As can be visualized directly in Fig. 1-1, ferrite and perlite microstructures are produced with slow cooling rate. Accelerated cooling will give bainitic microstructures or even with martensitic constituents, achieving an enhanced yield strength and probably a reduced ductility of the component. The undercooling of austenite due to accelerated cooling can further refine the microstructures, since more nuclei are being provided. The cooling process is essentially determined by the requirements of the final products from customers.

---

[1] T_{nr} or Non-recrystallization Temperature: an industry-concept temperature below which complete static recrystallization no longer takes place and strain accumulation starts (stored energy retained). It depends on factors such as alloy chemistry, pass strain, strain rate and interpass time.

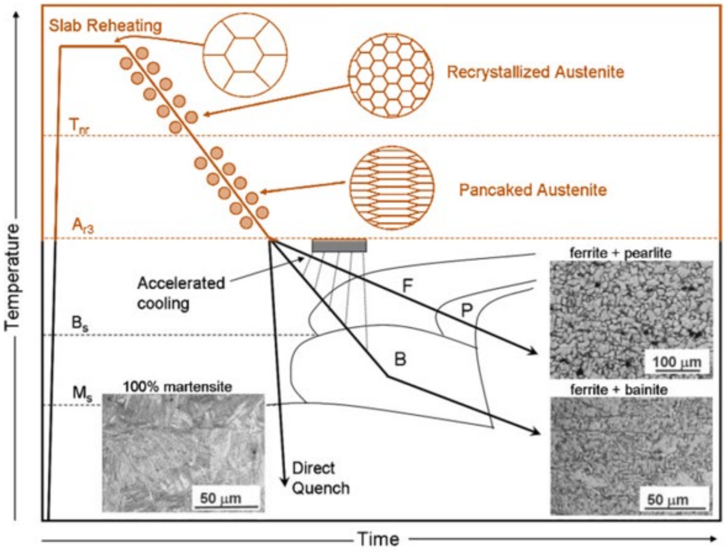

Fig. 1-1: Schematic diagram of thermomechanical controlled processing (TMCP) and microstructures that result upon phase transformations during cooling [9]. The diagram was re-decorated with an emphasis on hot rolling.

1.2.2 TMP models

In order to capture and predict the evolution of microstructure and mechanical properties during the TMCP process, much research has been devoted to try to understand the basic physics, either experimentally [9, 11-14] or by physical metallurgy process simulations [3-5, 8, 15-20]. As we know, recrystallization kinetics, including foregoing recovery kinetics and subsequent grain growth, is believed to be the essential and fundamental part of the modelling work. In the 1970s, Sellars and co-workers [11, 15] developed semi-empirical models which can describe the microstructure evolution during hot rolling of steels. Based on explicitly conducted experiments, their models were able to take into consideration the effect of alloy chemistry, strain, strain rate, grain size and so on, and they were widely adopted and further expanded by many other researchers worldwide such as O. Kwon [21], J. J. Jonas [22] and P. D. Hodgson [16, 17], for more than two decades. However, the solute drag effect of niobium had to be incorporated with a new equation (e.g. by Hodgson [17]) and the semi-empirical models were not sufficiently accurate for some applications. Therefore, a more physically-based model was anticipated at that time.

Almost at the end of last century, Humphreys [19, 20] analyzed the growth and stability of cellular microstructures, taking account of the orientation dependence of boundary energies and mobilities, and developed a simple unified theory for continuous and discontinuous recovery, recrystallization and grain growth. An important type of recrystallization mechanism is through the strain-induced boundary migration (SIBM), in which part of a pre-existing grain boundary bulges into the adjacent substructure, leaving a dislocation-free recrystallized region behind the migrating boundary. Based on SIBM, Zurob et al [3, 4, 8] coupled models for precipitation, recovery and recrystallization in order to describe the microstructural evolution behavior of industrial alloys.

The current work is based on the models by Zurob et al [3, 4, 8] and followed with further developments in several modules by researchers in the group. In the subsequent sections, the physically-based robust TMP models will be generally demonstrated again, with an emphasis on the alloying element effect in the first part (constitutive relation, solute drag effect and precipitation module) and on the basic models in the second part (recovery, recrystallization and grain growth module).

1.2.2.1 Constitutive relations

The prediction of stress-strain curves is crucial to the modelling, since the stored energy will be determined from the curve. At the beginning of the TMP model development, Yoshie's empirical formulation [23] was adopted to calculate the flow stress of Nb added steels, shown as Eq. $(1-1)$:

$$\sigma = 22.7\varepsilon^{0.223}\dot{\varepsilon}^{0.0480}D^{-0.070}\exp(2880/T)\exp(3.01\times Nb) \qquad (1-1)$$

where, σ is the stress in MPa, ε is the strain, $\dot{\varepsilon}$ is the strain rate (s^{-1}), D is the austenite grain size in μm, T is the absolute temperature and Nb is the wt% of Nb in solution. However, only the effect of alloying of Nb was taken into account in Yoshie's formulation, which is not adequate for modern microalloyed steel design, even though the calculated flow stresses can match the experimental data very well [23]. Other alloying elements such as Mn, Si, Al, Mo, Ti and V vary from one alloy to another. Therefore, for a complete consideration, it was replaced with Medina's formulation [24-26] which can predict the flow stress to a very large strain, with two-stage equations:

$$\sigma = B\ [1 - \exp\ (\ -C\varepsilon)]^{m} \qquad (1-2)$$

where, $B(MPa) = \ (9.5326 + 0.6196\ ln\frac{Z}{A})^{2}$;

$C = \ 3.9202\ (\frac{Z}{A})^{0.0592}$;

$m = \ 0.3449\ \exp\ (0.0139\ \sqrt{\frac{Z}{A}})$;

and

$$\Delta\sigma = B'\ (1 - \exp\ [\ -k(\frac{\varepsilon - a\varepsilon_{p}}{\varepsilon_{p}})^{m'}]) \qquad (\varepsilon > a\varepsilon_{p}) \qquad (1-3)$$

where, $B'(MPa) = \ 26.0310\ (\frac{Z}{A})^{0.1351}$;

$k = \ 0.5974\ \exp\ [1.2333\ \left(\frac{Z}{A}\right)^{-0.5}]$;

$m' = \ 1.0901\ \exp\ (0.264\ \sqrt{\frac{Z}{A}})$;

$a = 0.95$.

Here, *Z* is Zener-Hollomon parameter in the mathematic form of hyperbolic sine function, *Q* is the apparent activation energy for hot deformation, which is a function of most major alloying elements, and *A* is the coefficient as a function of carbon and niobium content and apparent activation energy *Q*.

$$Z(s^{-1}) = \dot{\varepsilon}\ \exp\left(\frac{Q}{RT}\right) = A\left(sinh\alpha\sigma_{p}\right)^{n} \qquad (1-4)$$

$$Q(J/mol) = 267000 - 2535wt\%C + 1010wt\%Mn + 33620wt\%Si\ + 35651$$
$$wt\%Mo + 31673wt\%V + 93680(wt\%Ti)^{0.5919} + 70729(wt\%Nb)^{0.5649} \qquad (1-5)$$

$$A(s^{-1}) = [12.197 + 65.590wt\%C - 49.052wt\%Nb] \times \exp(7.076 \times 10^{-5}Q) \qquad (1-6)$$

Some of the experimental and predicted flow stress curves are shown in Fig. 1-2 and it indicates that Medina's formulation is very precise in the prediction of stress-strain curves for microalloyed steels with various deformation conditions labeled in the diagram.

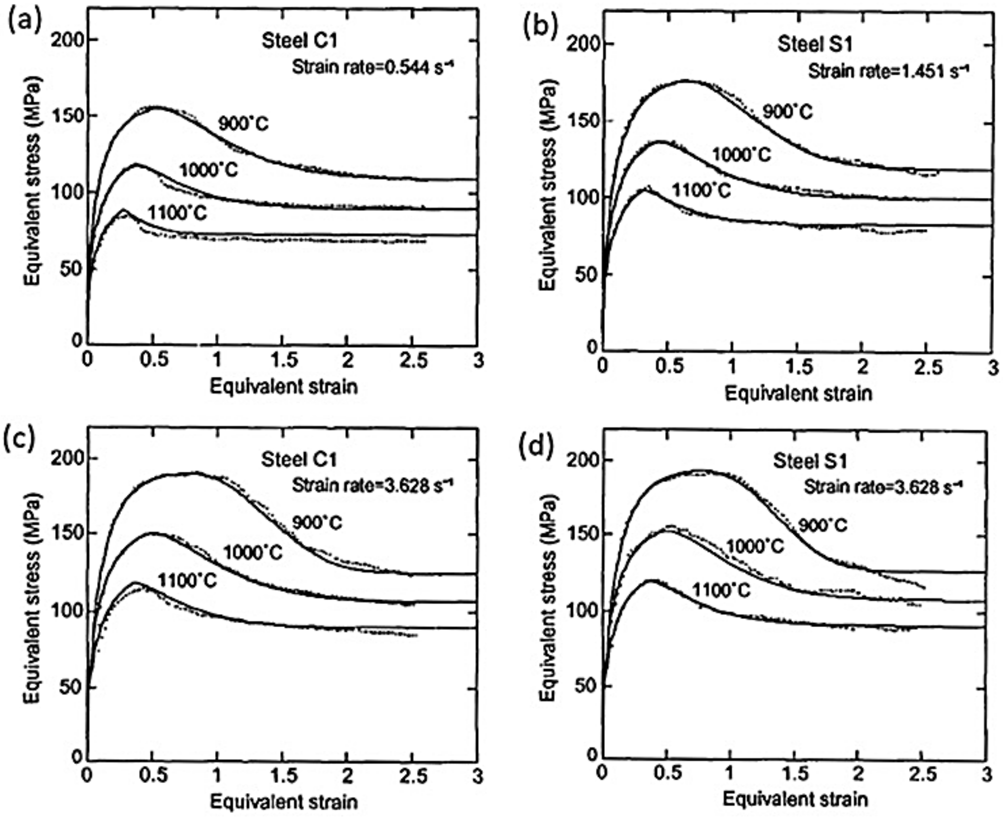

Fig. 1-2: Experimental and predicted flow stress curves for two steels with different deformation temperatures and strain rates. Details such as for the alloy chemistry should be referred to [26].

1.2.2.2 Solute drag effect

As known, the impurities in alloys can never be completely removed practically, and, on the other hand, some elements such as niobium are added on purpose. Impurities will always exist in the steel/alloy making process. The solutes (or impurities) would prefer to occupy defect sites such as grain boundaries/interfaces, i.e. having the tendency of forming segregation. The segregation process is irreversible thermodynamically because of the spontaneous decrease of the total Gibbs free energy of the system.

The segregated solute exerts a force on the migrating grain boundary, which is relative to the diffusivity of the solute and the interaction between the solute and grain boundary. It is usually termed the "Solute Drag Effect". Scientists have already reported the mobility reduction due to small additions of impurities to high purity metals. Lucke and Detert [27] first raised a mathematical treatment of the solute drag effect quantitatively. The recrystallization rate of high purity aluminum can be diminished by several orders of magnitude with very small amounts (0.01%wt) of impurity addition. The solute drag effect has thus received much attention since then and two distinct treatments were developed: the force approach by Cahn [28] in 1962 and the dissipation approach by Hillert [29] in 1976.

Here, Cahn's treatment [28] was adopted as it can be easily incorporated within the JMAK framework, according to Zurob [8]. The high angle grain boundary mobility with impurity additions is given as:

$$\frac{1}{M} = \frac{1}{M_i} + \sum_j \alpha_j C_j \qquad (1-7)$$

where,

$$\alpha_j = \frac{\delta N_0 (k_b T)^2}{E_b D} \left(\sinh\left(\frac{E_b}{k_b T}\right) - \frac{E_b}{k_b T}\right). \qquad (1-8)$$

In Eq. $(1-7)$, M is the mobility of a high angle grain boundary (HAGB), M_i is the intrinsic mobility of pure metals, C_j is the concentration of impurity j in the matrix, and in Eq. $(1-8)$, δ is the width of the grain boundary, N_0 is the number of atoms per unit volume, k_b is the Boltzmann constant, E_b is the solute boundary interaction energy, T is the absolute temperature and D is the average value of the diffusion coefficient in the vicinity of grain boundaries.

1.2.2.3 Precipitation

As mentioned at the beginning, strain-induced precipitation (SIP) of carbide/nitride {MX (M = Al, Nb, Ti, V; X = C, N)} or carbonitride { MC_xN_{1-x} (x is mole fraction of C in the interstitial sublattice)} is of great importance to the austenite grain refinement and strain accumulation in the roughing and finishing stages of microalloyed steels during TMCP. Therefore, the strain-induced precipitation should be investigated systematically, from thermodynamics to kinetics. The details of these two aspects will be presented in the following sections:

1.2.2.3.1 Thermodynamics and solubility product

It is necessary to compute the equilibrium between the austenite and the carbonitride as a reference for precipitation kinetics, because the system always tries to evolve towards this state from its initial non-equilibrium one [30]. As we know, the equilibrium states of carbide and nitride can be evaluated by the equilibrium constant k_s, i.e. the solubility product widely used by metallurgists [2]. For the chemical reaction of $[M]+[X] \Leftrightarrow (MX)$, the solubility product was defined as:

$$k_s = a_{[M]} \cdot a_{[X]} / a_{(MX)} \tag{1-9a}$$

and in a very empirical manner, it is assumed that the activity coefficients are equal to unity. Then,

$$k_s = [M] \cdot [X] / a_{(MX)} \tag{1-9b}$$

where, $[M]$ and $[X]$ are compositions of the solutes in solution in weight percent, "a" means the activity of a component. The temperature dependence of the solubility product is expressed in a condensed form such as [2]:

$$log\, k_s = A - \frac{B}{T} \tag{1-10}$$

The carbonitride (MC_xN_{1-x}) precipitation can be treated as an ideal mixture of carbide (MC) and nitride (MN). And the carbonitride is assumed to be perfectly stoichiometric for simplicity. According to the regular solution sublattice model by Hillert and Stanfasson [31], the molar Gibbs free energy of the carbonitride can be expressed as followed:

$$G_{\mathrm{MC}_x\mathrm{N}_{1-x}} = x°G_{MC} + (1-x)°G_{MN} + RT[xlnx + (1-x)\ln(1-x)] \tag{1-11}$$

where, $°G_{MC}$ and $°G_{MN}$ are the standard molar Gibbs free energies for MC and MN, respectively. These data were already well tabulated previously and can be incorporated to represent the Gibbs free energy curve of the precipitation phase. At this point, the equilibrium state can be obtained with the global minimization of the total Gibbs energy of the system. It is actually about the topic of computational thermodynamics, and the calculation/visualization can be realized by the powerful software, Thermo-Calc [32].

In terms of discussing carbonitrides, as we already know from thermodynamics, the chemical potentials of the carbide and nitride forming the carbonitride can be derived as:

$$\mu_{MC} = °G_{MC} + RTlnx \qquad (1-12)$$

$$\mu_{MN} = °G_{MN} + RTln(1-x) \qquad (1-13)$$

and furthermore, the stoichiometric compounds are in equilibrium with the corresponding solutes in solution and then we have the chemical potential relationships:

$$\mu_{MC} = \mu_M^{\gamma} + \mu_C^{\gamma} \qquad (1-14)$$

$$\mu_{MN} = \mu_M^{\gamma} + \mu_N^{\gamma} \qquad (1-15)$$

$$\mu_i^{\gamma} = °G_i + RTlna_i^{\gamma} \qquad (1-16)$$

where, μ_i^{γ} represents the chemical potential for element, i (M, C, N), and $°G_i$ refers to the infinitely dilute standard state in austenite. Combining Eqs. (1 – 12) to (1 – 16), we have:

$$\Delta°G_{MC} = °G_{MC} - °G_M - °G_C = RT\left[lna_M^{\gamma} + lna_C^{\gamma} - lnx\right] \qquad (1-17)$$

$$\Delta°G_{MN} = °G_{MN} - °G_M - °G_N = RT\left[lna_M^{\gamma} + lna_N^{\gamma} - \ln(1-x)\right] \qquad (1-18)$$

From Eqs. (1 – 17) and (1 – 18) and the basic thermodynamic data, along with the ideal assumptions, one can write the solubility products of MC and MN of the carbonitride as:

$$logk_{MC} = log\frac{[M][C]}{x} = A_1 + \frac{B_1}{T} \qquad (1-19)$$

$$logk_{MN} = log\frac{[M][N]}{1-x} = A_2 + \frac{B_2}{T} \qquad (1-20)$$

which are consistent with the definition of the solubility product as in Eq. $(1-10)$. The solubility products of carbides and nitrides in microalloyed steels have been collected systematically by Gladman [2], and they can be used to evaluate the solubility of the precipitate phase with convenience.

Additionally, other alloying elements should not be ignored as the existence of elements such as Mn and Si might change the activities of M, C and N in solution. According to Wagner [33], an adequate representation of the equilibria encountered in steelmaking is possible only if the effects of the various solutes on the activity coefficient are taken into account. Using a Taylor series expansion for the excess partial molar free energy or the logarithm of the activity coefficient and disregarding the second and higher order derivatives, the activity coefficient becomes a linear function of the mole fractions of the various solutes:

$$\ln f_2(x_2, x_3, x_4, \ldots) = lnf_2^{\circ} + x_2\epsilon_2^{(2)} + x_3\epsilon_2^{(3)} + x_4\epsilon_2^{(4)} + \cdots \qquad (1-21)$$

where, the coefficients $\epsilon_2^{(2)}$, $\epsilon_2^{(3)}$, etc., are defined as:

$$\epsilon_2^{(2)} = \lim_{x_2\to 0}\frac{\partial lnf_2}{\partial x_2}, \qquad \epsilon_2^{(3)} = \lim_{x_3\to 0}\frac{\partial lnf_2}{\partial x_3}, \qquad etc. \qquad (1-22)$$

Based on the Wagner's formulation, the activities of the solutes should be modified with the Wagner interaction parameters in a system containing solutes M, C and N:

$$lna_M^{\gamma} = lnx_M^{\gamma} + \varepsilon_M^M x_M^{\gamma} + \varepsilon_C^M x_C^{\gamma} + \varepsilon_N^M x_N^{\gamma} \qquad (1-23)$$

$$lna_C^{\gamma} = lnx_C^{\gamma} + \varepsilon_C^M x_M^{\gamma} + \varepsilon_C^C x_C^{\gamma} + \varepsilon_N^C x_N^{\gamma} \qquad (1-24)$$

$$lna_N^{\gamma} = lnx_N^{\gamma} + \varepsilon_N^M x_M^{\gamma} + \varepsilon_C^N x_C^{\gamma} + \varepsilon_N^N x_N^{\gamma} \qquad (1-25)$$

and thus, the modified solubility products with the effects of solute interactions become:

$$logk_{MC} = log\frac{[M][C]}{x} - 0.4343\sum_i\sum_j \varepsilon_i^j x_j = A_1 + \frac{B_1}{T} - 0.4343\sum_i\sum_j \varepsilon_i^j x_j \quad (1-26)$$

$$logk_{MN} = log\frac{[M][N]}{1-x} - 0.4343\sum_i\sum_j \varepsilon_i^j x_j = A_2 + \frac{B_2}{T} - 0.4343\sum_i\sum_j \varepsilon_i^j x_j \quad (1-27)$$

where, $i = M, C\ or\ M, N; j = M, C, N$.

If other alloying elements such as Mn, Si, Al, V, Ti, Nb, Mo exist in the system, the Wagner interaction terms should also be taken into account. It has to be mentioned that the summation of all interaction terms can be positive (> 0), negative (< 0) or even zero (0), depending on the magnitude of each alloying component. The Wagner interaction parameter ε_i^j can be measured experimentally and some of them have been reported by Sharma [34] and were reproduced in Table 1-1[2].

Table 1-1: Wagner interaction parameters (Reproduced from Sharma [34])

Parameter	Value	Parameter	Value
$\boldsymbol{\varepsilon_C^C}$	$\frac{8890}{T}$	$\boldsymbol{\varepsilon_C^{Nb}}$	$-\frac{66257}{T}$
$\boldsymbol{\varepsilon_N^N}$	$\frac{6294}{T}$	$\boldsymbol{\varepsilon_N^{Nb}}$	$-\frac{66257}{T}$
$\boldsymbol{\varepsilon_C^{Cr}}$	$7.02-\frac{21880}{T}$	$\boldsymbol{\varepsilon_C^{Ni}}$	$0.69+\frac{4600}{T}$
$\boldsymbol{\varepsilon_C^{Mo}}$	$3.86-\frac{17870}{T}$	$\boldsymbol{\varepsilon_N^{Mn}}$	$-\frac{8336}{T}-27.8$
$\boldsymbol{\varepsilon_{Nb}^{Nb}}$	-2	$\boldsymbol{\varepsilon_C^{Mn}}$	$-\frac{5070}{T}$
$\boldsymbol{\varepsilon_C^N}$	$\frac{5790}{T}$	$\boldsymbol{\varepsilon_C^{Si}}$	$4.84+\frac{7370}{T}$
$\boldsymbol{\varepsilon_N^{Si}}$	$\frac{57700}{T}-35.0$	$\boldsymbol{\varepsilon_N^{Cr}}$	$-\frac{65150}{T}+24.1$
$\boldsymbol{\varepsilon_N^{Mo}}$	$\frac{2888}{T}-33.1$	$\boldsymbol{\varepsilon_{Nb}^{Mn}}$	$-\frac{305033}{T}+203.57$
$\boldsymbol{\varepsilon_{Nb}^{Cr}}$	$140.8-\frac{216135}{T}$	$\boldsymbol{\varepsilon_{Nb}^{Ni}}$	$21.24-\frac{40510}{T}$
$\boldsymbol{\varepsilon_{Nb}^{Si}}$	$\frac{77265}{T}-44.91$	$\boldsymbol{\varepsilon_{Nb}^{Mo}}$	0

---

[2] The Wagner interaction parameters between niobium and substitutional elements were determined from the NbC solubility data.

1.2.2.3.2 Kinetics

Different from thermodynamics which essentially determines the possibility of a physical process, kinetics is dealing with the reaction rate of such a process, from non-equilibrium states to equilibrium ones. Due to the large lattice misfit between the carbides/nitrides and the matrix, strain-induced precipitation was developed with the heterogeneous nucleation of the second phase, i.e. nucleation starts on dislocations and at dislocation nodes. The orientation relationship (OR) between them is typically called the *Cube-on-Cube*. Interphase-precipitated particles, however, exhibit different ORs with the matrix (e.g. the *Baker-Nutting*). These ORs will be summarized in the next section:

1.2.2.3.2.1 Orientation relationships

As having been widely investigated, the principal compound which precipitates in steels is the face-centred cubic (FCC) NaCl-type (B1) in the form of MC_xN_{1-x}. The precipitates may have different morphology or distribution as can be identified by transmission electron microscopy (TEM) easily. However, they exhibit similar orientation relationships with austenite and ferrite. For precipitation in austenite, the simple *Cube-on-Cube* lattice orientation relationship (OR) is observed [35]:

$$(100)_{MC_xN_{1-x}} // \ (100)_\gamma$$
$$(010)_{MC_xN_{1-x}} // \ (010)_\gamma$$

A detailed example is a dense dispersion of small secondary niobium carbonitride precipitates in a commercial TP347 Nb-stabilized austenitic steel as shown in Fig. 1-3. The precipitates are semi-coherent having the *Cube-on-Cube* OR with the austenitic matrix [36]. Three different zone axes were aligned to illustrate the OR with diffraction patterns. The carbonitride precipitate heterogeneously as a consequence of the large misfit between the precipitates and the matrix. This misfit ranges from ~15% in the case of VN to ~25% in the case of NbC [8]. The misfit can be largely accommodated when they form on dislocations. This is the reason why the precipitates prefer to nucleate on the dislocation network during hot deformation of microalloyed steels.

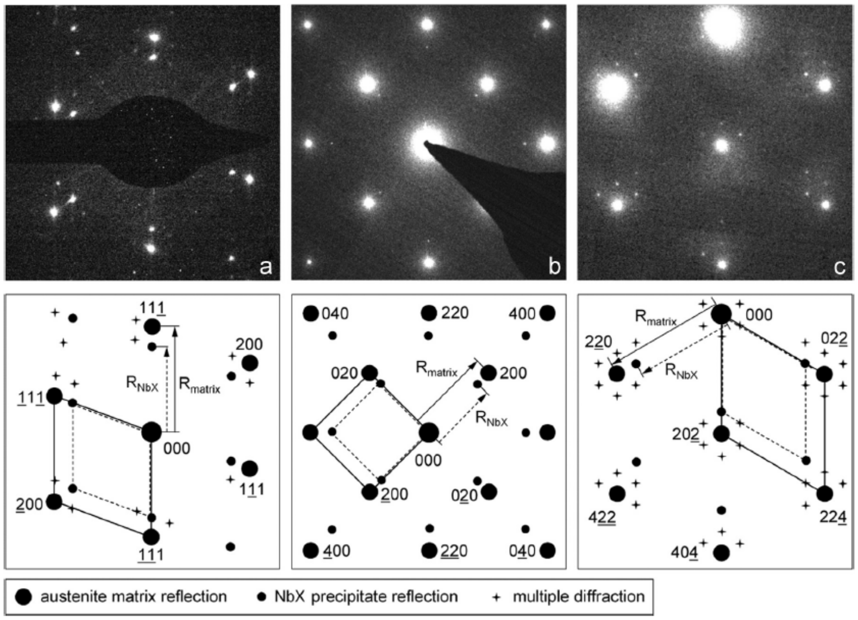

Fig. 1-3: SAD electron diffraction patterns recorded from 0.5μm wide areas containing only small precipitates, providing unambiguous evidence that the precipitate dispersion consists of FCC NbX formed in *cube-on-cube* orientation relationship with the austenite matrix. The beam directions are (a) z=<110>, (b) z=<100> and (c) z=<111> [36].

For precipitation in ferrite, two forms of MC_xN_{1-x} precipitates are known, i.e. precipitation in the supersaturated ferrite, and interphase precipitation which is also referred to 'precipitation-row' precipitation shown in Fig. 1-4 (a) and (b). One of the orientation relationship with ferrite is termed the *Baker-Nutting* [37], which is given as:

$$(100)_{MC_xN_{1-x}} // (100)_\alpha$$
$$[011]_{MC_xN_{1-x}} // [010]_\alpha$$

Through these two different ORs with the matrix, it should be possible to separate the precipitates into two groups: one forming at high temperature in the austenite and the other that forms during the cooling stage at which ferrite grows. It has to be mentioned, in order to study the OR in austenite, the austenitic model alloys should be used in order to preserve the microstructure by quenching to room temperature.

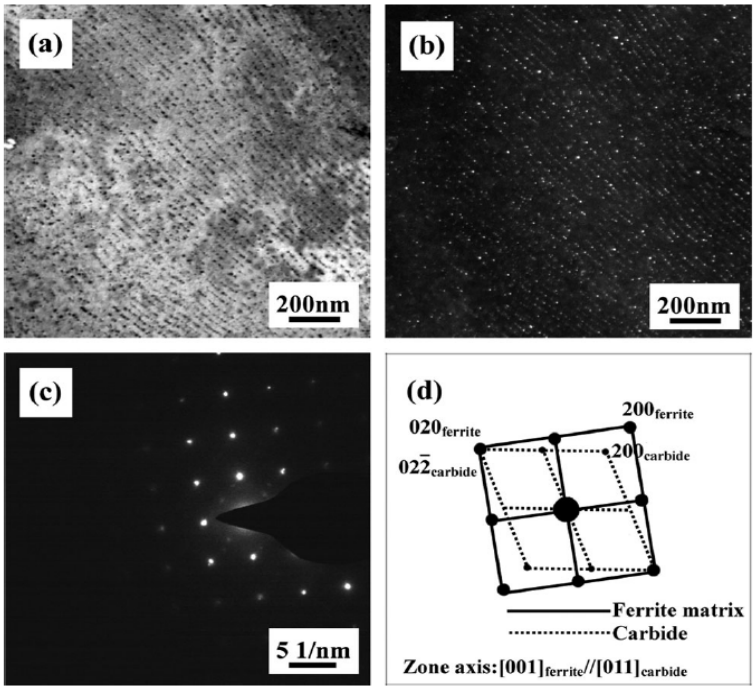

Fig. 1-4: (a) A bright-field transmission electron micrograph, (b) a dark-field transmission electron micrograph, (c) the corresponding selected area electron diffraction pattern of interphase-precipitated particles, and (d) the calibration of the selected area electron diffraction pattern, showing a *Baker–Nutting* orientation relationship between precipitated particles and ferrite matrix [37].

During deformation, dislocations are introduced mechanically into the matrix, in the form of dislocation tangles, cell structure or microbands. Dislocation nodes are created, due to the intersections of dislocations. The nodes provide preferred nucleation sites for precipitation when the deformation temperature is lower than the solubility temperature of carbides, nitrides or carbonitrides. The classical precipitation model proposed by Dutta and Sellars [38] is widely adopted for industrial applications. In their model, there are two major combined stages: (i) nucleation and growth and (ii) growth and coarsening. The nucleation rate depends on the chemical driving force and the dislocation density. The growth and coarsening processes are facilitated by the fast pipe diffusion due to the dislocation network, similar to that inside grain boundaries. These two stages will be summarized in the following sections:

1.2.2.3.2.2 Nucleation and growth

The nucleation rate is obtained from the classical theory of nucleation as:

$$\frac{dN}{dt}|_{nucleation} = (N_{tot} - N)Z\beta^* \exp\left(-\frac{\Delta G^*}{k_b T}\right) \exp\left(-\frac{\tau}{t}\right) \qquad (1-28)$$

$$N_{tot} = 0.5\rho^{1.5} \qquad (1-29)$$

$$\beta^* = \frac{4\pi(r^*)^2 CD}{a_0^4} \qquad (1-30)$$

where, N is the number of precipitates per unit volume, t is the time, N_{tot} is the total number of nucleation sites (i.e. dislocation nodes) per unit volume, Z is the Zeldovich factor which is approximately 1/20, β^* is the atomic impingement rate, ΔG^* is the activation energy of the critical nucleus, k_b is the Boltzmann constant, T is the temperature in Kelvin, τ is the incubation time for nucleation taken to be zero considering that heterogeneous nucleation is almost an instantaneous process requiring no incubation time, ρ is the dislocation density, r^* is the radius of the critical size for precipitation nucleation, a_0 is the lattice parameter of austenite, and C and D are the bulk concentration and diffusivity of the major microalloying element, respectively.

The critical energy barrier ΔG^* can be solved numerically from the free energy balance ΔG between the chemical free energy, the interfacial free energy and the dislocation core energy released. The formulation was organized by Zurob [8] and is given below as:

$$\Delta G = V\Delta G_V - \left(\frac{\mu b^2 r \ \ln\left(\frac{r}{b}\right)}{2\pi(1-\nu)} + \mu b^2 r/5\right) + A\gamma \qquad (1-31a)$$

where, V is the volume of the transformed nucleus, ΔG_V is the chemical free energy difference per unit volume of the transformation, μ is the shear modulus, b is the Burgers vector, r is the radius of precipitates, ν is the Poisson's ratio, A and γ are the surface area and surface energy of the nucleus, respectively. The chemical driving force for carbonitride can be calculated with respect to solubility products as:

$$\Delta G_V = -\frac{RT}{V_P} ln \frac{C_M [C_C]^x [C_N]^{1-x}}{[K_{MC}]^x [K_{MN}]^{1-x} x^x (1-x)^{1-x}} \qquad (1-31b)$$

where, R is the gas constant, x is the site fraction of carbon in the interstitial sublattice, V_P is the molar volume of the precipitate, C_i is the instantaneous concentration of element i in austenite, K_{MC} and K_{MN} are the solubility products for MC carbide and MN nitride. The detailed derivation of the equation is presented in Appendix II.

At the nucleation and growth stage, the instantaneous number density of nuclei can now be obtained from the integration of the nucleation rate dN/dt. The growth of the nuclei is controlled by the diffusion of microalloying element *M*. The growth rate is given as [8, 38]:

$$\frac{dr}{dt}|_{growth} = \frac{D_{eff}}{r} \frac{C_M - C_M^r}{C_M^P - C_M^{eq}} + \frac{1}{N} \frac{dN}{dt} (\alpha r^* - r) \qquad (1-32)$$

$$D_{eff} = D_{pipe} \pi R_{core}^2 \rho + D_{bulk}(1 - \pi R_{core}^2 \rho) \qquad (1-33)$$

where, D_{eff} is the effective diffusion coefficient. C_M^r, C_M^P and C_M^{eq} denote the composition of *M* in equilibrium with a precipitate particle of radius r, the composition of *M* of the precipitate and the composition of *M* in equilibrium with a planar precipitate, respectively. The first term in Eq. $(1-32)$ is the standard diffusion controlled growth law for a spherical particle [39] and the second term is the rate of change of the average particle radius resulting from the nucleation of dN new particles of size αr^* during time dt [8, 40], α is taken as 1.05 in the model. D_{eff} is an average of the pipe diffusion coefficient D_{pipe} and the bulk diffusion coefficient D_{bulk}, depending on the dislocation density ρ and the cross-section area of the dislocation core πR_{core}^2.

1.2.2.3.2.3 Growth and coarsening

Growth rate is shown in Eq. $(1-32)$ for the pure growth stage of the particles. In the coarsening stage, there will be a dispersed distribution of the particles and an average radius *r* of them. According to Gibbs-Thomson effects equation [41], the solubility limit of solutes in the matrix in equilibrium with the precipitate should be modified. The smaller radius particle owns higher solubility limit, which generates a concentration gradient between two non-identical particles. Solutes will diffuse from the small particle to the big one. Consequently, those precipitates whose radii are greater than the average will grow, while the smaller ones diminish and disappear.

Following Deschamps and Bréchet [40], the rate of change of particle size was given by Zurob [8] as:

$$\frac{dr}{dt}\Big|_{coarsen.} = \frac{D_{eff}}{r}\,\frac{C_M^r - C_M^{27r/23}}{C_M^P - C_M^{Eq}} \qquad (1-34)$$

$$\frac{dN}{dt}\Big|_{coarsen.} = \frac{dr}{dt}\Big|_{coarsen.} \cdot \left[\frac{r^* C_M}{r(C_M^P - C_M)}\left(\frac{3}{4\pi r^3} - 2N + \frac{4\pi r^3 N^2}{3}\right) - 3\mathrm{N}\right] \qquad (1-35)$$

where, $C_M^{27r/23}$ is the solute *M* concentration of the matrix in equilibrium with a precipitate of radius *27r/23*. The transition criterion from nucleation and growth stage to growth and coarsening stage is that the diminution of the precipitate density by coarsening is larger than the increase of the precipitates density by nucleation [40], i.e.

$$-\frac{dN}{dt}\Big|_{growth+coarsening} > \frac{dN}{dt}\Big|_{nucleation}. \qquad (1-36)$$

Under conditions of simultaneous growth and coarsening, the average rate of changes of particle size and number density of nuclei are given below as:

$$\frac{dr}{dt} = (1 - f_{coarse})\frac{dr}{dt}\Big|_{growth} + f_{coarse}\frac{dr}{dt}\Big|_{coarsening} \qquad (1-37)$$

$$\frac{dN}{dt} = f_{coarse}\frac{dN}{dt}\Big|_{coarsening} \qquad \left(\frac{dN}{dt}\Big|_{growth} = 0\right) \qquad (1-38)$$

$$f_{coarse} = 1 - \mathrm{erf}\left(4\left(\frac{r}{r^*} - 1\right)\right) \qquad (1-39)$$

1.2.2.3.3 Multi-pass precipitation

The abovementioned precipitation model has been applied successfully to single-pass deformations [38]. However, multi-pass scenarios are always encountered in industry. Thus, multi-pass precipitation should be considered since subsequent passes may generate new dislocation configurations. Secondly, experimental results such as [42] indicate that the precipitates nucleate within microbands having two dense dislocation walls (DDWs). It is different from the 3-D dislocation nodes assumption in the model by Dutta and Sellars [38]. Thirdly, the Dutta and Sellars model considers a global average concentration of niobium. The diffusion of niobium is the rate controlling process for the precipitation growth. With the new microbands treatment, the global concentration of niobium should be modified, and the local concentration should be considered.

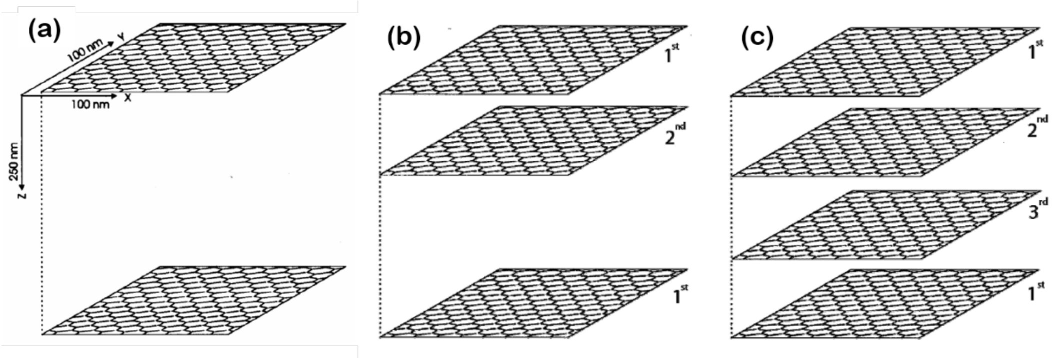

Fig. 1-5: Microbands configurations during multi-pass deformations: (a) the first pass; (b) the second pass and (c) the third pass [43].

For the multi-pass case, Sellars and Palmiere [43] proposed microbands configuration during as shown in Fig. 1-5 schematically. For the first pass, one set of parallel microbands is generated. Within the microbands, dislocation networks/nodes form and thus provide potential nucleation sites for precipitation. The matrix is therefore divided into separate blocks. Solutes diffuse from the separated matrix to the microbands walls and the bulk diffusion of niobium is the rate controlling process for such a process. For the second or third pass deformation, new sets of microbands will be created and the newly formed microbands cut the matrix into smaller blocks (Fig. 1-5(b) and (c)). Thus, it is possible to consider the multi-pass precipitation processes by tracking the local solute concentration with respect to the corresponding microbands.

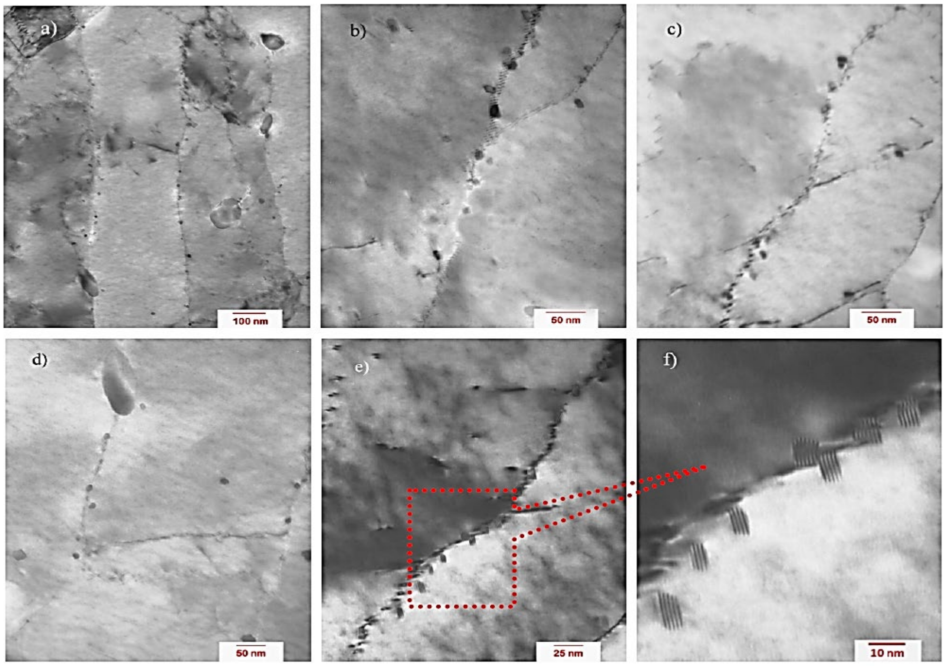

Fig. 1-6: TEM micrographs of thin foils taken from a sample subjected to a two pass PSC test of strains 0.75 and 0.25 with a hold time of 25 seconds after each pass at 850°C. Figures show fine precipitates lying on microband walls along with some large precipitates not all on microbands [42].

Nagarajan et al [42, 44] worked on the multi-pass precipitation simulations continuously. The solutionized sample was strained to 0.75 and held for 25 secs, and then strained to another 0.25 for the second deformation at 850°C and 900°C. The samples were subjected to transmission electron microscopy observation and analysis of precipitates. One of the typical TEM results is shown in Fig. 1-6, in which fine precipitates are lying on the microbands walls along with few outside. As mentioned, it was difficult to distinguish the nature of precipitation, whether it was formed after the first deformation pass or the second. Another experiment where the sample was strained to 0.75 and held for 25 secs, and then strained to another 0.50 and quenched immediately was designed and conducted. The results show that all the microbands carried precipitates which suggests that the second deformation did not produce new microbands. However, it is questionable that no new microbands were produced in the second pass deformation. Secondly, a Fe-30%Ni model alloy was used in their work and the model alloy may play a role on the dislocation structure characteristics during hot deformation. A different dislocation configuration may alter the situation for precipitation in subsequent deformation passes. Therefore, more research work can be conducted to investigate the multi-pass precipitation behavior.

1.2.2.3.4 Model alloy selection

The austenite microstructure during hot deformation is unknown, due to the unavoidable phase transformation upon cooling which inhibits the direct observation of the microstructure. It is known that strain-induced precipitation is largely depending on the dislocation configuration after deformation. A good knowledge of the deformed austenite microstructure at high temperatures helps the understanding of the precipitation behavior in steels. Over the years, various types of model alloys have been used such as austenitic stainless steel [45], Ni-Co alloys [46] and Ni-Fe alloys [43, 47]. Unfortunately, austenitic stainless steel has a low stacking fault energy at low temperatures which limits its applicability as a model alloy over a wider temperature range. A Ni-30%Co alloy has a stacking fault energy of ~72 mJ/m^2 which is very close to that of austenite [48]. Recently, Ni-Fe alloys draw more attention than the others. Sellars and Palmiere [43] used an Fe-30%Ni alloy to study the multi-pass precipitation behavior as mentioned above. However, according to Charnock and Nutting [48], the thermionic electron emission microscopy was utilized to measure the number of annealing twins in Fe-Ni alloy system at 1000°C and related this to the stacking fault energy at that temperature. Based on this work, an Ni-30%Fe alloy would have the same stacking fault energy (SFE, ~60-70 mJ/m^2) as low alloy steel at hot-rolling temperatures. The variation of stacking fault energy across the Fe-Ni system is presented in Fig. 1-7.

Moreover, according to Hurley [47], the hot-deformation flow curves of the model Ni-30%Fe alloy were similar to those of the low carbon steel with respect to the shape of the curve and critical features such as peak strain. The flow curve comparison between the

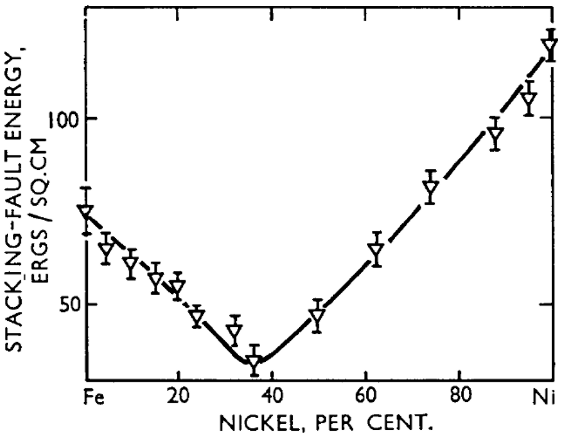

Fig. 1-7: The variation of stacking fault energy across the Fe-Ni system [48].

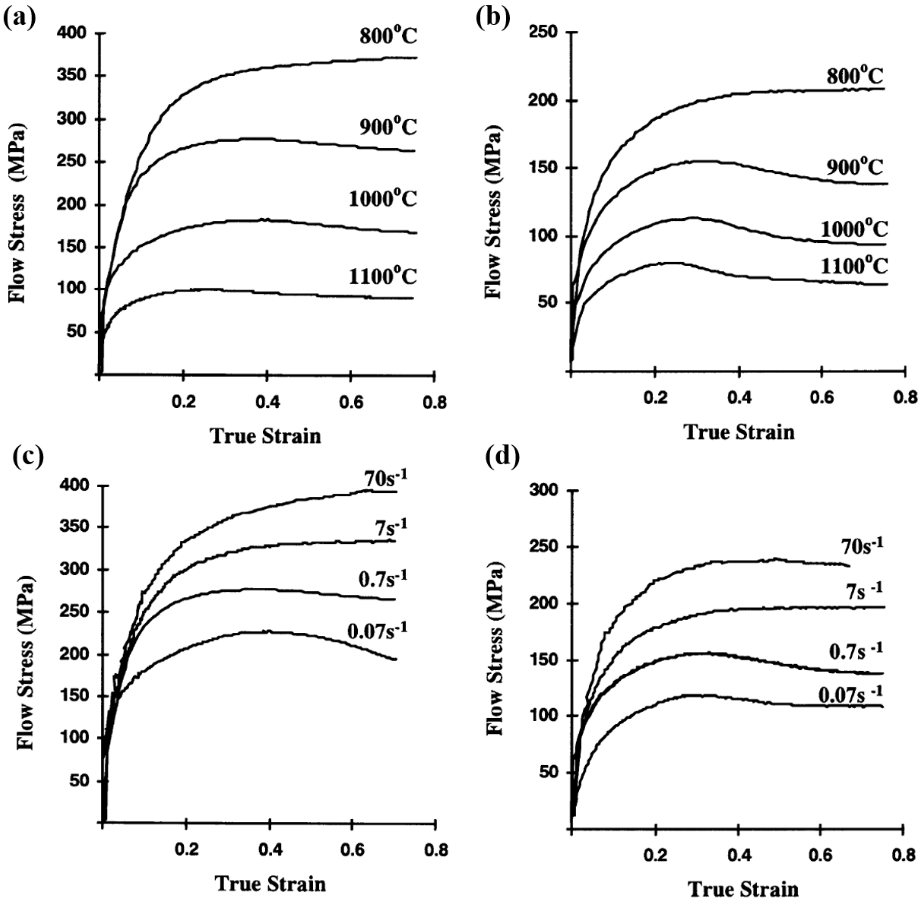

Fig. 1-8: Flow stress curves at a strain rate of 0.7 s^{-1} for (a) Ni-30%Fe and (b) a 0.15%C steel at varying temperatures; and flow stress curves at 900°C for (c) Ni-30%Fe and (d) a 0.15%C steel with varying strain rates [47].

model Ni-30%Fe alloy and a low carbon (0.15%C) steel is shown in Fig. 1-8. As pointed out by Hurley, dynamic recrystallization occurred for both alloys at similar strains above 800°C. Peak strains for the Ni-30%Fe model alloy and the low carbon steel are 0.38 ± 0.03 and 0.33 ± 0.03, respectively, at 900°C at a strain rate of 0.7 s^{-1}. The shape of the curves is analogical recognizing that the flow stress of the model alloy is higher which is due to the solid solution strengthening. The dislocation density might also be close since the yielding stress of the model alloy seems to be higher than that of the low carbon steel. It is, thus, plausible to assume these two alloys will behave similarly during hot deformation.

Considering both the stacking fault energy and hot-deformation behavior analogies, the Ni-30%Fe model alloy is believed to be a suitable candidate for studying the austenite microstructure and also good for the investigation of precipitation behavior. Discussions on the potential interactions between precipitation and microstructure (mainly the dislocation configuration) of the Ni-30%Fe model alloy are valuable to the hot deformation of austenite. Other alloy systems (e.g. Ni-Co alloys) may also be adopted as model alloys, given that the stacking fault energy and flow stress curve behaviors are similar at high temperatures.

1.2.2.4 Recovery

Annealing is one of the most crucial topics in metal production. Recovery is the very first annealing phenomenon when deformed products are heat treated at an elevated temperature or it happens concurrently with work hardening during hot deformation. It might be followed by recrystallization and grain growth, according to parameters such as alloy chemistry, temperature, strain, strain rate. As reviewed in Section 1.2.2.1 on constitutive relations, the stress increases quickly with the strain, which indicates a dramatic accumulation of dislocations. Slip is the dominant deformation mechanism for metals and alloys with relatively high SFE. Dislocations from different slip systems will be generated and accumulated under certain stress conditions. The interactions between dislocations can be very intensive, depending on the strain level.

Therefore, the dislocation network evolution (or growth) becomes the core of recovery. Dislocation recovery is actually a series of events which are shown in Fig. 1-9 schematically by Humphreys and Hatherly [49]. During recovery, the tangled dislocations start to realign themselves into cell structures, followed by the annihilation of dislocations within cells, the formation of subgrains and subgrain growth, by all of which the total Gibbs free energy of the deformed state is lowered spontaneously. There are two primary processes: the annihilation of dislocations and the rearrangement of dislocations. Both two processes are achieved by the motions of dislocation glide, climb and cross-slip. During recovery, some of the properties such as material density and electrical resistivity will be restored to the pre-deformed conditions.

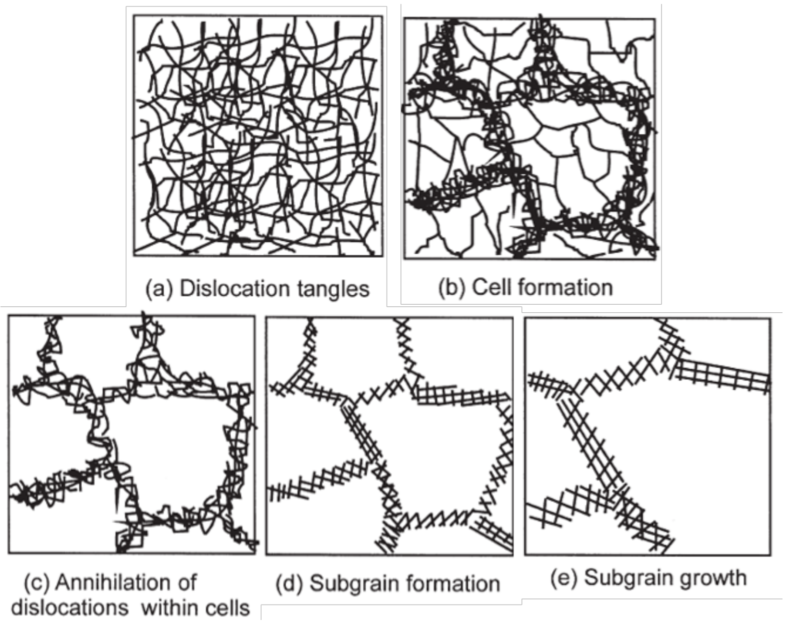

Fig. 1-9: Cell structure evolution during the recovery process of a plastically deformed material [49].

Nes [50] revisited the topic of recovery and summarized the major contributions from early decades (1950s ~1970s) by many researchers. The dislocation network growth mechanism was largely and essentially discussed, in terms of four possible controlling mechanisms: thermally activated glide, thermally activated cross-slip, climb and solute drag. According to Verdier [51], one assumes relaxation rate of the internal stress occurs by thermally-activated mechanisms as:

$$\frac{d\sigma_i}{dt} = -K exp\left(\frac{-U(\sigma_i)}{k_b T}\right) \qquad (1-40)$$

$$U(\sigma_i) = U_0 - V\sigma_i \qquad (1-41)$$

where, K is a constant, $U(\sigma_i)$ is the activation energy which decreases linearly with the stress, V is the activation volume of the elementary recovery events. Integration of Eq. $(1-40)$ leads to a logarithmic time decay of the yield stress:

$$\sigma_i = \sigma_0 - \frac{kT}{V}\ln\left(1 + \frac{t}{t_0}\right) \qquad (1-42)$$

$$t_0 = \frac{kT}{KV}\exp\left(\frac{U_0 - V\sigma_0}{k_b T}\right) \qquad (1-43)$$

where, t_0 is called a reference time, and σ_0 is the initial stress at the beginning of the decay (t = 0). The logarithmic decay is the most notable characteristic for the recovery process. It will be used to identify the transition from recovery to recrystallization during stress relaxation analysis. The detailed derivation of Eqs. $(1-42)$ and $(1-43)$ can be located in Appendix III. For the stress relaxation test, the total strain is held to be a constant, i.e. $\varepsilon_{\mathrm{tot}} = \varepsilon_{\mathrm{e}} + \varepsilon_{\mathrm{p}} = C$. The differentiation with respect to time gives rise to:

$$\frac{d\sigma_i}{dt} = -\dot{\varepsilon_{\mathrm{p}}} E \qquad (1-44)$$

It has to be mentioned here again that σ_i is the internal stress due to dislocations. The lattice friction stress part has been discarded since it will be a constant at fixed temperatures. As we all know, the flow stress, σ, is related to the dislocation density, ρ, through the forest-type relation which is:

$$\sigma = \sigma_y + M_T \alpha_T \mu b \sqrt{\rho} \qquad (1-45)$$

where, σ_y is the yielding stress, M_T is the Taylor factor, α_T is a constant of the order of 0.15. b is the Burgers vector. The Orowan law which bridges the plastic strain changing rate with the average dislocation migration velocity $\bar{v}$ is given as:

$$M_T\dot{\varepsilon_{\mathrm{p}}} = \rho b\bar{v} \qquad (1-46)$$

$$\bar{v} = b\upsilon_D \exp\left(\frac{-U_0}{k_b T}\right)\sinh\left(\frac{\sigma_i V}{k_b T}\right) \qquad (1-47)$$

where, υ_D is the Debye frequency of the material. Combining Eqs. $(1-44)$ to $(1-47)$, the rate of change of the internal stress due to the dislocation network evolution is given as:

$$\frac{d\sigma_i}{dt} = -\frac{64}{9{M_T}^3{\alpha_T}^2}\frac{\sigma_i^2}{E}\upsilon_D \exp\left(\frac{-U_0}{k_b T}\right)\sinh\left(\frac{\sigma_i V}{k_b T}\right) \qquad (1-48)$$

1.2.2.4.1 Effect of precipitation

According to Zurob [8], precipitation and recovery interact for mainly two reasons: the precipitates are nucleated heterogeneously on dislocations and the precipitate particles are able to pin the dislocation growth. Needless to say, fast recovery would anneal out more dislocations and thus could render less nucleation sites for precipitation (i.e. instantaneous dislocation density is used to calculate the number of nucleation sites) in the nucleation stage as expressed from Eqs. $(1-28)$ to $(1-30)$.

As illustrated in 1.2.2.3 precipitation module, the precipitation kinetics can be predicted quantitatively, either the particle number density or the total volume fraction. Thus, the effect of precipitation on the recovery kinetics can also be quantified theoretically. Zurob [8] discussed the effect in terms of the net driving force for the recovery of a 3-D dislocation network. The ratio of the net driving force to the total driving force, $\mathfrak{I}$, can be thought of as the unpinned fraction of the dislocation network:

$$\mathfrak{I} = \frac{G_R^{net}}{G_{tot}} \approx 1 - \frac{N}{N_c} \qquad (1-49)$$

where, N is the number density of particles, N_c is the instantaneous number of maximum nucleation sites available. As a result, the rate of change of the internal stress due to the dislocation network evolution should be modified, taking the precipitation pinning effect into consideration, as:

$$\frac{d\sigma_i}{dt} = -\frac{64}{9{M_T}^3{\alpha_T}^2}\frac{\sigma_i^2}{E}v_D exp\left(\frac{-U_0}{k_b T}\right) sinh\left(\frac{\sigma_i V}{k_b T}\right)\left(1-\frac{N}{N_c}\right) \quad (N < N_c) \quad (1-50)$$

$$\frac{d\sigma_i}{dt} = 0 \quad (N \geq N_c) \quad (1-51)$$

A good example of the effect of precipitation on recovery is from Liu and Jonas [52]. During the stress relaxation test, a pre-strain of 0.05 was introduced in order to avoid the occurrence of recrystallization. The stress evolution was then recorded precisely. As can be observed from Fig. 1-10, the stress curve decayed slowly due to the dislocation network growth. The slope of the curve changed at some point (see arrows in Fig. 1-10), and this is due to the onset of the precipitation of titanium carbonitrides under certain deformation conditions.

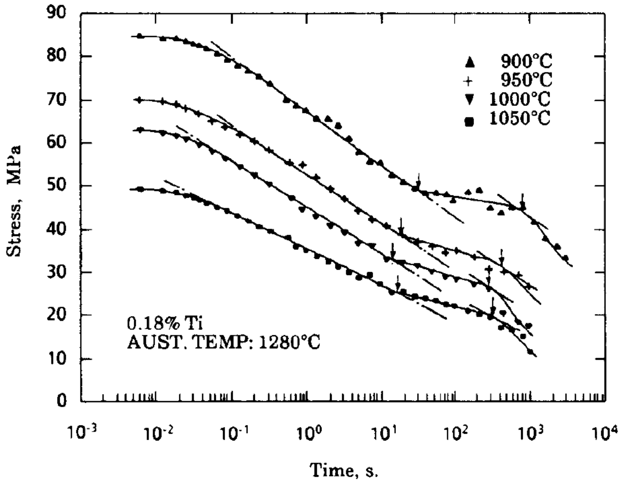

Fig. 1-10: Stress relaxation curve for a 0.18% Ti steel tested at 900~1050°C. The arrows indicate the relaxation times at which specimens were quenched [52].

1.2.2.4.2 Effect of solutes

The simple treatment of the effect of microalloying is through the interaction volume term. The interaction volume term was defined as ba^*l, where l is the obstacle spacing (also called activation length) and a^* is the activation distance. Generally, l is related to the number of jogs as a result of the dislocation intersection. Therefore, the activation length l is a function of dislocation density [50]:

$$l = K/\sqrt{\rho} \qquad (1-52)$$

where, K is constant and close to unity in materials with high stacking fault energy. Besides the dislocation jogs, another pinning centre comes from impurity atoms/clusters with a spacing proportional to $1/\sqrt[3]{C}$. For simplicity, both pinning centres are treated as equivalent and net spacing pinning centres is estimated as

$$\frac{1}{l} = K_1\sqrt{\rho} + K_2\sqrt[3]{C} \qquad (1-53)$$

where, K_1 and K_2 are proportionality constants [53]. In the existence of multiple microalloying elements, the constant K should be estimated for each one. And the net spacing centres is in a more general form as:

$$\frac{1}{l} = K_1\sqrt{\rho} + \sum_i K_i\sqrt[3]{C_i} \qquad (1-54)$$

The higher microalloying concentration is, the smaller activation length will be and then smaller activation volume. The rate of change of the internal stress will be reduced in terms of the activation volume term.

1.2.2.5 Recrystallization

Recrystallization is the formation of a new set of strain-free and equiaxed grains that have low dislocation density and are characteristic of the precold-worked condition. During recrystallization, the mechanical properties that were changed as a result of cold working are restored to their precold-worked values [54]. The driving forces for both recovery and recrystallization are the increased stored energy from deformation, i.e. the present of dislocations. However, the migration of high angle grain boundary, which removes dislocations completely, is an essential characteristic for recrystallization.

It is of tremendous importance to study the kinetics of recrystallization during metal and alloy productions, since the microstructure is determined by the specific heat treatment and thus the eventual mechanical properties of materials. The kinetics of primary recrystallization is usually described by the Johnson-Mehl-Avrami-Kolmogorov (JMAK) model. Under assumptions of constant nucleation rate, $\dot{N}$, and constant growth rate, $\dot{G}$, and with the extended volume concept, the recrystallization volume fraction X is expressed as:

$$X = 1 - \exp\left(\frac{-\pi \dot{N} \dot{G}^3 t^4}{3}\right) \tag{1-55}$$

The detailed derivation of X can be found in the literatures [49, 55] and it is also re-derived in Appendix IV. And a more generally written form of X_V is shown below as:

$$X = 1 - \exp(-Bt^n) \tag{1-56}$$

where, B and n are referred as Avrami constants.

Static recrystallization has been studied extensively worldwide in the field of physical metallurgy [11, 15, 22, 56]. The general form of the equation for the recrystallization kinetics is a modified JMAK equation in Eq. $(1-57)$, in which $t_{0.5}$ is the time for 50% static recrystallization proposed by Sellars [56, 57]. Knowledge of the dependence of n and $t_{0.5}$ on the thermomechanical and metallurgical parameters permits the complete description of the recrystallization kinetics [22]:

$$\mathrm{X} = 1 - \exp\left\{-0.639\left(\frac{t}{t_{0.5}}\right)^n\right\} \tag{1-57}$$

$$t_{0.5} = B\varepsilon^s d_0^p Z^q \exp\left(\frac{Q_{rex}}{RT}\right) \tag{1-58}$$

where, B, p, q and s are parameters that depend on the chemical composition of the steel, ε is the strain, d_0 is the austenite grain size in μm, Z is the Zener-Hollomon parameter and Q_{rex} is the activation energy for recrystallization. For microalloyed steels, there is a need to combine the solute drag effect of the added elements and the onset of strain-induced precipitation. A modified model for 50% static recrystallization time was applied to a range of Cu-Ni-Nb steels [17]:

$$t_{0.5} = (-5.24 + 550[Nb]) \times 10^{-18} \varepsilon^{-4+77[Nb]} d_0^2 \exp\left(\frac{330{,}000}{RT}\right) \tag{1-59}$$

However, these empirical or semi-empirical models were still not sufficiently accurate and convenient for applications and there were issues associated with full implementation of the models [17].

Humphreys [19, 20] analyzed the growth and stability of cellular microstructures, taking account of the orientation dependence of boundary energies and mobilities, and developed a simple unified theory of continuous and discontinuous recovery, recrystallization and grain growth. An important type of recrystallization is strain induced grain boundary migration (SIBM), in which part of a pre-existing grain boundary bulges into the adjacent substructure, leaving a dislocation-free recrystallized region behind the migrating boundary as shown schematically in Fig. 1-11. Based on SIBM, Zurob et al [3, 4, 8] coupled models for precipitation, recovery and recrystallization in order to describe the microstructural evolution behavior of industry alloys. The well-developed recrystallization model will be illustrated hereby in this section.

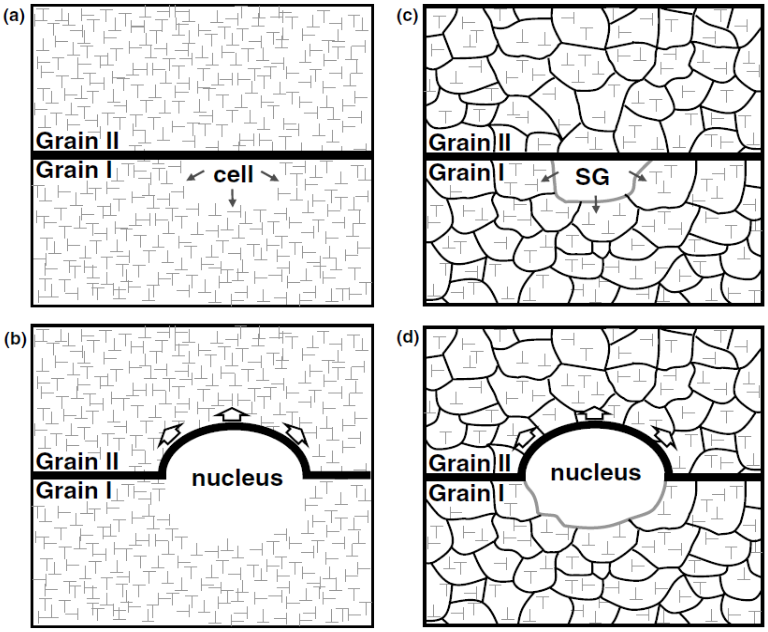

Fig. 1-11: Possible examples of recrystallization nucleation sites. In (a) and (c), the cell/subgrain initially grows within Grain I. When the cell/subgrain reaches the critical size which allows it to overcome the capillary force, it bulges into Grain II and a nucleus is formed by SIBM as shown in (b) and (d) [7].

1.2.2.5.1 Recrystallization nucleation

From the early work done by Bailey and Hirsch [58], the driving force due to the stored energy of dislocations and boundary curvature ($2\gamma/R$, where γ is the boundary energy and R is the radius of the subgrain) are two opposing factors for strain induced grain boundary migration. The evolution of driving force, $G(t)$, of remaining dislocations can be depicted and calculated in the recovery module. By making the two opposing forces equal, one can simply find that the critical subgrain size of a recrystallization nucleus which is:

$$r_c(t) = \frac{2\gamma}{G(t)} \tag{1-60}$$

where, $r_c(t)$ is the minimal size for a subgrain to become a viable recrystallization nucleus and it increases when the stored energy is dissipating from the materials.

The actual subgrain may or may not exceed the critical subgrain size at some point, depending on the deformation parameters such as strain and temperature. For example, if the strain is lower than the critical value, the subgrain can by no means reach the critical subgrain size, which is the case that recrystallization is suppressed. The stress dependence of the subgrain size is often found to vary according to the relation by Raj and Pharr [59]:

$$d_s = Kb\left(\frac{G}{\sigma}\right)^m \tag{1-61}$$

where, d_s is the subgrain diameter, b is the Burgers vector, σ is the applied stress, G is the shear modulus and K and m are constants. The cell structure evolution and subgrain growth have been reviewed by many scientists such as Humphreys [49]. Normally, the subgrain size obeys a Rayleigh distribution, and it is feasible to monitor the evolution of the average subgrain size, $\overline{r(t)}$:

$$\overline{r(t)} = \overline{r_0} + \int_0^t MG(t)dt \tag{1-62}$$

where, the $MG(t)$ term is the instantaneous rate of subgrain growth. The critical value of the normalized subgrain size, χ, can be defined as:

$$\chi_c = \frac{2\gamma}{G(t)(\overline{r_0} + \int_0^t MG(t)dt)} \qquad (1-63)$$

when $\chi > \chi_c$, the subgrains are able to become the viable recrystallization nuclei and number of the nuclei per unit volume can be accumulated. With the growth of the average subgrain size, the relative smaller subgrains χ can surpass the criterion of being a nucleus, as shown in Fig. 1-12.

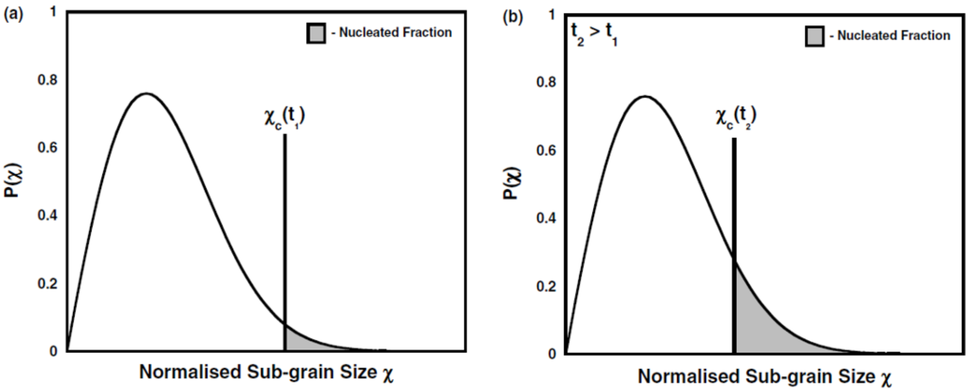

Fig. 1-12: Fraction of subgrains which gives rise to viable recrystallization nuclei consists of subgrains whose size is greater than χ_c. As the value of χ_c decreases with increasing annealing time (due to subgrain growth), more subgrains are able to nucleate [7].

1.2.2.5.2 Recrystallization grain growth

The grain boundary of a nucleus is a high angle grain boundary and is driven by the dissipation of the stored energy retained in the unrecrystallized region. From Zurob [8], the classic JMAK model can still be applied and recrystallization fraction, *X*, is given by:

$$X = 1 - \exp\left(-N_{rex}\left(\int_0^t M(t)G(t)dt\right)^3\right) \qquad (1-64)$$

where, the instantaneous grain boundary mobility considering the solute drag effect and instantaneous net driving force subtracted by Zener pinning force are utilized.

1.2.2.6 Grain growth

Grain growth[3] is the annealing phenomenon following recrystallization. Technically, it can be divided into two types: normal grain growth and abnormal grain growth (or secondary recrystallization). Within the current scope of multi-pass rolling modelling, only normal grain growth is considered in the context, i.e. grain growth means the normal grain growth behavior. Different from recovery and recrystallization, the driving force for grain growth is the reduction of the total grain boundary areas that own relatively high energy compared to the matrix.

According to the surface tension theory by Burke [60], Burke and Turnbull [61] deduced the kinetics of grain growth on the assumption that the driving pressure, P, on a boundary arises only from the curvature of the boundary:

$$P = \gamma_b \left(\frac{1}{R_1} + \frac{1}{R_2} \right) \qquad (1-65)$$

where, γ_b is the grain boundary energy, R_1 and R_2 are the principal radii of curvature of a boundary. If the boundary is part of a sphere of radius, R, and the radius of curvature, R, is proportional to the mean radius, $\bar{R}$, of an individual grain. The more generally modified driving pressure, with a small geometric constant α', is expressed as:

$$P = \frac{\alpha' \gamma_b}{\bar{R}} \qquad (1-66)$$

The boundary velocity is proportional to the driving pressure P, i.e.

$$\frac{d\bar{R}}{dt} = c_1 \frac{\alpha' \gamma_b}{\bar{R}} \qquad (1-67)$$

and therefore, we can derive the parabolic growth law as:

$$\bar{R}^2 - \bar{R}_0^2 = ct \qquad (1-68)$$

where, R_0 is the grain radius before the grain growth and c is a constant.

---

[3] Strictly speaking, grain growth means that each grain in the microstructure will increase its size. The fact is that only relatively large grains grow by the consumption of the small ones. Grain coarsening is a more precise terminology to describe the process. However, grain growth is still used as a convention.

The grain growth equation will usually be written, with n being the grain growth exponent, in the more general form:

$$\bar{R}^n - \bar{R}_0^n = ct \qquad (1-69)$$

As listed in Table 1-2, the grain growth exponents for some of the high purity metals were measured by researchers [62-65]. The evidence in favour of $n = 2$ being the prediction of theory for an ideal single phase material in which the boundary velocity is proportional to driving pressure and boundary energies are isotropic, appears to be conclusive [49]. However, the measured exponents are rarely found to be 2 and are usually larger than 2. This is due to the consequence of the non-ideality of the materials, i.e. slightly away from the assumptions used during the development of the model. There are several important parameters that will affect the growth kinetics such as the presence or development of texture, non-equiaxed initial grain structure, twinning and so on.

Table 1-2: Grain growth exponents for isothermal grain growth in high purity metals (Reproduced from Anderson [66])

Metal	Exponent *n*	Reference
Al	4	Gordon and El Bassyoumi [63]
Fe	2.5	Hu [65]
Pb	2.5	Bolling and Winegard [64]
Pb	2.4	Drolet and Gallibois [62]
Sn	2.3	Drolet and Gallibois [62]

The majority of statistical grain growth theories fall into the category of mean field theories within which the average of the growth behavior is utilized to represent the whole assembly. Two commonly known models are the drift model by Hillert [67] and the diffusion model by Louat [68]. During grain growth, the larger grains will grow, and small grains will shrink (and finally disappear, see 2-D case in Fig. 1-13). As a result, the grain size of the whole assembly increases with time. In order to quantify the kinetics, Hillert

[67] developed a statistical theory of grain growth based on the Ostwald ripening treatment by Lifshitz and Slyozov [69].

From Hillert's statement, an expression of the correct dimension and with the characteristic feature that it is positive for large R but negative for small R is needed. The critical size where the value of the expression goes through zero will be denoted by R_{cr}. The simplest choice for the driving force seems to be:

$$P = \gamma_b \left(\frac{1}{R_1} + \frac{1}{R_2}\right) = \alpha' \gamma_b \left(\frac{1}{R_{cr}} - \frac{1}{R}\right) \qquad (1-70)$$

and then the velocity of the migrating grain boundary is:

$$\frac{dR}{dt} = \alpha' M \gamma_b \left(\frac{1}{R_{cr}} - \frac{1}{R}\right) \qquad (1-71)$$

where, M is the high angle grain boundary mobility.

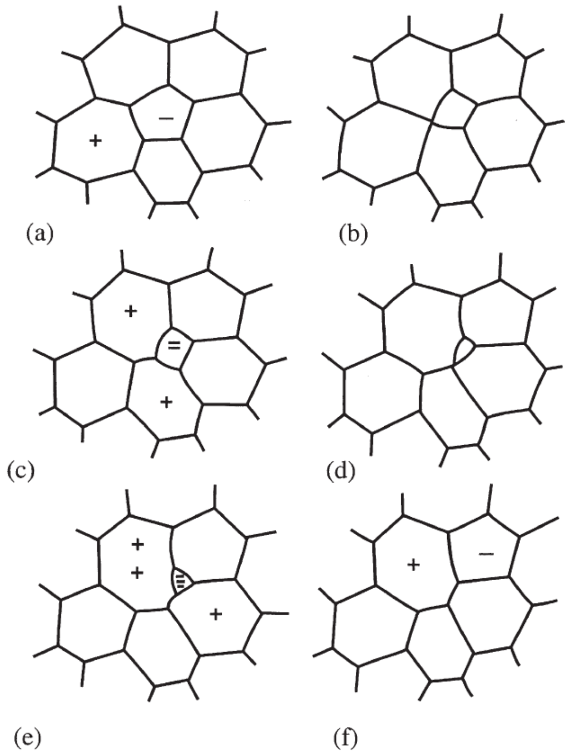

Fig. 1-13: Schematic diagram of growth of a 2-dimensional grain structure. (a) A grain of less than or more than 6 sides introduces instability into the structure, (b)–(f) Shrinking and disappearance of the 5-sided grain [67].

With mathematical transformation and deliberate derivation, Hillert gave the growth rate equation for normal grain growth:

$$\frac{dR_{cr}^2}{dt} = \frac{1}{2}\alpha' M\gamma_b \qquad (1-72)$$

which is quite close to the value obtained by Feltham [70]. By his further analysis, it was found that, in three-dimensional situation, $\alpha' = 1$ and $R_{cr} = \frac{9}{8}\bar{R}$ and then

$$\bar{D}^2 - \bar{D}_0^2 = 1.58 \cdot M\gamma_b t \qquad (1-73)$$

where, $\bar{D}$ is the average diameter of the grains and $\bar{D}_0$ is the original average grain size. The differential format of the grain growth equation can be written (in diameter) as:

$$\frac{dD}{dt} = M \cdot \frac{\omega}{2}\frac{\gamma_b}{D} \qquad (1-74)$$

or (in radius) as:

$$\frac{dR}{dt} = M \cdot \frac{\omega}{8}\frac{\gamma_b}{R} \qquad (1-75)$$

where, ω is a constant of 1.58.

1.2.3 Experimental methods for hot deformation

It is not difficult to develop a mathematical model for a physical metallurgical process, and there are various kinds of models at different scales and levels. For the multi-pass rolling, there are the semi-empirical modelling originating from Sellars [56, 57], the cellular automaton modelling such as Zheng et al [71], the physically-based modelling by Zurob [8], etc. However, all these models need to be validated against experimental results. The experimental methods that can be used to investigate thermomechanical processing of microalloyed steels are demonstrated in the following sections:

1.2.3.1 Double-hit deformation

The double-hit test means that the material undergoes two successive deformations in a cycle. As can be seen in Fig. 1-14, the specimen is reheated to 1250℃ for 3 mins and then cooled down to the deformation temperature between 800℃ and 1100℃. The first pass deformation is given at certain strain rate and the deformation temperature specified. Then the specimen awaits a period of time which is called interpass time. During the interpass time interval, the annealing phenomena of recovery, recrystallization and grain growth as well as precipitation occur, if all possible, and the softening of the material initiates. After the isothermal holding, the specimen is reloaded with the same conditions, i.e. the second pass deformation. The stress strain curve of the second pass would be identical to the first one if complete softening is attained; while the curve would continue following the first if no softening happens. Any intermediate scenario would fall into somewhere in-between.

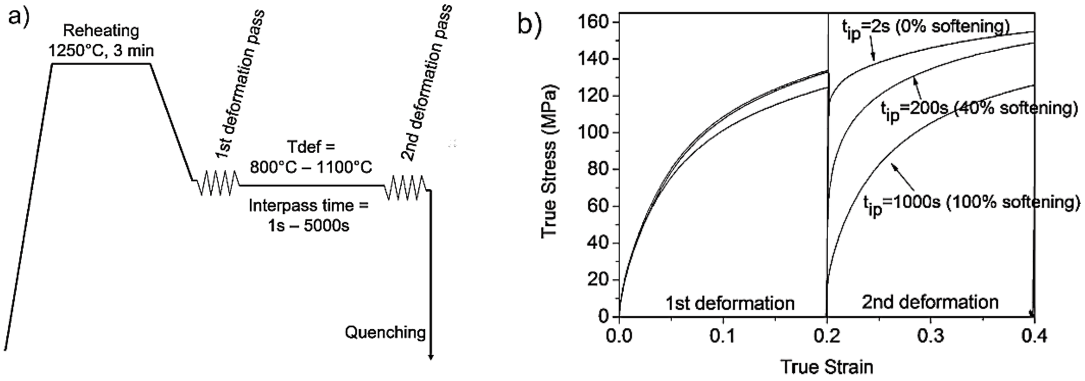

Fig. 1-14: Principle of the double deformation test (a) and resulting stress-strain curves from the double deformation test used to calculate the fraction of softening during the interpass time (b) [72].

The recrystallization kinetics can be quantified by the degree of softening through the double-hit deformation test. The degree of softening can be represented by the softening fraction which is defined as:

$$S = \frac{\sigma_w - \sigma_p}{\sigma_w - \sigma_r} \qquad (1-76)$$

where, σ_w, σ_p and σ_r refer to the flow stress of work-hardened, partially-restored and completely-restored materials, respectively. However, the calculation of softening fraction S from the double-hit stress strain curves is worth thinking meticulously. Many evaluation methods (0.2% offset, 20% softening, 2% offset, 5% total strain, back extrapolation and mean stress) were proposed for this purpose [22, 73-76]. The major methods were reviewed by Fernandez et al [73] as shown in Fig. 1-15. Overall, 2% offset, 5% total strain, and mean stress methods are the most suitable ones, if precipitation does not occur to affect recovery and recrystallization kinetics.

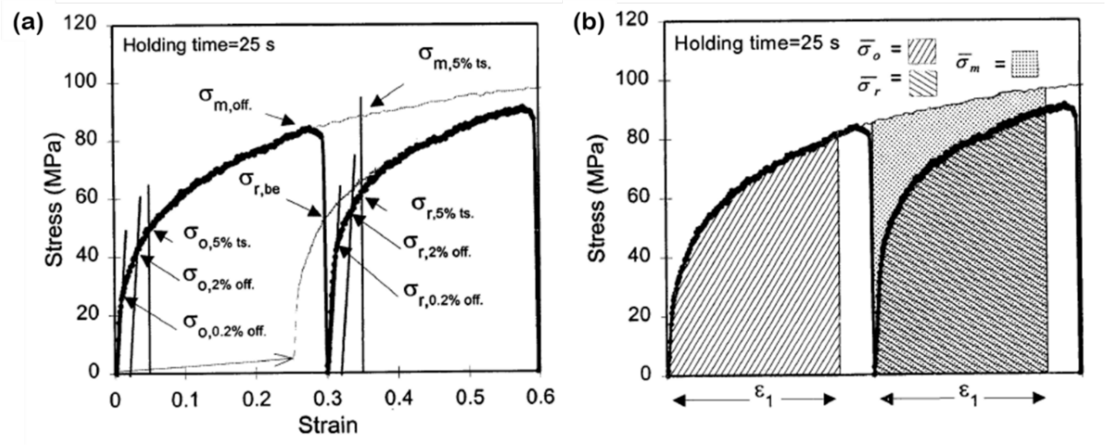

Fig. 1-15: Determination of the stresses used to calculate the softening fraction by (a) the 0.2% offset, 2% offset, back extrapolation and the 5% total strain methods and (b) the mean flow stress method [73].

1.2.3.2 Stress relaxation

The recrystallization kinetics can be monitored by the degree of softening through a double-hit deformation test. However, the double-hit deformation has two major disadvantages. At first, the contributions of recovery and recrystallization cannot explicitly be separated. Secondly, the double-hit deformation procedures are tedious because for each point a new sample is needed, and a complete program of thermomechanical treatment has to be performed. The method of stress relaxation, however, allows measuring the total course of the softening behavior with only one sample. Furthermore, stress relaxation enables the determination of both recovery and recrystallization kinetics of austenite after deformation [72].

The sample is reheated to 1250°C for 3 mins for homogenization and cooled down to the deformation temperature that is usually between 800°C and 1100°C. A certain deformation strain is applied and then the sample is held at constant total strain (elastic and plastic). The stress decay is monitored and recorded with high precision with a holding time from few secs to two thousand secs, followed by quenching. The complete deformation cycle can be conducted with either Gleeble or dilatometer. A schematic cycle is shown in Fig. 1-16 (a). In the next step, the stress versus logarithmic time is plotted as it has been proved that the stress is approximately linear to logarithmic time for recovery processes. The dramatic deviation from the linearity of the curve is due to the occurrence of recrystallization (Fig. 1-16 (b)).

Therefore, the stress relaxation method can be used to study the effect of alloying elements on recovery. The slope of the curve would be different as the interaction volume might be changing with the alloy chemistry. Also, one can investigate the recrystallization kinetics of a certain conditions, like the time for complete recrystallization, softening fraction, etc.

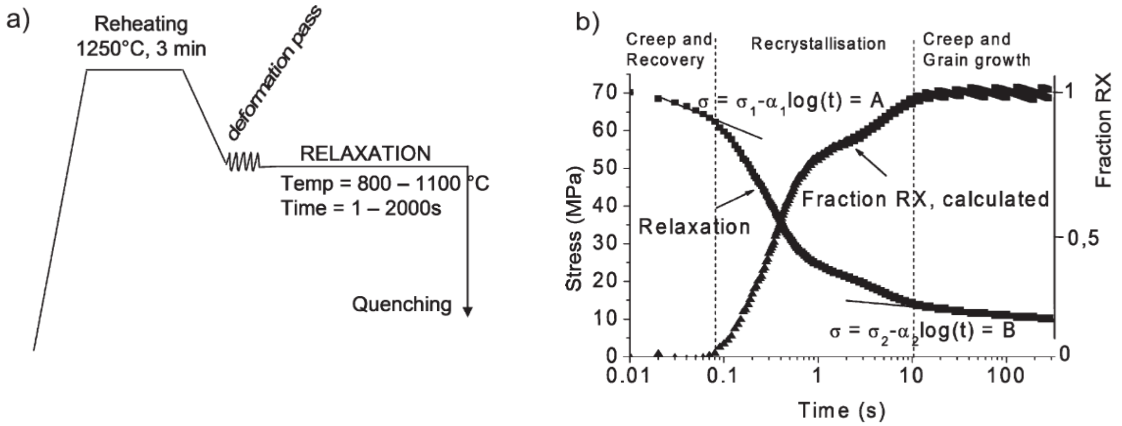

Fig. 1-16: (a) Illustration of the principle of a stress relaxation test and (b) illustration of the analysis of a stress relaxation test following the Karjalainen approach [72].

1.2.3.3 Laser-ultrasonics

It is always tedious, and even challenging, to measure the grain size in an isothermal or non-isothermal process. With conventional metallography methods, it is impossible to conduct the in-situ measurement of the grain growth. However, the novel in-situ laser-ultrasonics technique makes it feasible. Laser-ultrasonics is a remote, continuous and non-destructive technique that can be operated in-situ at high temperatures for bulk observations [77]. It is based on the generation of ultrasonic waves by a pulsed laser and the subsequent detection of these waves by a laser interferometer. The specimen geometry and the laser-ultrasonics experimental setup are shown in Fig. 1-17(a) [77].

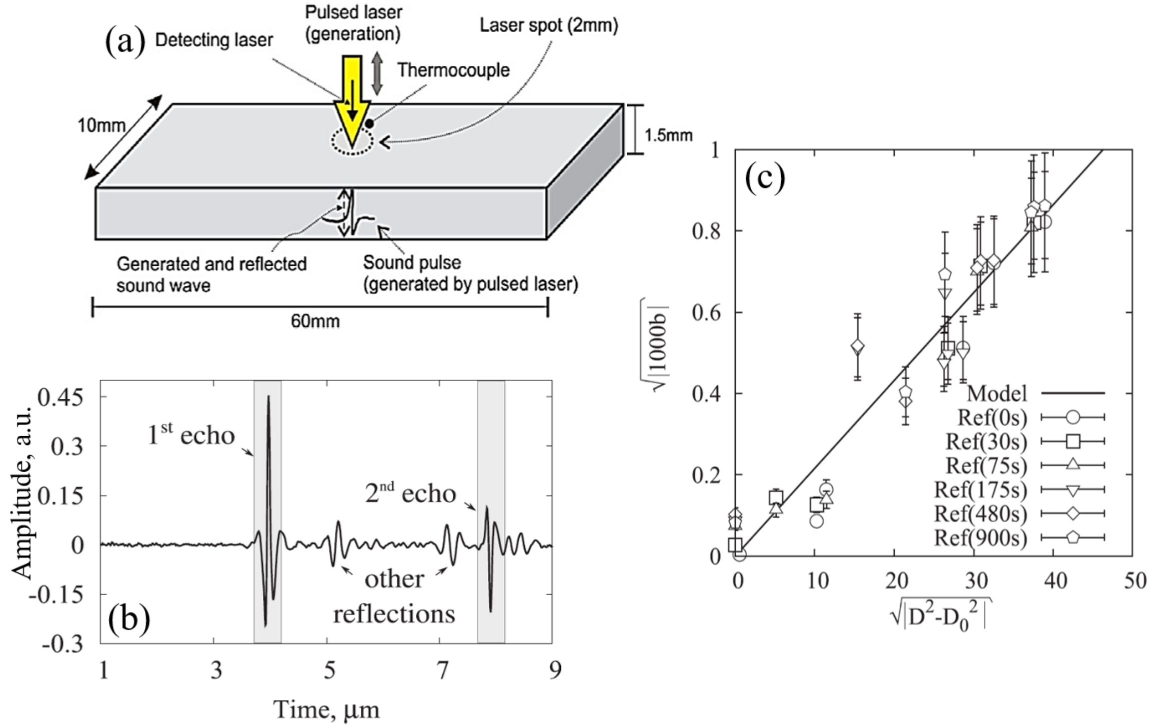

Fig. 1-17: (a) Schematic diagram of the specimen geometry and the laser-ultrasonics experimental setup [77]; (b) An ultrasound waveform measured at a specific time and (c) Correlation between the fitting parameter and grain size [78].

Analysis of the detected ultrasonic pulse provides microstructural information. The ultrasound velocity is, for instance, a direct measure of the elastic modulus, which depends on temperature, crystal structure and texture. The decay of an ultrasonic wave depends on scattering by the microstructure (i.e. by the bulk of the grains) and internal friction. An ultrasound waveform measured at a specific time shows the wave amplitude decay (1st echo to 2nd echo) in Fig. 1-17(b) [78]. The attenuation, $\alpha(f)$, can be fitted as a function of frequency as $a + bf^n$, where a and b are fitting parameters, n is a constant depending on the material. The attenuation of the waves determines the value of parameter b which can be correlated with the grain size (in Fig. 1-17(c)). More details about the fitting process can be found in the literature [78-81].

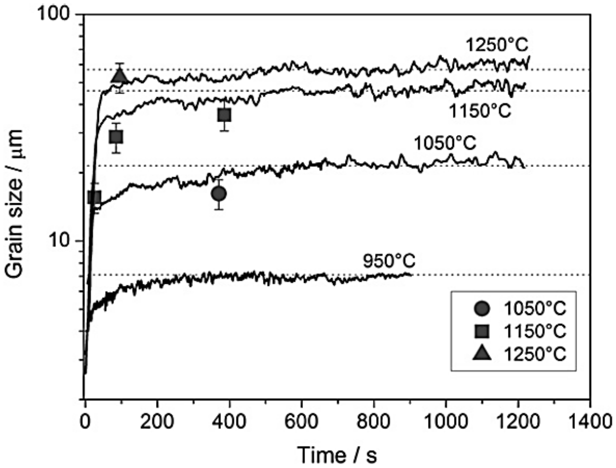

Fig. 1-18: Austenite grain growth behaviour measured by laser-ultrasonics at 10°C / s heating rate followed by isothermal holding. Time zero corresponds to 900°C, and the symbols are average volumetric grain diameters measured by metallography. Dashed lines show the limiting grain sizes [77].

The measured austenite grain size evolutions at four different temperatures are shown in Fig. 1-18. The grain size increases fast at short times and run into a plateau for a long period of isothermal holding. The traditional metallographic measurements were also included for comparison. As can be seen, there is a good quantitative agreement between laser-ultrasonics and the metallographic measurements. Another similar example from Legrand et al [82] is shown in Fig. 1-19. Generally, the grain size dropped and then increased after reaching a minimum value. After the completion of recrystallization, grain growth was triggered. Two different strains were implemented in the study. Apparently, grain size of the low strain condition is larger than that of the higher one. Dynamic recrystallization should have occurred for the 0.75 strain case. Thus, laser-ultrasonics is an effective and effort-saving (also timesaving) way to measure the in-situ grain size evolution.

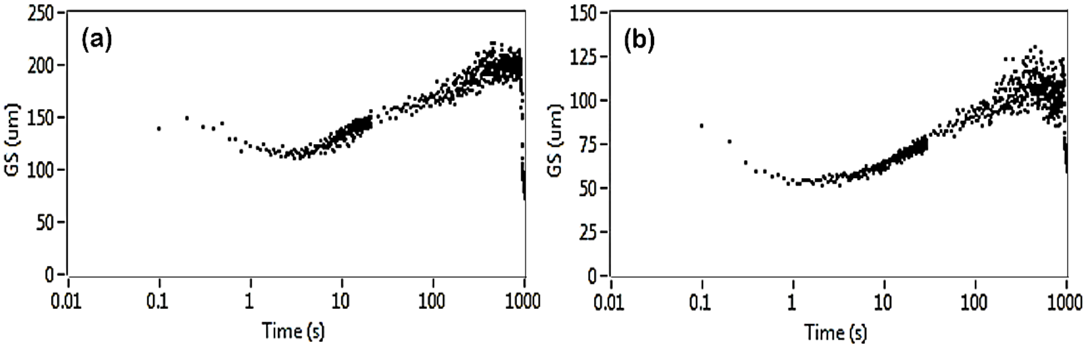

Fig. 1-19: Measured grain size evolution for a C-Mn steel: (a) T=1050°C, ε=0.25 and (b) T=1050°C, ε= 0.75. The strain rate is 1 s^{-1} for both conditions [82].

1.2.3.4 Transmission electron microscopy

Conventional Transmission Electron Microscopy (CTEM) is utilized to analyze materials based on either mass-thickness contrast or diffraction contrast. Crystal defects such as dislocations or orientation relationships (ORs) between matrix and precipitate can be studied and elucidated explicitly with CTEM. For metallurgists, the orientation relationship study is important somehow. Two good examples can be found in Figs. 1-3 and 1-4 in Section 1.2.2.3.2.1. Moreover, the number density and size distribution of precipitates can also be estimated. High angle annular dark field (HAADF) in scanning TEM mode (STEM) is a robust way, providing good contrast between precipitates and their surroundings, to obtain detailed precipitation information, from both carbon replica and metal foil specimens. Nowadays, with the advancements of the characterization techniques such as electron energy loss spectroscopy (EELS), the precipitation can be analyzed more systematically, from a few nanometers to microns. One example is from Ma et al [83], the titanium nitride and niobium carbide can be identified by high resolution TEM-EELS with images shown in Fig. 1-20. It confirmed the epitaxial growth nature of NbC precipitation on pre-existing TiN particles in the steel X90. Scientists are developing continuously on the EELS methods such as parallel electron energy loss spectrum (PEELS) which allows better quantification of carbon-nitrogen ratio of the carbonitrides [84] or dual electron energy loss spectroscopy (DualEELS) which guarantees more accurate signal extraction

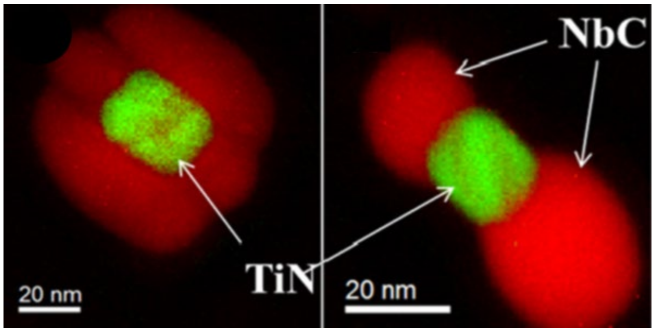

Fig. 1-20: High resolution TEM-EELS image of TiN-NbC composite precipitates observed in X90, showing epitaxial growth of NbC on pre-existing TiN particles [83].

from the raw data [85]. One example of PEELS study is shown in Fig. 1-21, which investigated the composition of the proeutectoid ferrite precipitates as a function of precipitate size, along with EDX analysis. The results confirmed that the smallest precipitates, which are assumed to have nucleated at low temperatures, are vanadium rich. The nitrogen content decreases, and the carbon content increases with decreasing precipitate size. Therefore, a systematic analysis of precipitates including particle size distribution, precipitation classification, morphology, accurate composition, etc. is feasible and beneficial with the advancement of TEM equipment.

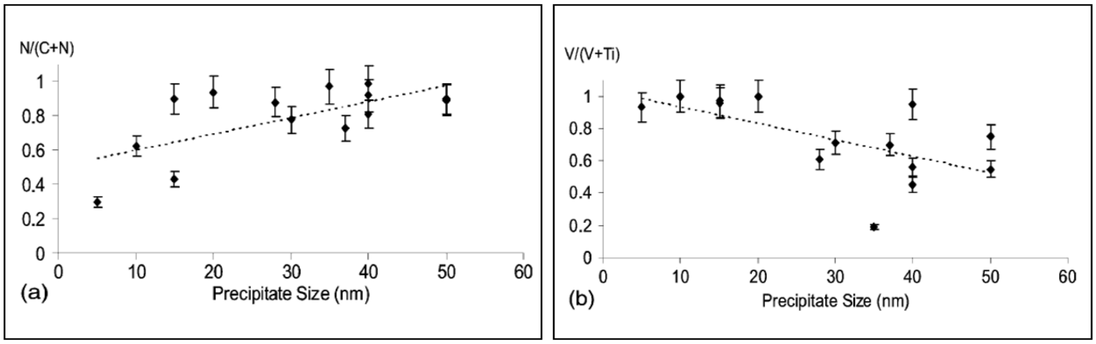

Fig. 1-21: (a) PEELS measurements of precipitate nitrogen to carbon atomic ratios in proeutectoid ferrite of a ferrito-pearlitic microalloyed vanadium steel Fe-0.38C-0.107V-0.010Ti-0.026Al-0.015N. The steel had previously been austenitised at 1250°C for 1 min, deformed above 1000°C and air cooled to 20°C at 1000°C / h, and (b) the corresponding vanadium to titanium atomic ratios as measured by EDX [84].

1.3 Scope and objective

The essence of thermomechanical controlled processing is the mutual interactions between deformation, recovery, recrystallization, grain growth and precipitation. Recovery reduces the driving force for grain boundary migration and potential nucleation sites for strain-induced precipitation. Precipitates in the matrix, on the contrary, will slow down the recovery process and exert pinning forces for grain boundary migration during recrystallization and grain growth. Therefore, the objective of the current work is to investigate the nature of each component and the potential interactions between them. The following topics will be covered during the course of study:

A) Alloying element effect on recovery and recrystallization.

- The effect of alloying elements of Mn, Si, Al and Nb on recovery and recrystallization will be studied by conducting stress relaxation tests on binary Fe-0.1%C and ternary Fe-0.1%C-X alloys.
- The effect of temperature on recovery kinetics will also be investigated.
- The alloying elements and temperature effects will be considered by fitting the recovery model through the activation volume term.

B) Precipitation behavior during multi-pass deformation.

- NbC precipitation behavior will be studied using a nickel-based model alloy. The sample will be deformed at room temperature and followed by annealed at 700°C. The deformation and annealing process will be repeated three times in order to elucidate the nucleation, growth and coarsening (if possible) of precipitates.
- Similar experiments on precipitation behavior will be carried out with two-pass hot-deformation and annealing process, and similar precipitation behavior investigation will be touched.
- The microstructures will be preserved by quenching and examined by transmission electron microscopy (with both metal foil and carbon replica specimens).

- Results from mechanical response and microstructural evolution will be linked and discussed. Meanwhile, a classical precipitation model will be adopted to simulate the kinetics of strain-induced precipitation.

C) Laser ultrasonic in-situ measurement of grain size evolution.

- The in-situ laser-ultrasonics measurement for grain size of C-Mn steels will be investigated at 950℃ and 1050℃, with different strains of 0.15, 0.25 and 0.35. Therefore, the effect of temperature and strain on recrystallization and grain growth (also on recovery from Topic A) will be covered and elucidated.
- The microalloying element of Nb on softening kinetics will also be investigated by comparing C-Mn/C-Mn-Nb steels at the same conditions. The solute drag effect of Nb will be discussed.
- The grain size evolution results may provide the possibility to develop robust thermomechanical processing models combining deformation, recovery, recrystallization and grain growth.

1.4 Reference

[1] J.R. Davis, Alloying: Understanding the Basics. , ASM International (2001) p. 193.

[2] T. Gladman, The physical metallurgy of microalloyed steels, The Institute of Materials, London, 1997.

[3] H.S. Zurob, Y. Bréchet, G. Purdy, A model for the competition of precipitation and recrystallization in deformed austenite, Acta Mater 49(20) (2001) 4183-4190.

[4] H.S. Zurob, C.R. Hutchinson, Y. Bréchet, G. Purdy, Modeling recrystallization of microalloyed austenite: effect of coupling recovery, precipitation and recrystallization, Acta Mater 50(12) (2002) 3075-3092.

[5] H.S. Zurob, C.R. Hutchinson, G.R. Purdy, Y. Bréchet, Investigation of the interaction between recovery and precipitation in a model austenitic alloy: Experimental and modelling results, Austenite Formation and Decomposition (2003) 121-138.

[6] H.S. Zurob, C.R. Hutchinson, Y. Bréchet, G.R. Purdy, Rationalization of the softening and recrystallization behaviour of microalloyed austenite using mechanism maps, Mat Sci Eng a-Struct 382(1-2) (2004) 64-81.

[7] H.S. Zurob, Y. Bréchet, J. Dunlop, Quantitative criterion for recrystallization nucleation in single-phase alloys: Prediction of critical strains and incubation times, Acta Mater 54(15) (2006) 3983-3990.

[8] H.S. Zurob, Effects of precipitation, recovery and recrystallization on the microstructural evolution of the microalloyed austenite, McMaster University, 2003.

[9] S. Vervynckt, K. Verbeken, B. Lopez, J.J. Jonas, Modern HSLA steels and role of non-recrystallisation temperature, International Materials Reviews 57(4) (2012) 187-207.

[10] M.K. Rehman, Modeling the microstructure evolution during hot deformation of microalloyed steels, McMaster University, 2014.

[11] G. Glover, C.M. Sellars, Static recrystallization after hot deformation of α iron, Metallurgical Transactions 3(8) (1972) 2271-2280.

[12] R.A.P. Djaic, J.J. Jonas, Recrystallization of high carbon steel between intervals of high temperature deformation, Metallurgical Transactions 4(2) (1973) 621-624.

[13] J.W. Bowden, F.H. Samuel, J.J. Jonas, Effect of interpass time on austenite grain refinement by means of dynamic recrystallization of austenite, Metallurgical Transactions A 22(12) (1991) 2947-2957.

[14] D.Q. Bai, S. Yue, W.P. Sun, J.J. Jonas, Effect of deformation parameters on the no-recrystallization temperature in Nb-bearing steels, Metallurgical Transactions a-Physical Metallurgy and Materials Science 24(10) (1993) 2151-2159.

[15] C.M. Sellars, J.A. Whiteman, Recrystallization and grain growth in hot rolling, Metal Science 13(3-4) (1979).

[16] P.D. Hodgson, R.K. Gibbs, A mathematical-model to predict the mechanical-properties of hot rolled C-Mn and microalloyed steels, Isij Int 32(12) (1992) 1329-1338.

[17] P.D. Hodgson, Microstructure modelling for property prediction and control, Journal of Materials Processing Technology 60(1-4) (1996) 27-33.

[18] G.M. Zhu, C. Lv, Y.L. Kang, G.G. Cheng, Three Dimensional Prediction of Microstructure Evolution and Mechanical Properties of Hot Strips, Materials Processing Technology, Pts 1-4 291-294 (2011) 455.

[19] F.J. Humphreys, A unified theory of recovery, recrystallization and grain growth, based on the stability and growth of cellular microstructures .1. The basic model, Acta Mater 45(10) (1997) 4231-4240.

[20] F.J. Humphreys, A unified theory of recovery, recrystallization and grain growth, based on the stability and growth of cellular microstructures .2. The effect of second-phase particles, Acta Mater 45(12) (1997) 5031-5039.

[21] O. Kwon, A Technology for the Prediction and Control of Microstructural Changes and Mechanical Properties in Steel, Isij Int 32(3) (1992) 350-358.

[22] A. Laasraoui, J.J. Jonas, Recrystallization of austenite after deformation at high temperatures and strain rates—Analysis and modeling, Metallurgical Transactions a-Physical Metallurgy and Materials Science 22(1) (1991) 151-160.

[23] A. Yoshie, T. Fujita, M. Fujioka, K. Okamoto, H. Morikawa, Formulation of flow stress of Nb added steels by considering work-hardening and dynamic recovery, Isij Int 36(4) (1996) 467-473.

[24] S.F. Medina, C.A. Hernandez, General expression of the Zener-Hollomon parameter as a function of the chemical composition of low alloy and microalloyed steels, Acta Mater 44(1) (1996) 137-148.

[25] S.F. Medina, C.A. Hernandez, The influence of chemical composition on peak strain of deformed austenite in low alloy and microalloyed steels, Acta Mater 44(1) (1996) 149-154.

[26] C.A. Hernandez, S.F. Medina, J. Ruiz, Modelling austenite flow curves in low alloy and microalloyed steels, Acta Mater 44(1) (1996) 155-163.

[27] K. Lücke, K. Detert, A quantitative theory of grain-boundary motion and recrystallization in metals in the presence of impurities, Acta Metallurgica 5(11) (1957) 628-637.

[28] J.W. Cahn, The impurity-drag effect in grain boundary motion, Acta Metallurgica 10(9) (1962) 789-798.

[29] M. Hillert, B. Sundman, A treatment of the solute drag on moving grain boundaries and phase interfaces in binary alloys, Acta Metallurgica 24(8) (1976) 731-743.

[30] M. Mukherjee, U. Prahl, W. Bleck, Modelling the strain-induced precipitation kinetics of vanadium carbonitride during hot working of precipitation-hardened Ferritic–Pearlitic steels, Acta Mater 71 (2014) 234-254.

[31] M. Hillert, S.L. I., The regular solution model for stoichiometric phases and ionic melts, Acta Chemica Scandinavica 24 (1970) 8.

[32] Thermo-Calc software package, http://www.thermocalc.com/, 2019.

[33] C. Wagner, Thermodynamics of Alloys, Addison-Wesley, London, 1952.

[34] R.C. Sharma, V.K. Lakshmanan, J.S. Kirkaldy, Solubility of niobium carbide and niobium carbonitride in alloyed austenite and ferrite, Metallurgical Transactions A 15(3) (1984) 545-553.

[35] A.T. Davenport, L.C. Brossard, R.E. Miner, Precipitation in microalloyed high-strength low-alloy steels, Jom-Us 27(6) (1975) 21-27.

[36] C. Solenthaler, M. Ramesh, P.J. Uggowitzer, R. Spolenak, Precipitation strengthening of Nb-stabilized TP347 austenitic steel by a dispersion of secondary Nb(C,N) formed upon a short-term hardening heat treatment, Materials Science and Engineering: A 647 (2015) 294-302.

[37] J. Chen, G.D. Wang, Precipitation Characteristics in a Low-Carbon Vanadium-Titanium-Bearing Steel, Steel Res Int 86(7) (2015) 821-824.

[38] B. Dutta, E.J. Palmiere, C.M. Sellars, Modelling the kinetics of strain induced precipitation in Nb microalloyed steels, Acta Mater 49(5) (2001) 785-794.

[39] G.J. Jones, R.K. Trivedi, Lateral Growth in Solid-Solid Phase Transformations, Journal of Applied Physics 42(11) (1971) 4299-4304.

[40] A. Deschamps, Y. Bréchet, Influence of predeformation and agEing of an Al–Zn–Mg alloy—II. Modeling of precipitation kinetics and yield stress, Acta Mater 47(1) (1998) 293-305.

[41] M. Perez, Gibbs-Thomson effects in phase transformations, Scripta Mater 52(8) (2005) 709-712.

[42] V. Nagarajan, A new approach for modelling strain induced precipitation of niobium carbonitrides in austenite during multipass hot rolling, University of Sheffield, 2011.

[43] C.M. Sellars, E.J. Palmiere, Modelling Strain Induced Precipitation of Niobium Carbonitride during Multipass Deformation of Austenite, Materials Science Forum 500-501 (2005) 3-14.

[44] V. Nagarajan, E.J. Palmiere, C.M. Sellars, New approach for modelling strain induced precipitation of Nb(C,N) in HSLA steels during multipass hot deformation in austenite, Mater Sci Tech 25(9) (2009) 1168-1174.

[45] E.L. Brown, A.J. DeArdo, Sheffield, 1980.

[46] R.K. Ray, P. Chapellier, J.J. Jonas, Correlations between the rolling textures in FCC Ni-Co alloys and the BCC transformation textures in controlled rolled steels, Textures and Microstructures 12(1-3) (1990) 141-153.

[47] P.J. Hurley, P.D. Hodgson, B.C. Muddle, A study of deformation substructures in austenite using a model Ni-30 wt.% Fe alloy, Scripta Mater 45(1) (2001) 25-32.

[48] W. Charnock, J. Nutting, The Effect of Carbon and Nickel upon the Stacking-Fault Energy of Iron, Metal Science Journal 1(1) (1967) 123-127.

[49] F.J. Humphreys, M. Hatherly, Recrystallization and Related Annealing Phenomena, Pergamon, Oxford, 1996.

[50] E. Nes, Recovery revisited, Acta Metallurgica Et Materialia 43(6) (1995) 2189-2207.

[51] M. Verdier, Y. Bréchet, P. Guyot, Recovery of AlMg alloys: Flow stress and strain-hardening properties, Acta Mater 47(1) (1998) 127-134.

[52] W.J. Liu, J.J. Jonas, A stress-relaxation method for following carbonitride precipitation in austenite at hot-working temperatures, Metallurgical Transactions a-Physical Metallurgy and Materials Science 19(6) (1988) 1403-1413.

[53] M.K. Rehman, H.S. Zurob, A Novel Approach to Model Static Recrystallization of Austenite During Hot Rolling of Nb Microalloyed Steel. Part I: Precipitate-Free Case, Metall Mater Trans A 44a(4) (2013) 1862-1871.

[54] W.D. Callister, D.G. Rethwisch, Materials science and engineering : an introduction, 2014.

[55] S. Liang, Deformation and its effect on recrystallization in magnesium alloy AZ31, McMaster University, 2012.

[56] C.M. Sellars, Physical metallurgy of hot working, 1980.

[57] C.M. Sellars, Modeling microstructural development during hot-rolling, Mater Sci Tech 6(11) (1990) 1072-1081.

[58] J.E. Bailey, P.B. Hirsch, The Recrystallization Process in Some Polycrystalline Metals, Proceedings of the Royal Society A: Mathematical, Physical and Engineering Sciences 267(1328) (1962) 11-30.

[59] S.V. Raj, G.M. Pharr, A compilation and analysis of data for the stress dependence of the subgrain size, Materials Science and Engineering 81 (1986) 217-237.

[60] J.E. Burke, Some Factors Affecting the Rate of Grain Growth in Metals, Trans. Metall. Soc. AIME 180 (1949).

[61] J.E. Burke, D. Turnbull, Recrystallization and grain growth, Progress in Metal Physics 3 (1952) 220-292.

[62] J.P. Drolet, A. Galibois, The impurity-drag effect on grain growth, Acta Metallurgica 16(12) (1968) 1387-1399.

[63] P. Gordon, T.A. El Bassyoumi, Transactions of the Metallurgical Society of AIME. 223 (1965).

[64] G.F. Bolling, W.C. Winegard, Grain growth in zone-refined lead, Acta Metallurgica 6(4) (1958) 283-287.

[65] H. Hu, Grain growth in zone-refined iron, Can Metall Quart 13(1) (1974) 275-286.

[66] M.P. Anderson, D.J. Srolovitz, G.S. Grest, P.S. Sahni, Computer simulation of grain growth—I. Kinetics, Acta Metallurgica 32(5) (1984) 783-791.

[67] M. Hillert, On the theory of normal and abnormal grain growth, Acta Metallurgica 13(3) (1965) 227-238.

[68] N.P. Louat, On the theory of normal grain growth, Acta Metallurgica 22(6) (1974) 721-724.

[69] I.M. Lifshitz, V.V. Slyozov, The kinetics of precipitation from supersaturated solid solutions, Journal of Physics and Chemistry of Solids 19(1) (1961) 35-50.

[70] P. Feltham, Grain growth in metals, Acta Metallurgica 5(2) (1957) 97-105.

[71] C.W. Zheng, N.M. Xiao, D.Z. Li, Y.Y. Li, Microstructure prediction of the austenite recrystallization during multi-pass steel strip hot rolling: A cellular automaton modeling, Computational Materials Science 44(2) (2008) 507-514.

[72] S. Vervynckt, K. Verbeken, P. Thibaux, Y. Houbaert, Characterization of the Austenite Recrystallization by Comparing Double Deformation and Stress Relaxation Tests, Steel Res Int 81(3) (2010) 234-244.

[73] A.I. Fernandez, B. Lopez, J.M. Rodriguez-Ibabe, Relationship between the austenite recrystallized fraction and the softening measured from the interrupted torsion test technique, Scripta Mater 40(5) (1999) 543-549.

[74] J.S. Perttula, L.P. Karjalainen, Recrystallisation rates in austenite measured by double compression and stress relaxation methods, Mater Sci Tech 14(7) (1998) 626-630.

[75] O. Kwon, A.J. Deardo, On the recovery and recrystallization which attend static softening in hot-deformed copper and aluminum, Acta Metallurgica Et Materialia 38(1) (1990) 41-54.

[76] G. Li, T.M. Maccagno, D.Q. Bai, J.J. Jonas, Effect of initial grain size on the static recrystallization kinetics of Nb microalloyed steels, Isij Int 36(12) (1996) 1479-1485.

[77] M. Maalekian, R. Radis, M. Militzer, A. Moreau, W.J. Poole, In situ measurement and modelling of austenite grain growth in a Ti/Nb microalloyed steel, Acta Mater 60(3) (2012) 1015-1026.

[78] T. Garcin, J.H. Schmitt, M. Militzer, In-situ laser ultrasonic grain size measurement in superalloy INCONEL 718, Journal of Alloys and Compounds 670 (2016) 329-336.

[79] M. Keyvani, T. Garcin, D. Fabregue, M. Militzer, K. Yamanaka, A. Chiba, Continuous Measurements of Recrystallization and Grain Growth in Cobalt Super Alloys, Metall Mater Trans A 48A(5) (2017) 2363-2374.

[80] M. Militzer, T. Garcin, W.J. Poole, In-situ measurements of grain growth and recrystallization by laser ultrasonics, Mater Sci Forum 753 (2013) 25-30.

[81] M. Keyvani, Laser ultrasonic investigations of recrystallization and grain growth in cubic metals, The University of British Columbia, 2018.

[82] N. Legrand, N. Souto, E. Poliak, R. Jacolot, D. Levesque, S. Krueger, Combinning metallurgical models, metallography and laser ultrasonic techniques to monitor steel microstructure evolution at high temperature, Third International Symposium on Ultrasound for Metals, Stockholm, 2017.

[83] X.P. Ma, C.L. Miao, B. Langelier, S. Subramanian, Suppression of strain-induced precipitation of NbC by epitaxial growth of NbC on pre-existing TiN in Nb-Ti microalloyed steel, Materials & Design 132 (2017) 244-249.

[84] C.P. Scott, D. Chaleix, P. Barges, V. Rebischung, Quantitative analysis of complex carbo-nitride precipitates in steels, Scripta Mater 47(12) (2002) 845-849.

[85] J. Bobynko, I. MacLaren, A.J. Craven, Spectrum imaging of complex nanostructures using DualEELS: I. digital extraction replicas, Ultramicroscopy 149 (2015) 9-20.

CHAPTER 2: Effects of solutes and temperature on high-temperature deformation and subsequent recovery in hot-rolled low alloy steels[4]

2.1 Introduction

Thermomechanical controlled processing (TMCP) is a common practice to tailor the microstructural evolution of steels [1-3]. It is well known that grain size refinement is the only way to increase both strength and ductility of steels [4]. Grain refinement can be achieved through properly selected processing parameters, such as deformation temperature, strain rate, inter-pass time, pass strain and alloy chemistry. Hot rolling is the key step of thermomechanical controlled processing. During hot rolling, static recovery and recrystallization, as well as grain growth, occur after hot deformation [5]. These annealing phenomena should be considered deliberately when designing new rolling schedules for rough rolling and finish rolling [6-10].

Microalloyed steels with small addition of niobium can achieve high strength due to grain refinement and precipitation hardening [11, 12]. Recently, new steel designs with relatively high manganese, aluminium and silicon contents are gaining increasing interest in the steel industry. These elements are traditionally added in low concentration (<0.5%Si, <2%Mn, <0.3%Al). At these concentrations, the above additions have less impact on recovery and recrystallization compared to microalloying elements such as Nb, Ti and V or Mo [13, 14]. The effects of Mn, Al and Si on recovery and recrystallization could become significant when their additions are increased substantially. A relatively small number of studies have considered the effect of high alloying additions on recrystallization [13-15], and recovery kinetics. Therefore, the current research was dedicated to investigating the effect of Mn, Al and Si, as well as deformation temperature on the recovery process, and the onset of

---

[4] This chapter is based on the journal publication: S. Liang, F. Fazeli, H.S. Zurob, Effects of solutes and temperature on high-temperature deformation and subsequent recovery in hot-rolled low alloy steels, Materials Science and Engineering: A (2019) 138324.

recrystallization, which is influenced by the preceding recovery process. The subsequent recrystallization kinetics will be modelled and discussed in future works.

2.2 Experimental

Several Fe-C-X ternary alloys (where X = Mn, Si or Al) and the binary Fe-C alloy were studied, and their corresponding compositions are shown in Table 2-1. The base alloy Fe-0.1%C was also studied to provide a reference point. These alloys were prepared by arc melting under vacuum. The melting was performed and repeated four times in order to guarantee the homogeneity of the alloys. The as-cast finger ingot was then sealed in a glass tube under vacuum and then heated up to 1100°C in the austenite temperature region for three days to homogenize the microstructure. After homogenization, the ingots underwent hot rolling to break down the as-cast microstructure. The hot-deformed samples were then machined into cylinders of 5mm diameter and 10mm height.

Table 2-1: Ternary alloys (Fe-C-X, where X = Mn, Si or Al) compositions (in wt%)

Fe-C-Mn	Fe-C-Si	Fe-C-Al
Fe-0.1%C-0.48%Mn	Fe-0.1%C-1.0%Si	Fe-0.1%C-1.0%Al
Fe-0.1%C-1.39%Mn	/	/
Fe-0.1%C-2.76%Mn	/	/

The effect of solutes and temperature on recovery and recrystallization were studied through stress relaxation experiments. For stress relaxation tests, the cylindrical specimens were first heated up to 1100°C for 5 mins for homogenization and then cooled down to the deformation temperature. The temperature was selected according to the austenitization temperatures of each alloy calculated by the Thermo-Calc software [16], as shown in Fig. 2-1(a). Deformation was conducted with a Bahr dilatometer DIL 805. The strain rate was $1s^{-1}$ and the applied strain was 0.25 for all tests. After the deformation and while the specimen was constrained by the anvils, force drop was recorded for 5 mins at the deformation temperature. The detailed conditions are summarized in Fig. 2-1(b).

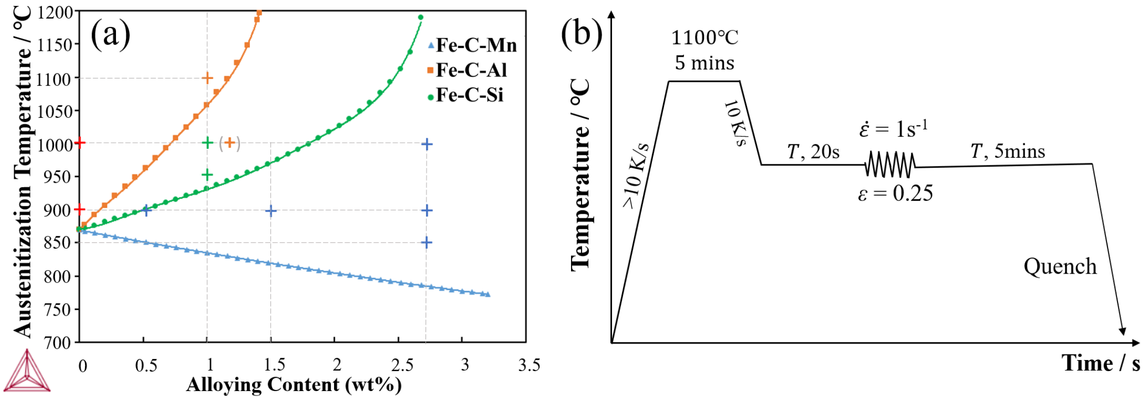

Fig. 2-1: (a) Austenitization temperatures for Fe-C-X systems calculated by Thermo-Calc. Carbon content is 0.1wt% for all alloy systems. The selected testing temperatures are represented by the colored crosses and (b) Deformation scheme for stress relaxation testing by dilatometry (T: deformation temperature).

2.3 Results

2.3.1 Effect of alloying elements

The instantaneous forces were recorded during both the initial deformation step and the subsequent isothermal stress relaxation step. At the deformation temperature of 900°C, the flow stress (at $\varepsilon = 0.25$) for the ternary alloys Fe-0.1%C-y%Mn (y =0, 0.48, 1.39 and 2.76) steels have increased from 141 MPa to 162 MPa with increasing Mn concentration, due to solid solution strengthening, as shown in Fig. 2-2(a). Under current deformation conditions, the stress relaxation curve can be divided into three sections: the gradual decrease stage which corresponds to recovery and creep at the beginning of the stress relaxation, the dramatic drop stage which is due to the occurrence of recrystallization and the last stage after the completion of recrystallization in which stress decreases slightly in general and the governing mechanisms are grain growth and creep. In Fig. 2-2(b), stress decays for ternary alloys Fe-0.1%C-y%Mn (y = 0.48, 1.39 and 2.76) are compared with those of the reference alloy Fe-0.1%C. Firstly, the slopes at recovery stage for all relaxation curves exhibit similar values, but the initial stresses are different. Secondly, the onset of recrystallization is about 0.15 sec for the base alloy and around 0.96 sec for Fe-0.1%C-2.76%Mn alloy. With increasing alloying addition of Mn, the time for the onset of recrystallization increases, as well as the whole recrystallization kinetics.

At 1000°C, ternary alloys with addition of 1.0wt% of Si and Al were studied. From Figs. 2-2(c) ~ (d), similar effects of alloying solutes on flow stress and relaxation curves can be observed. The flow stress (at ε = 0.25) for Fe-0.1%C-1.0%Al is about 140 MPa and the onset of recrystallization is around 0.28 sec, and for Fe-0.1%C base alloy, it is about 110 MPa for the stress and 0.07 sec for the onset of recrystallization. Fe-0.1%C-1.0%Si and Fe-0.1%C-2.76%Mn exhibit intermediate behaviors. The Al solute exhibits strongest effects on work-hardening and onset of recrystallization, compared to Si and Mn. The onsets of recrystallization for all conditions were estimated and presented in Table 2-2.

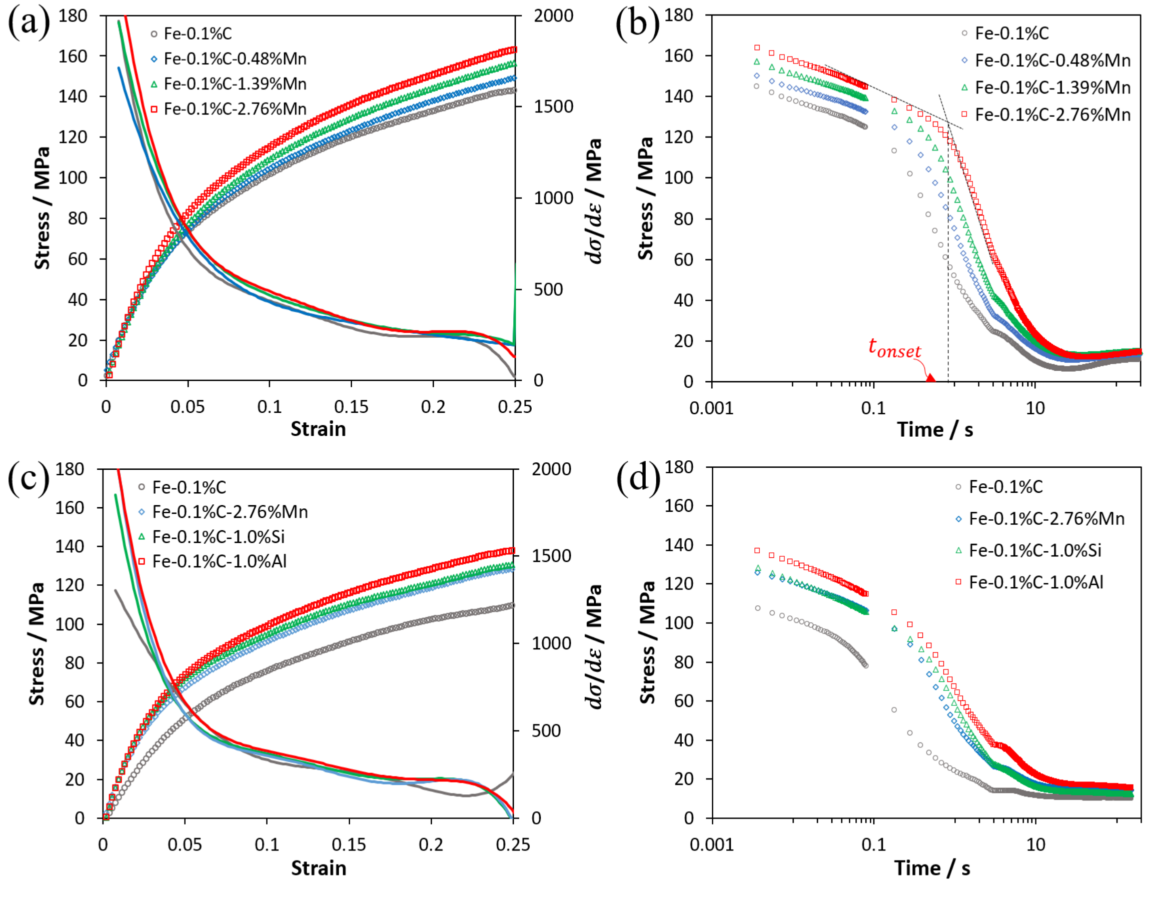

Fig. 2-2: (a) Stress-strain curves and corresponding (of the same color) work-hardening rates and (b) stress relaxation curves for Fe-0.1%C-y%Mn (y: weight percent of Mn) low alloy steels at 900°C; (c) stress strain curves and corresponding (of the same color) work-hardening rates and (d) stress relaxation curves for Fe-0.1%C-y%X (X = Mn, Si or Al, y: weight percent of solutes) low alloy steels at 1000°C. The onset of recrystallization is determined by the intersection of extrapolations from recovery and recrystallization data points, as shown in (b).

2.3.2 Effect of temperature

The effect of temperature on softening kinetics is shown in Fig. 2-3. For the Fe-0.1%C reference alloy in Fig. 2-3(a), the onset of recrystallization occurred at 0.07 sec at 1000℃ and increases to 0.15 sec at 900℃. Similar results for the onset of recrystallization and recrystallization kinetics can be seen for the other three alloys: Fe-0.1%C-2.76%Mn, Fe-0.1%C-1.0%Al and Fe-0.1%C-1.0%Si, as illustrated in Fig. 2-3(b) to Fig. 2-3(d). The time for the onset of recrystallization of each condition can be found in Table 2-2. To be mentioned, the whole recrystallization kinetics is delayed as the temperature decreases.

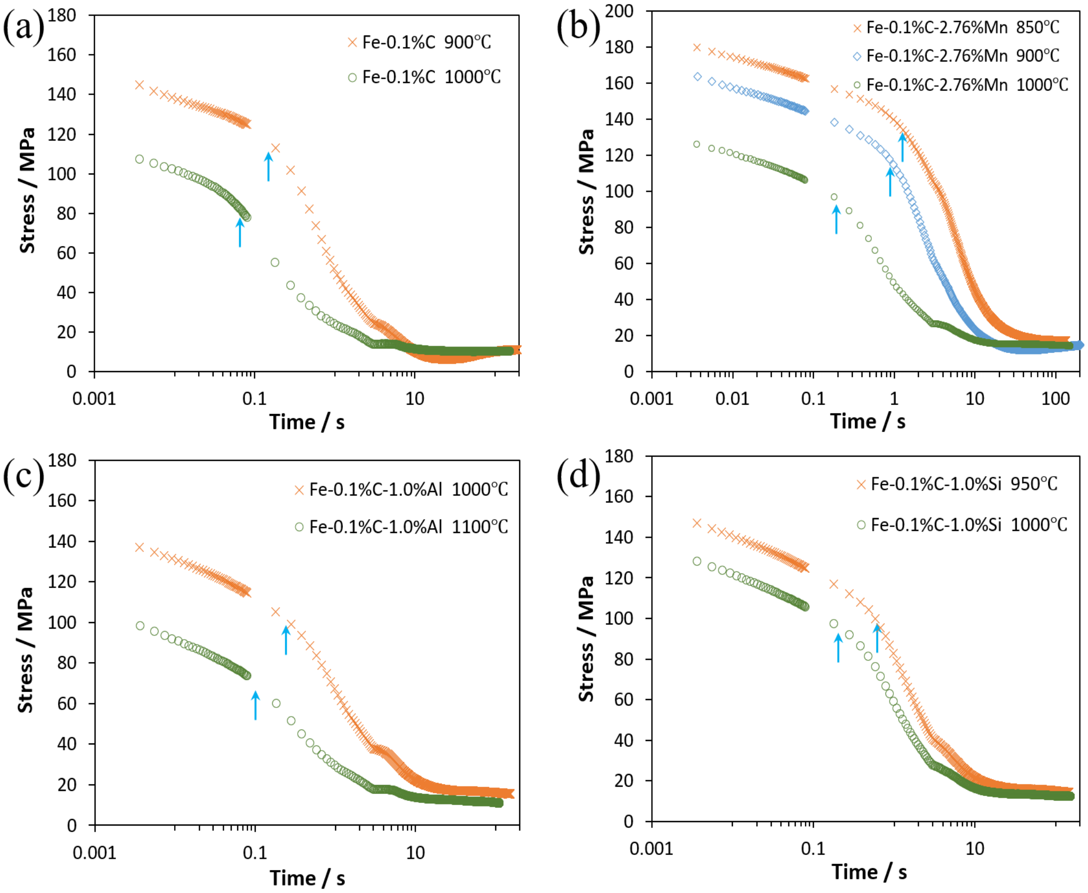

Fig. 2-3: Stress relaxation curves at various deformation temperatures for alloys: (a) Fe-0.1%C; (b) Fe-0.1%C-2.76% Mn; (c) Fe-0.1%C-1.0%Al and (d) Fe-0.1%C-1.0%Si. Temperatures are shown together with the legend. The arrows indicate the onset of recrystallization for each condition.

Table 2-2: Estimated time for the onset of recrystallization (in seconds)

	850℃	**900℃**	**950℃**	**1000℃**	**1100℃**
Fe-0.1%C		$0.15\,^{-0.01}_{+0.03}$		$0.07\,^{-0.01}_{+0.03}$	
Fe-0.1%C-0.48%Mn		$0.28\,^{-0.01}_{+0.03}$			
Fe-0.1%C-1.39%Mn		$0.50\,^{-0.03}_{+0.09}$			
Fe-0.1%C-2.76%Mn	$1.20\,^{-0.06}_{+0.18}$	$0.96\,^{-0.05}_{+0.15}$		$0.20\,^{-0.01}_{+0.03}$	
Fe-0.1%C-1.0%Si			$0.75\,^{-0.04}_{+0.12}$	$0.20\,^{-0.01}_{+0.03}$	
Fe-0.1%C-1.0%Al				$0.28\,^{-0.01}_{+0.03}$	$0.13\,^{-0.01}_{+0.03}$

Note: The lower and upper bounds of onsets are represented by " - " and " + " signs.

2.3.3 Fitting with recovery model

Recovery can be fast or sluggish depending on annealing temperatures and be retarded due to the pinning of small dispersed particles [5, 9]. Recovery kinetics can also be altered, to some extent, by solutes (e.g. [17]). During recovery, dislocations annihilate and dislocation cells and subgrains form subsequently. The motion of dislocations is almost always obstacle-limited. Obstacles may include other dislocations, solutes, precipitates and grain boundaries [18]. During the creep of materials, the strain rate, $\dot{\gamma}$, is related to the mobile dislocation density ρ_m and the average velocity of dislocations $\bar{v}$:

$$\dot{\gamma} = \rho_m b \bar{v} \qquad (2-1)$$

where, b is the magnitude of the Burgers vector. Nes [19] claimed that the rate controlling mechanism for recovery is the glide of jogged screw dislocations and the average migration rate of dislocations is given as:

$$\bar{v} = 2b\upsilon_D \exp\left(\frac{-U_0}{kT}\right) \sinh\left(\frac{Fbl_j}{kT}\right) \qquad (2-2)$$

where, υ_D is the Debye frequency, U_{sa} is expected to be of the order of the activation energy for bulk diffusion of the solute, F is the force per unit length and l_j is the dislocation jog separation distance. According to the theory, Verdier et al [20] derived the equation for the internal stress relaxation corresponding to dislocation annihilation and rearrangement. The changing rate of the internal stress is related to the plastic relaxation strain rate $\dot{\varepsilon}_p$ and the rate equation is:

$$\frac{d\sigma_i}{dt} = -\frac{64}{9{M_T}^3{\alpha_T}^2}\frac{\sigma_i^2}{E}\upsilon_D \exp\left(\frac{-U_0}{kT}\right)\sinh\left(\frac{\sigma_i V}{kT}\right) \qquad (2-3)$$

where, σ_i is the internal stress due to dislocations, M_T is the Taylor factor, α_T is a constant of the order of 0.15, E is the Young's modulus (or elastic modulus), υ_D is the Debye frequency, k is the Boltzmann constant, U_0 and V are the activation energy and activation volume, respectively. The Verdier et al [20] recovery model was adopted for the current study. The input parameters used in the model are presented in Table 2-3. Following the obstacle theory for the deformation mechanisms [18], dislocation jogs, solutes and temperature effect were considered through the activation volume term V, while the value of the activation energy was set equal to that for self-diffusion of austenite.

Table 2-3: Recovery model parameters

Parameter	**Value**
Activation energy, U_0	285,000 J/mole [21]
Alpha factor, α_T	0.15 [8]
Debye frequency, υ_D	2×10^{12} s^{-1} [8]
Taylor factor, M_T	3.1
Shear modulus, μ	$81 \times 10^9[0.91 - (T(K) - 300)/1810]$ Pa [18]

The activation volume was adjusted to best fit the data as a function of dislocation density, solute content and temperature, leading to the following semi-empirical expression:

$$V = b^3/[0.45b\sqrt{\rho} + 0.042(C_{Nb})^{0.3333} + 0.0035(C_{Mn})^{0.5} + 0.0075(C_{Al})^{0.3333} + 0.0058(C_{Si})^{0.3333} + (4700.00 - 2.5T) \times 10^{-5}] \qquad (2-4)$$

where, b is the Burgers vector, ρ is the dislocation density, C_i is the alloying composition of Nb, Mn, Al and Si in wt%, and T is the temperature in Kelvin.

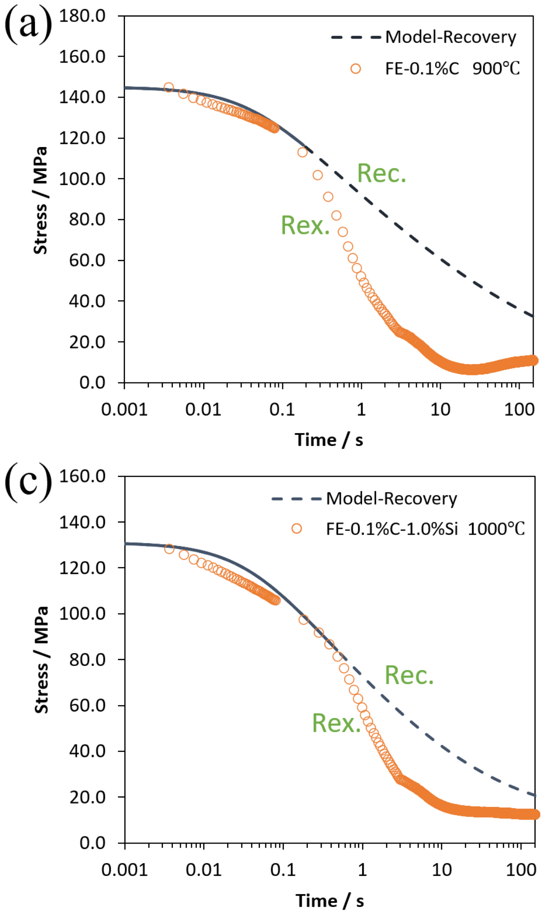

Fig. 2-4: Recovery data fitting using Verdier et al [20] recovery model for a) alloy Fe-0.1%C at 900℃; b) alloy Fe-0.1%C-2.76% Mn at 900℃; (c) alloy Fe-0.1%C-1.0%Al at 1000℃ and (d) alloy Fe-0.1%C-1.0%Si at 1000℃. The solid part of the recovery model curve was attempted to fit the experimental recovery data and the dotted part represents the stress behavior if no recrystallization occurs. (Rec.: recovery; Rex.: recrystallization)

As can be seen, increased dislocations and solutes create more pinning centres and thus reduce the activation volume. However, higher temperatures tend to increase the activation volume. The recovery model was applied to fit the initial portion of the stress relaxation curves. The model results are shown with solid lines in Fig. 2-4. Additional comparisons of the experimental and modeling results are provided in Appendix V.

2.4 Discussion

2.4.1 Effect of solutes and temperature on high temperature flow behavior

In Figs. 2-2(a) ~ (c), the flow stresses for all alloys are compared at 900°C and 1000°C. With increasing Mn content, flow stress increases at a specific strain. Stress increase is larger for larger strains suggesting that Mn addition not only increases the yield stress, but also the rate of work-hardening. This is likely due to the enhanced interactions between solutes and dynamic recovery of dislocations during deformation [22-24]. Solutes in solution tend to retard the dynamic recovery process. As can be seen in Fig. 2-2(a), the work-hardening rate is largest for the Fe-0.1%C-2.76wt%Mn alloy and lowest for the reference alloy. It increases with increasing Mn contents. In Fig. 2-2(c), similar effects can be observed when alloys Fe-0.1%C-1.0%Si and Fe-0.1%C-1.0%Al were investigated at 1000°C. Based on these results, Al has the strongest solid solution strengthening effect (per mass%) and it leads to the greatest increase in the work-hardening rate, followed by Si and then Mn. This could be partially due to the large atomic radius difference between Al (0.143 nm) and Fe (0.124 nm) [4]. The local stress field created by the substitutional Al atoms interacts with edge dislocations (either attraction or repulsion), leading to the increase of yielding stress and retardation of dynamic recovery during deformation.

In order to examine the effect of temperature, the stress-strain curves and corresponding work-hardening curves at 900°C and 1000°C are compared for the Fe-0.1%C and Fe-0.1%C-2.76%Mn alloys as plotted in Fig. 2-5. As expected, both the flow stress and work-hardening rate are higher at lower temperatures, because dynamic recovery is undoubtedly facilitated at high temperatures.

2.4.2 Effect of solutes and temperature on recovery

As mentioned earlier in Section 2.3.3, the strain rate is related to the average velocity of dislocations, which is frequently determined by the strength and density of discrete obstacles [18]. Such obstacles can be precipitates, forest dislocations or solutes. Effects of obstacles are considered through the activation volume term V which was formulated as

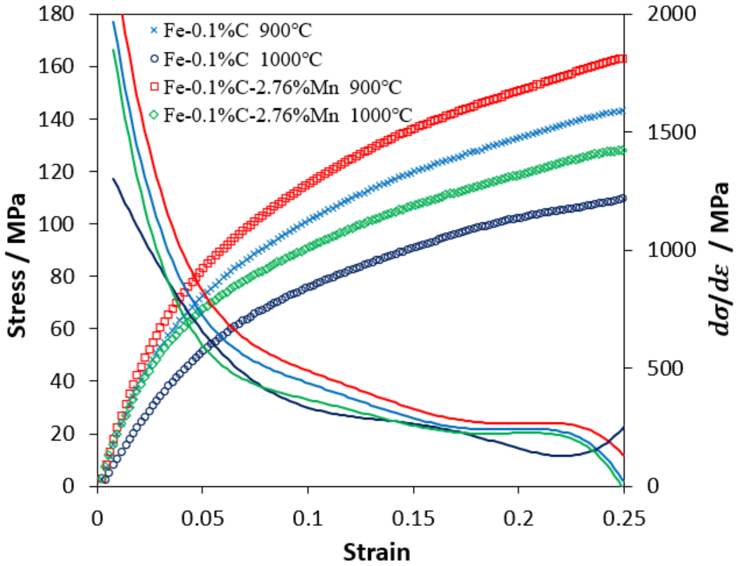

Fig. 2-5: Stress-strain curves and work-hardening curves for alloys Fe-0.1%C and Fe-0.1%C-2.76%Mn at 900°C and 1000°C. The work-hardening rate curves are present with the same color for corresponding stress strain curves.

Eq. $(2-4)$. Alternatively, some researchers have already accounted for the effect of solute contents by adjusting the value of activation energy (e.g. [25]). Unfortunately, the apparent measured values, which fell between 400 and 800 kJ/mole, can not be reconciled with any physical mechanisms. As stated by Nes [19], the activation energy, U_{sa}, is expected to be of the order of the activation energy for bulk diffusion of the solute, which is approximately 285 kJ/mol for austenite [21]. Therefore, the activation volume, which is broadly defined as the rate of decrease of activation enthalpy with respect to flow stress at fixed temperature [26], is more suitable for considering alloying effects. Nes [19] also argued that jog spacing, l_j, is expected to be proportional to the initial dislocation density. And the increasing activation length/volume with increasing temperature has been observed experimentally for α-iron [27, 28] and magnesium [29], which is consistent with our current research findings. As we can see in Eq. $(2-4)$, the activation volume is a function of dislocation density, solute concentration and annealing temperature. For high dislocation density in the microstructure, there are more dislocation jogs acting as the obstacles for the motion of dislocation and thus slow down the kinetics. Similarly, solutes will interact with dislocations and generate resistance to dislocation movement. Therefore, higher dislocation density and solute concentrations give smaller activation volume and as a result the stress relaxation rate will be lowered. However, temperature exhibits the opposite behavior, i.e. higher temperature renders more extended activation volume.

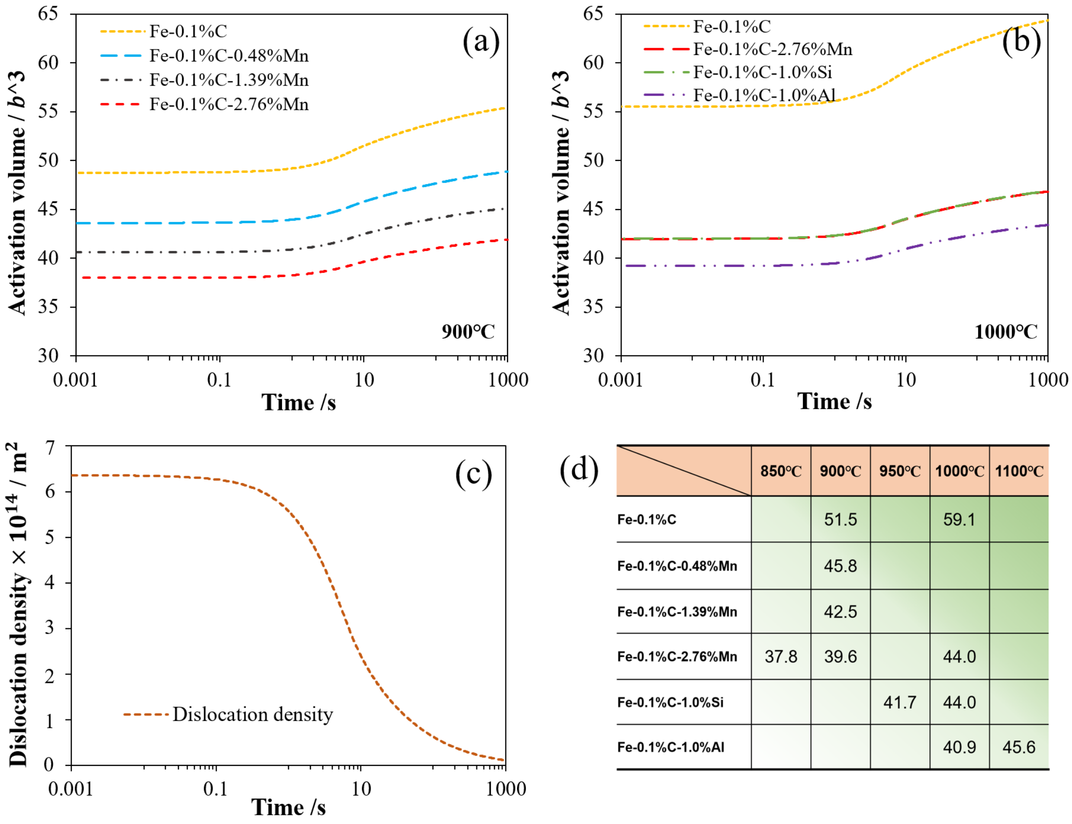

	850℃	900℃	950℃	1000℃	1100℃
Fe-0.1%C		51.5		59.1	
Fe-0.1%C-0.48%Mn		45.8			
Fe-0.1%C-1.39%Mn		42.5			
Fe-0.1%C-2.76%Mn	37.8	39.6		44.0	
Fe-0.1%C-1.0%Si			41.7	44.0	
Fe-0.1%C-1.0%Al				40.9	45.6

Fig. 2-6: Activation volume as a function of dislocation density, temperature and alloying contents: (a) activation volume of ternary alloys at 900°C; (b) activation volume of ternary alloys at 1000°C; (c) a typical dislocation density evolution during annealing used for activation volume calculations in (a) and (b); and (d) summary of the average activation volumes (divided by b^3) for alloys and temperatures.

The activation volumes for all alloys and temperatures were plotted and illustrated in Fig. 2-6. In Fig. 2-6(a), with increasing manganese alloying at 900°C, the activation volume decreases consistently. In contrast, the activation volumes of alloys Fe-0.1%C and Fe-0.1%C-2.76%Mn are increased when temperature is increased to 1000°C. At 1000°C, the activation volumes of alloy Fe-0.1%C-1.0%Si and Fe-0.1%C-1.0%Al are smaller than that of alloy Fe-0.1%C-2.76%Mn (in Fig. 2-6(b)), which indicates that Si and Al are more prominent effect on recovery than Mn. For both cases at 900°C and 1000°C, activation volumes increase with time due to the annealing-out of dislocations (as shown in Fig. 2-6(c)). The average activation volumes for all six alloys are tabulated in Fig. 2-6(d) and the trends of activation volume changes due to alloying elements and temperatures can be observed.

2.4.3 Effect of solutes and temperature on the onset of recrystallization

Microstructural evolution of cells/subgrains is of great importance for the Strain Induced Boundary Migration (SIBM) mechanism of recrystallization [5]. A small number of subgrains become viable, strain-free nuclei successively during the recovery process. The nuclei then start to grow into the interior of the deformed original grain, marking the onset of recrystallization. However, the subgrain growth kinetics will be affected by the solutes and temperature (through the activation volume in the recovery model). The lower the temperature and richer the solute content, the more sluggish the subgrain growth. Thus, the time for the onset of recrystallization will be increased due to the slow down of subgrain growth.

The onset of recrystallization tabulated in Table 2-2 for all the conditions is in consistent with the trend of the activation volume in Fig. 2-6(d); the larger for activation volume, the shorter for the onset of recrystallization. This can be understood in Fig. 2-7 schematically, according to Zurob et al [10]. Based on Bailey and Hirsh's nucleation criteria [30], the critical subgrain size is proportional to the inverse of the stored energy that is related to the activation volume during recovery. The higher for activation volume, the smaller for the stored energy and the larger for the critical subgrain size (case I). For case II with lower activation volume, the nucleation onset would be earlier (point 2') if the subgrain coarsening kinetics were not altered. However, in fact, the subgrain kinetics will slow down due to smaller activation volume or lower mobility [31, 32]. Therefore, it is believed that solutes as well as annealing temperatures can retard the cell structures/subgrains evolution and, as a result, the onset of recrystallization is postponed.

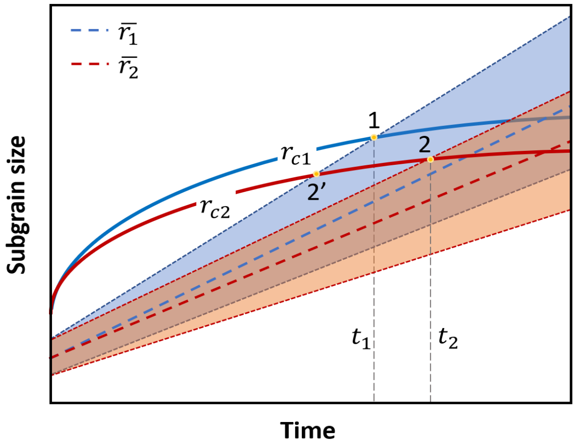

Fig. 2-7: Subgrains coarsening and critical subgrain size evolution for two distinct activation volume scenarios. The activation volume is larger in case I compared to case II. Solid lines represent critical subgrain size satisfying Bailey and Hirsh's criteria. Dotted lines show subgrain size coarsening during annealing. The shaded areas indicate a Rayleigh distribution of subgrain size. Nucleation onsets earlier in case I (at point 1) than case II (at point 2) ($t_1 < t_2$).

2.5 Conclusions

The alloying effects of Mn, Si and Al on the high temperature flow stress, recovery and the onset of recrystallization have been investigated.

1) A pragmatic formulation for activation volume term was developed that accounts for the effect of solute content and temperature on the recovery kinetics.

2) Lower temperatures or richer solute concentration will retard recovery and mitigate dynamic recovery during hot deformation.

3) The effects on recovery process of studied elements suggest that Al has the most prominent effect (per mass%) and the weakest effect for Mn.

4) The time for the onset of recrystallization varies depending on the degree of recovery. Generally, higher temperatures or less alloying elements lead to shorter transition time from recovery to recrystallization. This suggests that during nucleation, recovery helps recrystallization, in contrast to growth conditions where recovery and recrystallization compete for the stored energy.

2.6 Reference

[1] S. Vervynckt, K. Verbeken, B. Lopez, J.J. Jonas, Modern HSLA steels and role of non-recrystallisation temperature, International Materials Reviews 57(4) (2012) 187-207.

[2] M. Cabibbo, A. Fabrizi, M. Merlin, G.L. Garagnani, Effect of thermo-mechanical treatments on the microstructure of micro-alloyed low-carbon steels, J Mater Sci 43(21) (2008) 6857-6865.

[3] S.V. Subramanian, M.K. Rehman, H. Zurob, C. Shang, Recrystallization and grain coarsening control in processing high niobium microalloyed line pipe steels, Mater Sci Forum 753 (2013) 391-396.

[4] W.D. Callister, D.G. Rethwisch, Materials science and engineering : an introduction, 2014.

[5] F.J. Humphreys, M. Hatherly, Recrystallization and Related Annealing Phenomena, Pergamon, Oxford, 1996.

[6] J.W. Bowden, F.H. Samuel, J.J. Jonas, Effect of interpass time on austenite grain refinement by means of dynamic recrystallization of austenite, Metallurgical Transactions A 22(12) (1991) 2947-2957.

[7] Q.Y. Sha, Z.Q. Sun, L.F. Li, Refinement of coarse grained austenite in Nb-V-Ti microalloyed steel during roughing rolling, Ironmaking & Steelmaking 42(1) (2015) 74-80.

[8] H.S. Zurob, C.R. Hutchinson, Y. Bréchet, G. Purdy, Modeling recrystallization of microalloyed austenite: effect of coupling recovery, precipitation and recrystallization, Acta Mater 50(12) (2002) 3075-3092.

[9] H.S. Zurob, Effects of precipitation, recovery and recrystallization on the microstructural evolution of the microalloyed austenite, McMaster University, 2003.

[10] H.S. Zurob, Y. Bréchet, J. Dunlop, Quantitative criterion for recrystallization nucleation in single-phase alloys: Prediction of critical strains and incubation times, Acta Mater 54(15) (2006) 3983-3990.

[11] T. Gladman, The physical metallurgy of microalloyed steels, The Institute of Materials, London, 1997.

[12] X.P. Ma, C.L. Miao, B. Langelier, S. Subramanian, Suppression of strain-induced precipitation of NbC by epitaxial growth of NbC on pre-existing TiN in Nb-Ti microalloyed steel, Materials & Design 132 (2017) 244-249.

[13] S.F. Medina, J.E. Mancilla, Influence of Alloying Elements in Solution on Static Recrystallization Kinetics of Hot Deformed Steels, Isij Int 36(8) (1996) 1063-1069.

[14] H. Andrade, M. Akben, J. Jonas, Effect of molybdenum, niobium, and vanadium on static recovery and recrystallization and on solute strengthening in microalloyed steels, Metallurgical Transactions A 14(10) (1983) 1967-1977.

[15] S.H. Cho, K.B. Kang, J.J. Jonas, Effect of manganese on recrystallisation kinetics of niobium microalloyed steel, Mater Sci Tech 18(4) (2013) 389-395.

[16] Thermo-Calc software package, http://www.thermocalc.com/, 2018.

[17] L. Backe, Modeling the Effect of Solute Drag on Recovery and Recrystallization during Hot Deformation of Nb Microalloyed Steels, Isij Int 50(2) (2010) 239-247.

[18] H.J. Frost, M.F. Ashby, Deformation-mechanism maps : the plasticity and creep of metals and ceramics, Pergamon Press, Oxford, 1982.

[19] E. Nes, Recovery revisited, Acta Metallurgica Et Materialia 43(6) (1995) 2189-2207.

[20] M. Verdier, Y. Bréchet, P. Guyot, Recovery of AlMg alloys: Flow stress and strain-hardening properties, Acta Mater 47(1) (1998) 127-134.

[21] J. Fridberg, L.E. Torndahl, M. Hillert, Diffusion in iron, Jernkont. Ann. 153 (1969) 263.

[22] I. Westermann, K.O. Pedersen, T. Furu, T. Borvik, O.S. Hopperstad, Effects of particles and solutes on strength, work-hardening and ductile fracture of aluminium alloys, Mechanics of Materials 79 (2014) 58-72.

[23] A. Shadkam, C.W. Sinclair, The coupled effect of grain size and solute on work hardening of Cu-Ni alloys, Philosophical Magazine Letters 95(12) (2015) 555-563.

[24] A. Yoshie, T. Fujita, M. Fujioka, K. Okamoto, H. Morikawa, Formulation of flow stress of Nb added steels by considering work-hardening and dynamic recovery, Isij Int 36(4) (1996) 467-473.

[25] F.G. Arieta, C.M. Sellars, Activation volume and activation-energy for deformation of Nb HSLA steels, Scripta Metallurgica Et Materialia 30(6) (1994) 707-712.

[26] R.J. Asaro, S. Suresh, Mechanistic models for the activation volume and rate sensitivity in metals with nanocrystalline grains and nano-scale twins, Acta Mater 53(12) (2005) 3369-3382.

[27] R.W. Evans, L.A. Simpson, The strain-rate sensitivity of the plastic properties of α-iron at high temperatures, The Philosophical Magazine: A Journal of Theoretical Experimental and Applied Physics 19(160) (1969) 809-819.

[28] K.K.M. Pandey, O. Prakash, B. Bhattacharya, Variation of activation volume with temperature for Fe, Si, and Ge, Materials Letters 57(26-27) (2003) 4319-4322.

[29] G.B. Gibbs, Creep and stress relaxation studies with polycrystalline magnesium, Philosophical Magazine 13(122) (1966) 317.

[30] J.E. Bailey, P.B. Hirsch, The recrystallization process in some polycrystalline metals, Proceedings of the Royal Society of London. Series A. Mathematical and Physical Sciences 267(1328) (1962) 11-30.

[31] M.K. Rehman, H.S. Zurob, A Novel Approach to Model Static Recrystallization of Austenite During Hot Rolling of Nb Microalloyed Steel. Part I: Precipitate-Free Case, Metall Mater Trans A 44a(4) (2013) 1862-1871.

[32] M. Winning, A.D. Rollett, G. Gottstein, D.J. Srolovitz, A. Lim, L.S. Shvindlerman, Mobility of low-angle grain boundaries in pure metals, Philosophical Magazine 90(22) (2010) 3107-3128.

CHAPTER 3: NbC precipitation during multi-pass deformation of a nickel-based model alloy: experiments and modelling[5]

3.1 Introduction

The precipitation of microalloyed carbonitrides plays an important role in the thermomechanical processing of High Strength Low Alloy (HSLA) steels [1-7]. The formation of a high number density of precipitates leads to the retardation of both recovery and recrystallization by pinning both the dislocation substructure and the grain boundaries during thermomechanical controlled processing (TMCP) [8]. In order to evaluate the softening kinetics during TMCP, it is necessary to capture the time evolution of precipitation during multi-pass rolling.

Microalloying elements such as niobium, titanium or vanadium are added to form carbides, nitrides and/or carbonitrides with carbon and nitrogen [9]. It is found that these carbides, nitrides and/or carbonitrides exhibit "*cube-on-cube*" orientation relationships (OR) [10] with the austenite. These precipitates are incoherent with the matrix due to the large lattice misfit between the precipitates and austenite (~15% in the case of VN to ~25% in the case of NbC [11]). The precipitation of microalloyed carbonitrides occurs heterogeneously on defects such as grain boundaries and dislocations. Strain-induced precipitation refers to the formation of microalloyed carbonitrides on the dislocations formed during thermomechanical processing.

After a single pass deformation, precipitates nucleate and grow on the available dislocations within the microstructure. Depending on the interpass time, precipitate coarsening can also take place [12, 13]. Precipitation interacts with recovery, recrystallization

---

[5] This chapter is based on the journal publication: S. Liang, X. Wang, H.S. Zurob, NbC precipitation during multi-pass deformation of a nickel-based model alloy: experiments and modelling, Materials Science and Engineering: A (2019) 138748.

and grain growth [11, 14] during further annealing. The interactions can be complicated during multi-pass deformation. After the first deformation pass, precipitates nucleate and grow on the dislocation network. The second pass leads to the formation of new dislocations which interact with existing precipitates and potentially provide nucleation sites for new precipitates. A second wave of precipitates may then nucleate on the freshly created dislocations. The new precipitates are potentially in competition with existing precipitates. To begin with, the existing precipitates deplete the available solute within their immediate vicinity, and this makes the area around the existing precipitates a less attractive nucleation site. In addition, if a significant size difference exists between the existing and new precipitates, the existing precipitates may cause the new precipitates to dissolve once the diffusion fields of the two kinds of precipitates interact (similar to Ostwald ripening [8]). Similar interactions can occur for the third and later passes. Nagarajan et al [15, 16] investigated the precipitation kinetics of a Fe-30%Ni model alloy subjected to two-pass compression tests. It was found that the second pass deformation seemed to be accommodated by the first generation of microbands by adding more dislocations into them, instead of creating new microbands structures. The new dislocations can be potential nucleation sites for another class of precipitates newly formed. However, this has not been covered and discussed in their work.

In order to gain a better understanding of the precipitation behavior under multi-pass deformation conditions, austenitic model alloys comparable to low alloy austenite were needed. Charnock and Nutting [17] used thermionic electron emission microscopy to measure the number of annealing twins in Fe-Ni alloys at 1000°C and related this to the stacking fault energy at that temperature. Based on this work, an Ni-30%Fe alloy would have the same stacking fault energy (SFE, ~60-70 mJ/m^2) as low alloy steel at hot-rolling temperature. Moreover, according to Hurley [18], the hot-deformation flow curves of the Ni-30%Fe model alloy were similar to those of low carbon steel with respect to the shape of the curve and critical features such as peak strain. It is, therefore, plausible to select the Ni-30%Fe model alloy to mimic austenite during hot deformation. The aim was to examine the microstructure such as microbands after room-temperature deformation, as well as both precipitate size and spatial distributions in the matrix during annealing, using transmission electron microscopy (TEM). A precipitation model was applied to simulate the nucleation, growth and coarsening of the precipitates during multi-pass deformation and annealing processes. Mechanical properties such as flow behavior and microhardness were also included and discussed.

3.2 Experimental

The present work was carried out using an austenitic nickel-based model alloy (Ni-30wt%Fe-0.33wt%Nb-0.03wt%C). In such a model alloy, austenite is retained down to room temperature. Therefore, the dislocation structure formed during hot/cold deformation can be preserved, which makes it possible to study the interactions between dislocations and precipitates. The as-received hot-rolled material was machined into cylindrical tensile samples with 4.08 mm diameter and a gauge length of 20 mm.

Specimens were deformed at a strain rate of 0.001 s^{-1} with an Instron tensile testing machine at room temperature, which avoids the heat effects in hot-deformation and quench process. After each deformation pass, the specimen was subjected to annealing at 700℃ in a tube furnace with different holding times followed by water quenching. The detailed deformation and annealing conditions for each pass, as well as, their corresponding sample labels are listed in Table 3-1. The temperature of 700℃ was chosen in order to avoid recrystallization during annealing. In this way, it is possible to focus on the interaction between recovery and precipitation during multi-pass rolling. A second deformation pass was applied to specimens that have been annealed at 700℃ for 45 mins (F3). The third deformation pass was applied to sample that was annealed for 60 mins at 700℃ following the second deformation pass (S3). The deformation and annealing history of all samples is summarized in Table 3-1 and alternatively in Appendix VI.

Table 3-1: Deformation and annealing time (with sample labels) for three passes at 700°C

	Deformation strain	**Annealing Time / mins**
First-pass	0.15	0 (F1), 5 (F2), 45 (F3), 45+60 (F4)
Second-pass	0.10	0 (S1), 5 (S2), 60 (S3), 60+60 (S4)
Third-pass	0.07	0 (T1), 5 (T2), 60 (T3), 60+60 (T4)

Note: Annealing time "0" indicates the as-deformed states for all three passes.

The holding times between deformation passes were selected based on preliminary calculations (referred to Section 3.3.3) which suggested that 45 mins of holding after the first deformation pass would have about 30 percent of total equilibrium precipitation volume fraction formed thus leaving a significant driving force for precipitation during the subsequent deformation pass. The holding time after the second deformation pass would consume more than 75 percent of total equilibrium precipitation volume fraction. Thus, after the third deformation pass, the supersaturation would decrease further, leading to the onset of coarsening which would make it possible to investigate the precipitate interactions under coarsening conditions.

Vickers microhardness (Hv) was measured for each annealing condition with a load of 300 grams. TEM foils were prepared by sectioning the tensile samples parallel to the longitudinal direction, grinding down to below 100 µm in thickness and finally twin-jet electropolishing in a solution of 5% perchloric acid in methanol at -30°C and 35 Volts. For carbon replica, the samples were polished with 1µm diamond paste and slightly etched with 4% nital solution, followed by a carbon layer coating under vacuum. Carbon coatings were then detached by dissolving the matrix and picked up with copper grids. TEM observations were performed with Philips CM12 and JOEL 2010F TEMs operating at 120 kV and 200 kV, respectively.

3.3 Results

3.3.1 Mechanical Properties

The engineering and true stress-strain curves for three passes deformed at room temperature are plotted in Fig. 3-1(a). Vickers microhardness was measured for the as-received, as-deformed and annealed conditions, and the microhardness versus annealing time is plotted in Fig. 3-1(b). As we can see, the as-received material is relatively soft with a hardness of 159 Hv. The hardness increased to 213 Hv after first pass deformation (F1) and then dropped to 202 Hv with 5 mins annealing at 700°C (F2), however, the hardness increased again to 220 Hv with 45 mins annealing time (F3). A similar hardness behavior can be observed for the second pass (S1 to S3). However, for the third pass, the hardness for T3 after 60 mins annealing at 700°C is lower than that of T2. The dashed lines in Fig. 3-1(b) represent the extended annealing conditions (F4, S4 and T4, all with additional 1hr annealing). The changes of microhardness ΔHv as shown in the Fig. 3-1(b) indicate the work-hardening after each pass deformation.

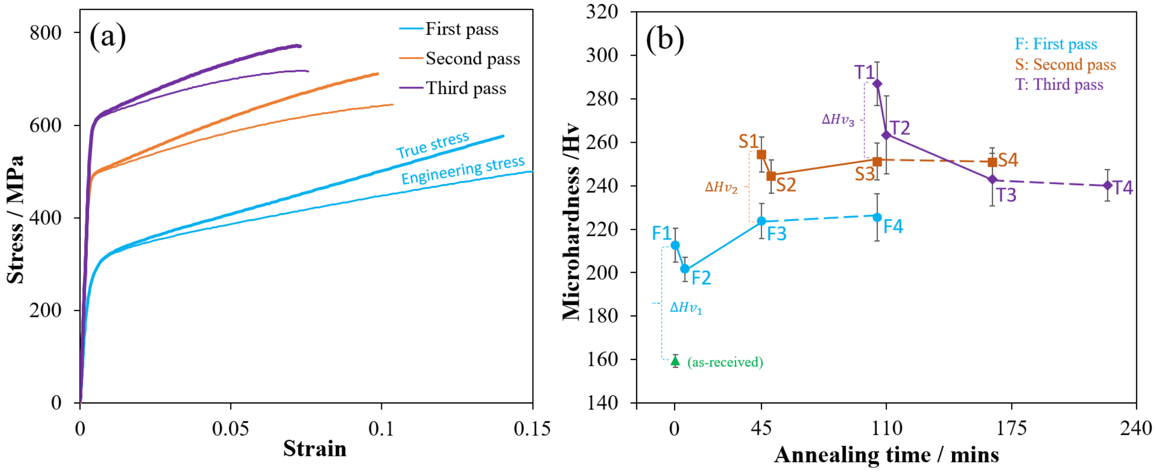

Fig. 3-1: (a) Engineering stress-strain curves and (b) microhardness measurements for the as-received (green triangle), first-pass (F1 to F3), second-pass (S1 to S3) and third-pass (T1 to T3) conditions. Annealing time is specified for each condition, time zero means the as-received or as-deformed states. (10 ~ 15 measurements were conducted for each point and error bar is referred to the standard deviation of measurements). The change of microhardness due to deformation has also been illustrated for each pass.

3.3.2 Microstructure

3.3.2.1 Dislocation structures

Dislocations structures for the first and second passes have been examined with TEM. In the as-deformed state (a strain of 0.15) for the first pass, band structures and tangled dislocations were largely observed as shown in Fig. 3-2. Band structures were inevitably formed on primary slip {111} planes as confirmed by diffraction patterns (Fig. 3-2(a)). The band structures or slip traces exhibited orthogonal and hexagonal patterns when viewed near the <001> and <111> zone axes (Fig. 3-2(b) and Fig. 3-2(c)). The thickness of the bands varies roughly from 0.1 to 0.5 μm. Occasionally, dislocations tended to form the cell-like structures as presented from Fig. 3-2(d) to Fig. 3-2(f). Individual dislocations can be seen between bands and inside cell structures.

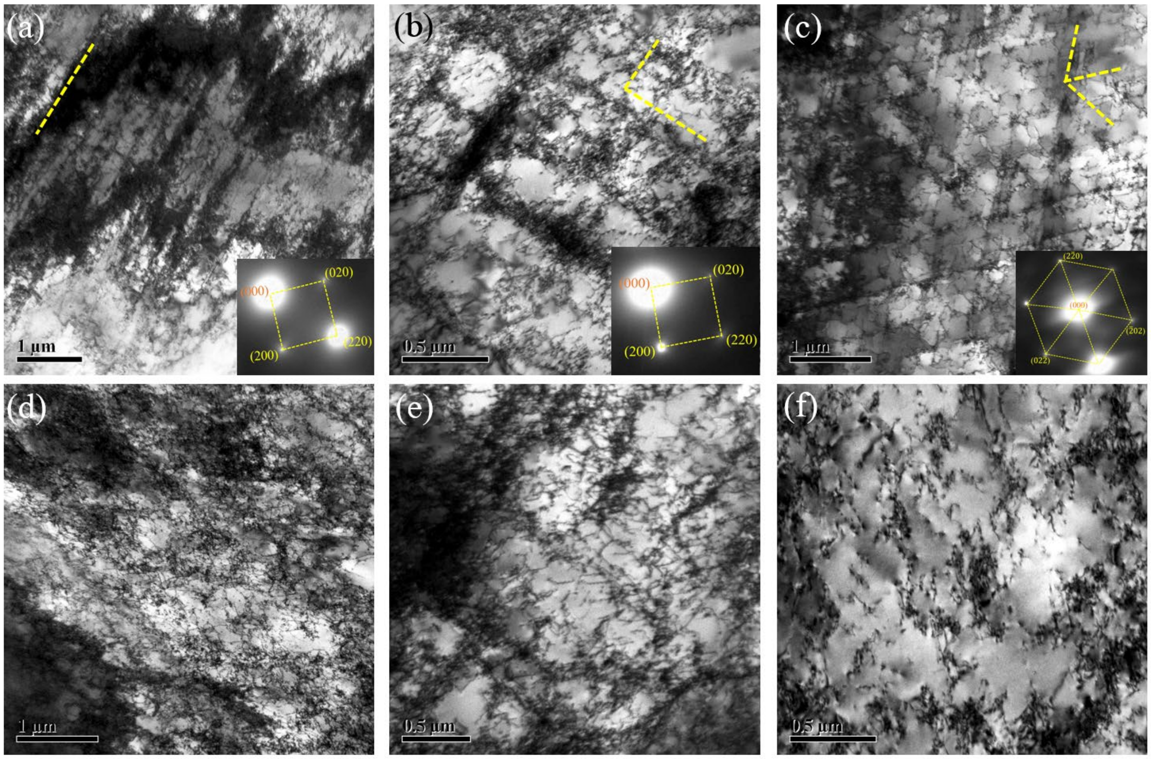

Fig. 3-2: Dislocation structures in the as-deformed state (F1): (a) single band structure along {111} plane (near [001] zone axis); (b) orthogonal bands (near [001] zone axis); (c) hexagonal slip traces in {111} planes (near [111] zone axis) and (d)-(f) dislocation tangles with cell structure formation tendency. The dashed lines indicate {111} plane traces.

After annealing for 5 mins at 700℃, dislocations were partially annealed out and the band structures formed during deformation became diffused as shown in Fig. 3-3(a) and Fig. 3-3(b). Multiple diffused bands at low magnification were observed in the sample annealed for 45mins at 700℃ (Fig. 3-3(c)). The second pass deformation with a strain of 0.10 was applied to the annealed condition of 45 mins at 700℃ (F3) of the first pass. Dislocations density was substantially increased by comparing Fig. 3-3(c) and Fig. 3-3(d). Cell structure size formed for the second pass is much smaller than that in as-deformed state in the first pass (Fig. 3-2(e) and Fig. 3-3(e)). With annealing for 60 mins at 700℃, dislocation density decreased, and the diffused band structures were also observed (Fig. 3-3(f)). It seems that a relatively large cell-like structure formed.

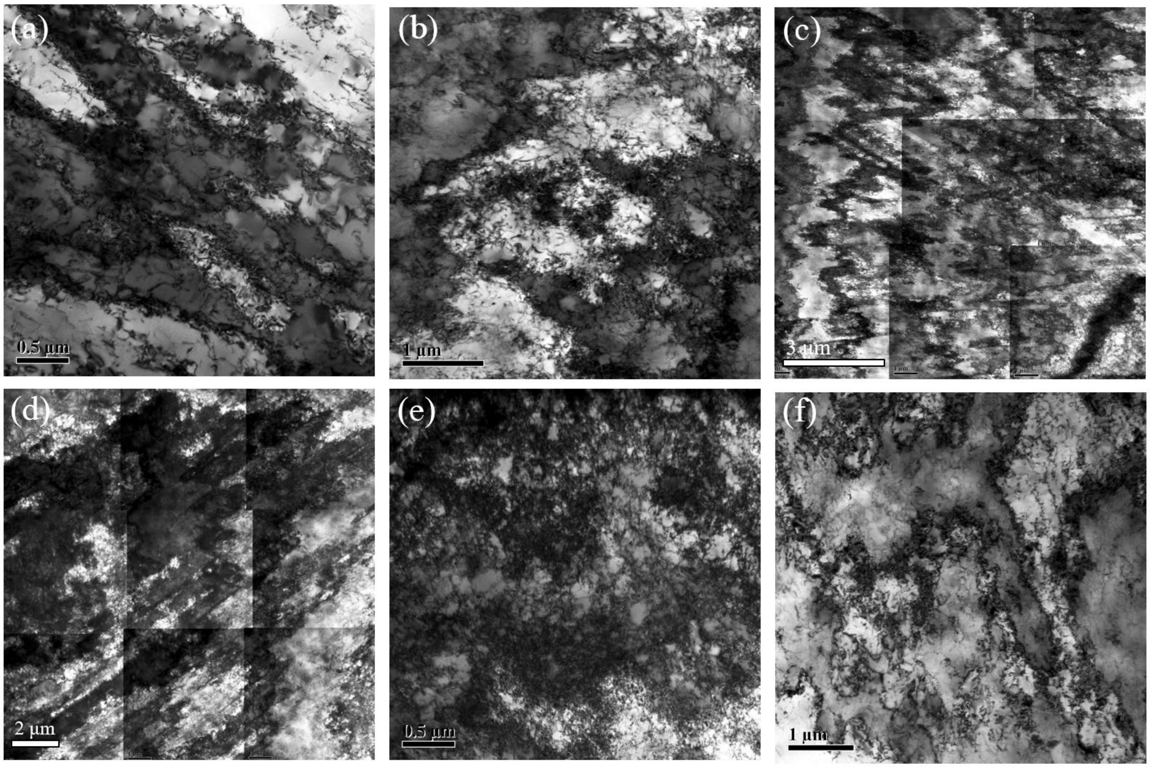

Fig. 3-3: Dislocation and band structures after annealing for the first pass: (a)-(b) annealed for 5mins at 700℃ (F2) and (c) annealed for 45mins at 700℃ (F3). And for the second pass: (d)-(e) as-deformed (S1) and (f) annealed for 60mins at 700℃ (S3).

3.3.2.2 Strain-induced precipitation

The spatial distribution of precipitates was investigated for the first pass and second pass conditions. It can be concluded that most precipitates formed preferentially on the dislocations and within band walls (Fig. 3-4(a) and Fig. 3-4(b)). In order to confirm the precipitate distribution, pairs of bright and dark field images of the precipitates were obtained as shown in Figs. 3-4(c) ~ (f). From the diffraction patterns, the "*cube-on-cube*" orientation relationship (OR) was verified for all precipitates with respect to the matrix. The crystallographic {111} planes were marked in each micrograph as a reference. It must be mentioned that precipitates were still aligned with the primary slip {111} plane even after the annealing-out of dislocations inside the band walls (Fig. 3-4(b)).

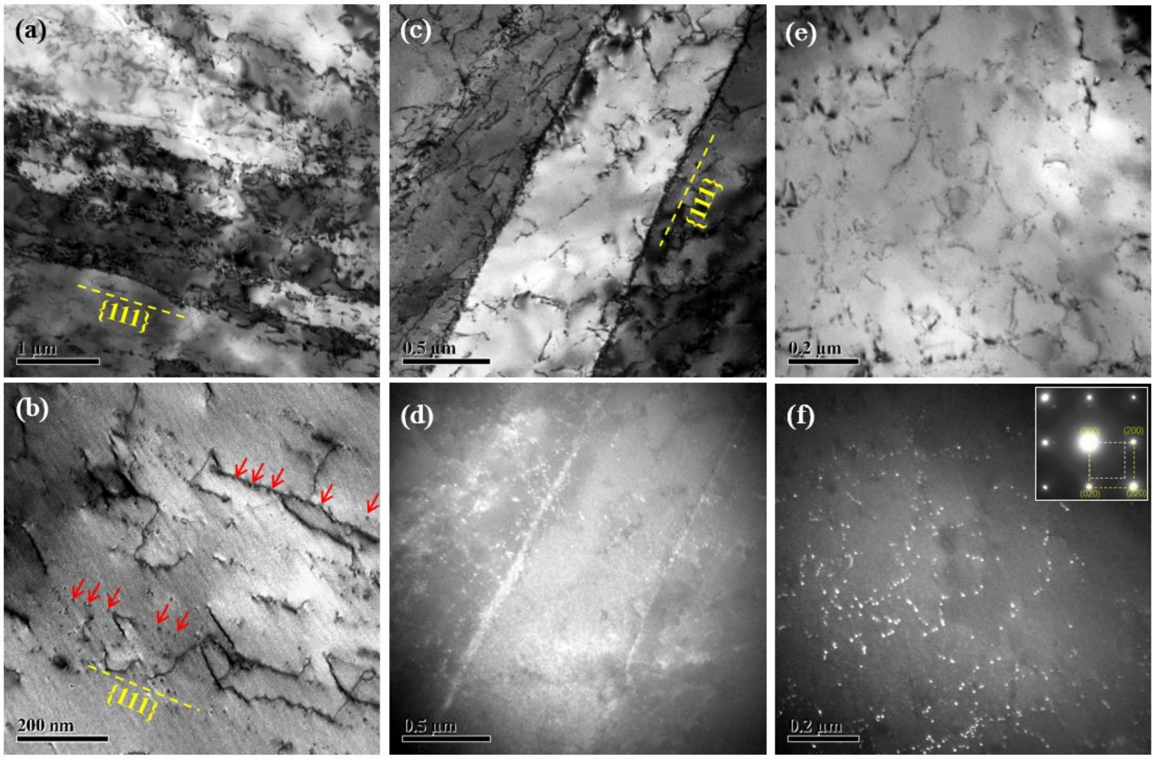

Fig. 3-4: Precipitate distributions for condition F3 (a ~ d): (a) precipitates located inside microbands; (b) precipitates aligned with {111} plane (e.g. as shown by red arrows); (c) bright field of dislocations and a band structure; (d) dark field micrograph of precipitate in (c). For condition S2 (e ~ f): (e) bright field of precipitates on random dislocations and (f) dark field micrograph of (e). The dotted yellow lines indicate the primary {111} slip planes.

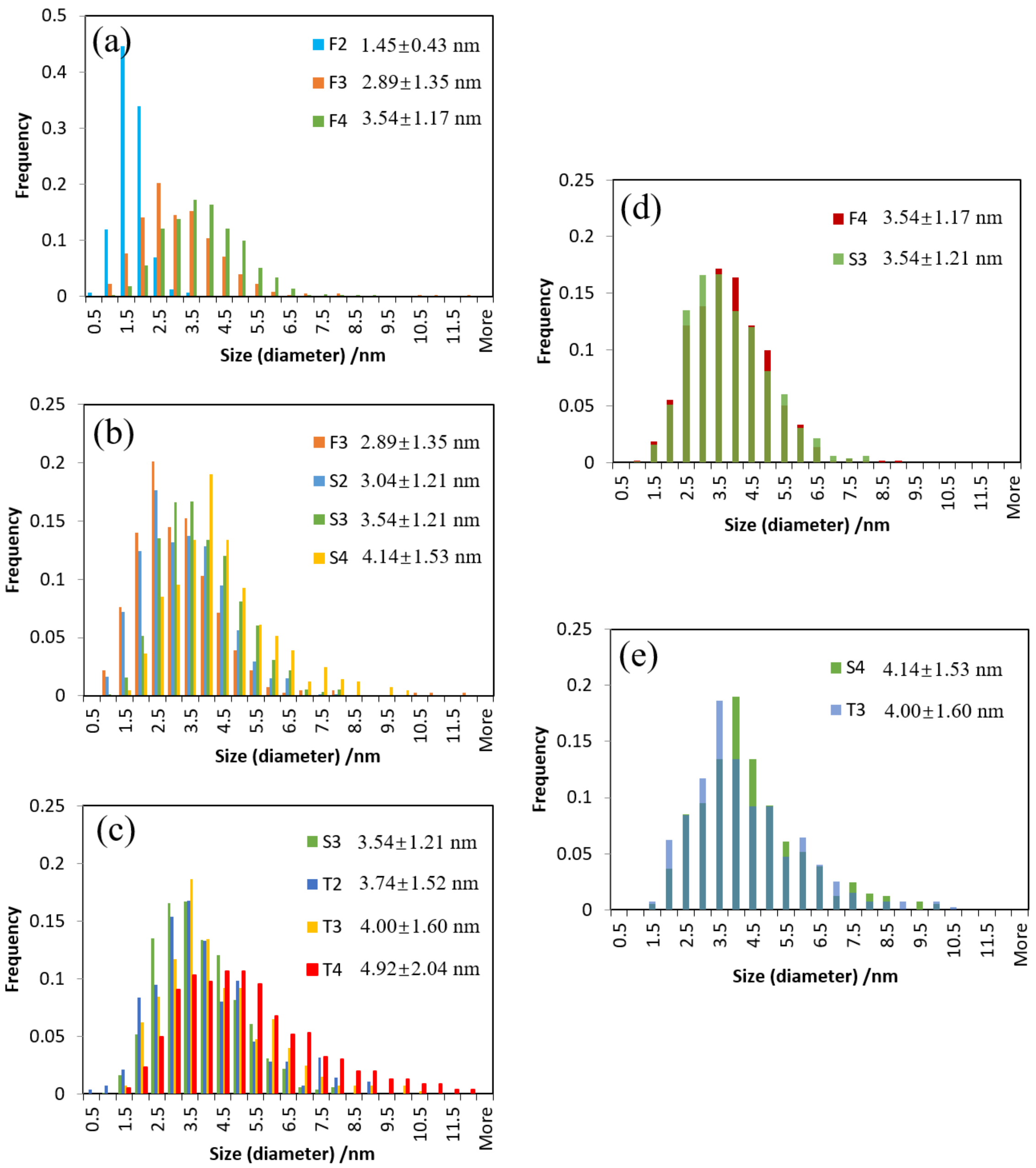

Fig. 3-5: Precipitate size distributions by TEM carbon replica measurement for: (a) the first pass annealing; (b) the second pass annealing with F3 as the reference distribution; (c) the third pass annealing with S3 as the reference distribution; (d) comparison between F4 and S3(same annealing time but with/without the second pass deformation) and (e) comparison between S4 and T3(same annealing time but with/without the third pass deformation).

Precipitate size distribution was studied by the TEM carbon replica technique. More than 400 particles were counted for each condition. From the results in Fig. 3-5, the average particle size after one deformation pass was 1.45 nm for the specimen annealed for 5 mins at 700°C and increased to 2.89 nm (Fig. 3-5(a)) after 45 mins annealing. For the second pass, the particle size distribution profile shifted to the right bringing the average from 2.89 nm to 3.54 nm (Fig. 3-5(b)). The size increased from 3.54 nm to 4.00 nm for the third pass after 60 mins annealing (Fig. 3-5(c)). Additional 1 hr annealing for each pass (F4, S4 and T4) were also included, in order to investigate the effect of deformation as shown in Fig. 3-5(d) and Fig. 3-5(e). The size distributions for F4-S3 and S4-T3 are almost identical to each other. Examples of carbon replica for each condition can be found in Appendix VI.

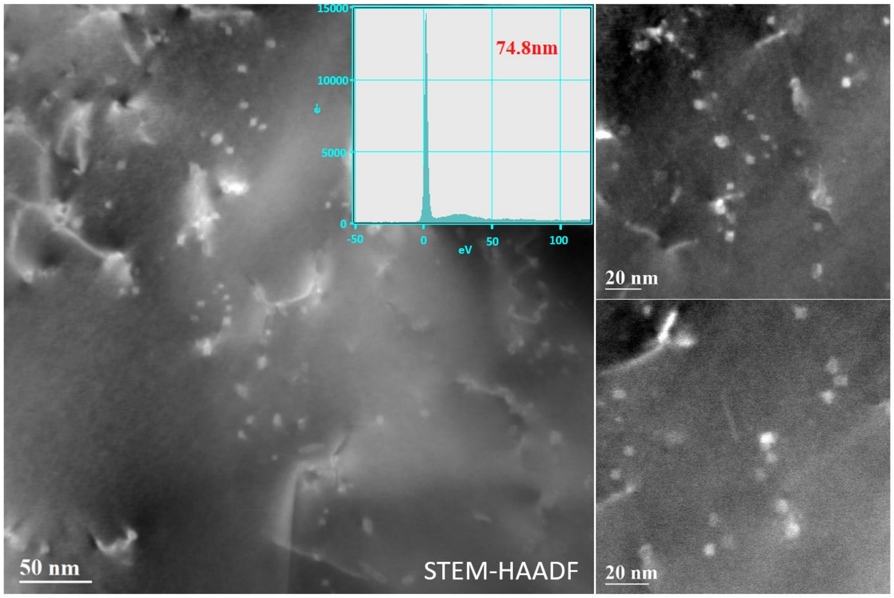

Fig. 3-6: Precipitate number density measurement for F3 with high angle annular dark field (HAADF) in scanning TEM mode (STEM). The thickness was measured with electron energy loss spectrum (EELS). The embedded spectrum plots the number of electrons in each electron energy window.

The number density of precipitates was estimated using high angle annular dark field analysis in scanning TEM mode (STEM-HAADF) which captures the scattered electrons at high angles due to the larger atomic number (***Z***) of niobium. In Fig. 3-6, the bright spots are NbC precipitates in the Nickel-based alloy. The thickness was measured with the TEM-EELS Log-Ratio technique by counting the total and zero-loss electrons in the EEL spectrum [19]. The average thickness of the sample in the regions of interest is about 75nm (ranging from 60 to 90 nm). With the number of particles counted in each view, the average number density of precipitates is estimated to be around $(2.00 \pm 0.49\ ) \times 10^{22}/m^3$. More detailed information can be found in Appendix VI.

3.3.3 Modeling of precipitation kinetics

TEM observations confirmed the nucleation of precipitates on individual dislocations and on microbands. The precipitation kinetics will be modelled using the classical model with an initial stage of nucleation and growth followed by a stage of growth and coarsening [12, 13]. The criterion proposed by Deschamps and Bréchet [12] for the transition from nucleation-growth to growth-coarsening stage was adopted.

3.3.3.1 Nucleation and growth

The nucleation rate is obtained from the classical theory of nucleation as:

$$\frac{dN}{dt}|_{nucleation} = (N_{tot} - N)Z\beta^* \exp\left(-\frac{\Delta G^*}{kT}\right) \exp\left(-\frac{\tau}{t}\right) \qquad (3-1)$$

$$N_{tot} = 0.5\rho^{1.5} \qquad (3-2)$$

$$\beta^* = \frac{4\pi(r^*)^2 CD}{a_0^4} \qquad (3-3)$$

where, N is the number of precipitates per unit volume, t is the time, N_{tot} is the total number of nucleation sites (i.e. dislocation nodes) per unit volume, Z is the Zeldovich factor which is approximately 1/20, β^* is the atomic impingement rate, ΔG^* is the activation energy of the critical nucleus, k_b is the Boltzmann constant, T is the temperature in Kelvin, τ is the incubation time for nucleation taken to be zero considering that heterogeneous nucleation is almost an instantaneous process requiring no incubation time, ρ is the dislocation density, r^* is the radius of the critical size for precipitation nucleation, a_0 is the lattice parameter of austenite, and C and D are the bulk concentration and diffusivity of the major microalloying element, respectively.

The aforementioned critical energy barrier ΔG^* can be calculated numerically from the free energy balance ΔG between the chemical free energy, the interfacial free energy and the elastic energy of the dislocation The formulation used by Zurob et al [11] is given below as:

$$\Delta G = V\Delta G_V + A\gamma - \left(\frac{\mu b^2 r\ \ln\left(\frac{r}{b}\right)}{2\pi(1-\nu)} + \mu b^2 r/5\right) \qquad (3-4a)$$

where, V is the volume of the transformed nucleus, ΔG_V is the chemical free energy difference per unit volume of the transformation, μ is the shear modulus, b is the Burgers vector, r is the radius of precipitates, ν is the Poisson's ratio, A and γ are the surface area and surface energy of the nucleus, respectively. The chemical driving force for carbonitride can be calculated with respect to solubility products as:

$$\Delta G_V = -\frac{RT}{V_P} ln \frac{C_{Nb}[C_C]^x[C_N]^{1-x}}{[K_{NbC}]^x[K_{NbN}]^{1-x}x^x(1-x)^{1-x}} \qquad (3-4b)$$

where, R is the gas constant, x is the site fraction of carbon in the interstitial sublattice, V_P is the molar volume of the precipitate, C_i is the instantaneous concentration of element i in austenite, K_{NbC} and K_{NbN} are the solubility products for NbC and NbN.

At the nucleation and growth stage, the instantaneous number density of nuclei can now be obtained from the integration of the nucleation rate dN/dt. The growth of the nuclei is controlled by the diffusion of microalloying element Nb. The growth rate is given by [11, 13] as:

$$\frac{dr}{dt}|_{growth} = \frac{D_{eff}}{r}\frac{C_{Nb}-C_{Nb}^r}{C_{Nb}^P-C_{Nb}^{Eq}} + \frac{1}{N}\frac{dN}{dt}(\alpha r^* - r) \qquad (3-5)$$

$$D_{eff} = D_{pipe}\pi R_{core}^2\rho + D_{bulk}(1-\pi R_{core}^2\rho) \qquad (3-6)$$

where, D_{eff} is the effective diffusion coefficient, and C_{Nb}^{r}, C_{Nb}^{P} and C_{Nb}^{eq} denote the Nb concentration in equilibrium with a precipitate particle of radius r, the Nb concentration of the precipitate and the Nb concentration in equilibrium with a planar precipitate, respectively. The first term in Eq. $(3-5)$ is the standard diffusion controlled growth law for a spherical particle [20] and the second term is the rate of change of the average particle radius resulting from the nucleation of dN new particles of size αr^* during time dt [11, 12], α is taken as 1.05 in the model. D_{eff} is an average of the pipe diffusion coefficient D_{pipe} and the bulk diffusion coefficient D_{bulk}, depending on the dislocation density ρ and the cross-section area of the dislocation core πR_{core}^2.

3.3.3.2 Growth and coarsening

The growth rate in Eq. $(3-5)$ is driven by the supersaturation of solute in the matrix. In the coarsening stage, the average precipitate size will increase as a result of the size-driven competition between individual precipitates. Following Deschamps and Bréchet [12], the rate of change of particle size during coarsening was given as [11]:

$$\frac{dr}{dt}|_{coarsen.} = \frac{D_{eff}}{r}\,\frac{C_{Nb}^{r}-C_{Nb}^{27r/23}}{C_{Nb}^{P}-C_{Nb}^{Eq}} \qquad (3-7)$$

$$\frac{dN}{dt}|_{coarsen.} = \frac{dr}{dt}|_{coarsen.}\cdot\left[\frac{r^*C_{Nb}}{r(C_{Nb}^{P}-C_{Nb})}\left(\frac{3}{4\pi r^3}-2N+\frac{4\pi r^3N^2}{3}\right)-3\mathrm{N}\right] \qquad (3-8)$$

Under conditions of simultaneous growth and coarsening, the average rate of changes of particle size and number density of nuclei are given below as:

$$\frac{dr}{dt} = (1-f_{coarse})\frac{dr}{dt}|_{growth} + f_{coarse}\frac{dr}{dt}|_{coarsening} \qquad (3-9)$$

$$\frac{dN}{dt} = f_{coarse}\frac{dN}{dt}|_{coarsening} \qquad \left(\frac{dN}{dt}|_{growth}=0\right) \qquad (3-10)$$

$$f_{coarse} = 1-\mathrm{erf}\left(4\left(\frac{r}{r^*}-1\right)\right) \qquad (3-11)$$

The precipitation modeling was then implemented at 700°C for the Ni-based model alloy. The average precipitate size evolution as well as the number density and volume fraction has been plotted in Fig. 3-7. The experimentally measured average size and number density (for condition F3) were included for comparison and the results showed good agreements between experimental measurements and model predictions.

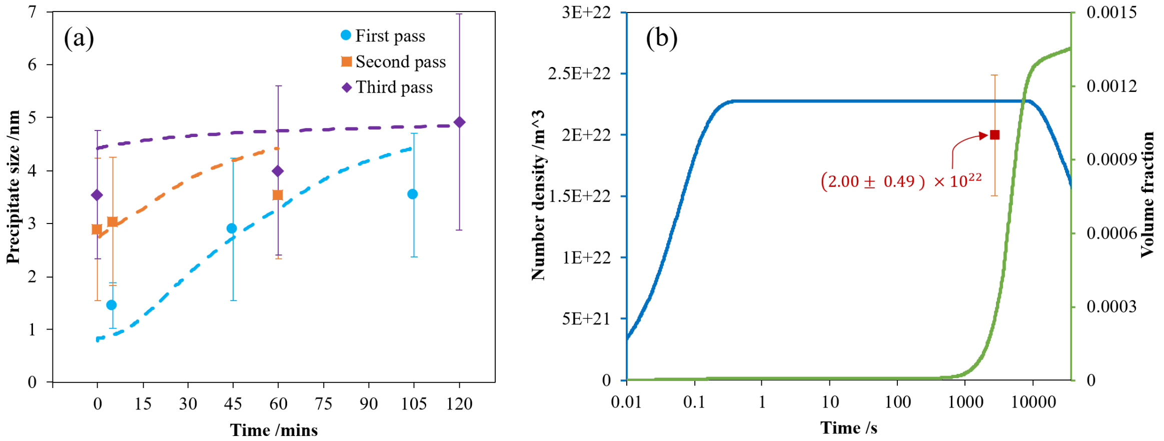

Fig. 3-7: (a) Modelled (dashed lines) and measured average precipitate size comparison for three passes and (b) volume fraction and number density of precipitate predicted by the model and the number density estimated with TEM-STEM for condition F3 has also been included.

3.4 Discussions

3.4.1 Microstructure evolution

For materials having medium to high stacking fault energies, slip is the major deformation mode. Dislocations glide on primary {111} slip planes (for FCC crystals) in order to accommodate the plastic strain locally. Low energy dislocation structure (LEDS) can develop as described by Kuhlmann and Wilsdorf [21]. As can be seen from TEM observations (Fig. 3-2), an important feature of the microstructure is the presence of microbands varying from 0.1 to 0.5 μm in thickness, which contain two dense dislocation walls (DDWs) [22-26]. Dislocation tangles/cells structures can also be observed frequently.

These observations are consistent with those of Wang et al [27] who studied the formation of microbands as a function of grain size and deformation temperatures. It is worth mentioning that the formation of microbands exists in both cell-forming [28] and non-cell-forming microstructures [22]. Relatively large grain size and low temperatures of the material will favor the microbands formation according to [27]. Moreover, microbands can develop into cell-like structure with post-annealing at elevated temperature. Our results show that with post-annealing at 700℃, the microband walls become more diffuse due to the thermally activated climb of dislocations which is accompanied with the formation of cell-like low energy dislocation structure (LEDS). In Fig. 3-3(b), for example, two adjacent microbands walls started to coalescent and form a cell-like structure.

3.4.2 Strain-induced precipitation

As confirmed by TEM observations, the orientation relationship (OR) between NbC precipitates and the austenite phase is the so-called "*cube-on-cube*" OR [10]. However, the lattice mismatch between NbC and austenite is about 25% [11]. As a result, the nucleation energy barrier will be lowered if precipitates form on dislocations due to the released elastic energy of dislocations. As a result, NbC precipitates nucleate heterogeneously on defects such as dislocations and grain boundaries. As mentioned in Section 3.4.1, microbands contain dense dislocation walls (DDWs) which become the preferred precipitation nucleation sites, as shown in Figs. 3-4(a) ~ (d). In Fig. 3-4(b), sets of precipitates were aligned parallel to the trace of the primary {111} slip planes which indicates that these precipitates originally formed on dislocations inside the microband walls, but these dislocations probably were annealed-out during the subsequent annealing steps. Further bright field and dark field analysis (Fig. 3-4(c) and Fig. 3-4(d)) of microbands revealed that precipitates are usually located on the microbands walls. The precipitates can also be located on randomly distributed dislocations within the microstructure as shown in Figs. 3-4(e) ~ (f).

From the precipitate size distribution in Fig. 3-5, the average diameter of the precipitates increases from 1.45 to 3.54 nm during annealing after the first pass, from 2.89 to 4.14 nm during annealing after the second pass and from 3.54 to 4.92 nm during annealing after the third pass. The number density of precipitates was estimated, using STEM-HAADF, to be $(2.00 \pm 0.49\,) \times 10^{22}/m^3$. A classical precipitation model by Deschamps and Bréchet [12] was adopted to simulate the kinetics at 700°C. The precipitate size and number density predicted by the model showed good agreements with those measured by TEM as presented in Fig. 3-7. As a result, the volume fraction of precipitates was estimated to be about 0.0014 which is close to 0.0015 calculated by the thermodynamic software Thermo-Calc [29]. This calculation further confirmed that both the precipitate size evolution and number density should be reasonable.

3.4.3 Microhardness evolution

The change of microhardness resulted from interactions between dislocations and precipitates during both deformation and annealing. After each deformation pass, dislocation densities were increased as reflected by the flow stresses and microhardness in Fig. 3-1. When exposed to annealing at 700°C, microhardness for all three passes decreased at 5 mins. This is mainly due to the annealing-out of dislocations (e.g. F1 to F2). The microhardness started to increase for the first pass which should be related to the growth of the existing precipitates. It can be rationalized by the increase of the average precipitate size from both experimental measurements and model predictions in Fig. 3-7(a). For the initial 5 mins annealing time, the strength increment due to the growth of precipitates was much less than that caused by the annealing-out of dislocations, leading to the drop of the microhardness. However, with further annealing, the precipitation hardening took over and strength/hardness started to increase (e.g. F2 to F3). Similar trend was observed for the second pass annealing after deformation.

For the third pass, the microhardness, on the contrary, kept decreasing with further annealing, which is thought to be related to the coarsening of precipitates. With solute being consumed by the growth of precipitates, the supersaturation of solutes was depleted and the coarsening of precipitates should occur spontaneously because of the Gibbs-Thomson effect [30]. As we can see from Fig. 3-7(b), the precipitation model predicted that the transition from the growth to coarsening stage is about 8300 secs (or 138 mins), which means the coarsening was the dominant microstructure evolution event after the third pass deformation (occurred after about 30 mins of annealing at 700°C). Therefore, it seems to be quite reasonable to observe the continuous decrease of the microhardness following the third pass.

3.4.4 Interactions between deformation, annealing and precipitation

The aim of the current study was to understand the precipitation behavior during multi-pass deformation. The formation of precipitates has only been observed after the first deformation. This is evident by comparing the size distribution of precipitates of conditions F2, S2 and T2, annealed for 5 mins at 700°C (Fig. 3-5(a) to Fig. 3-5(c)). The evolution of distributions indicates a continuous growth of existing precipitates and that a wave of newly formed ones was not presented for subsequent passes. It seems that there is not enough solute supersaturation for triggering the nucleation for later passes. The solubility temperature of NbC in the model alloy drops from 806°C (1st pass), 793°C (2nd pass) to 778°C (3rd pass), which was calculated with Thermo-Calc software using the solute concentrations predicted by the precipitation model. The nucleation rates for all three passes were plotted in Fig. 3-8 and it confirms the low nucleation rates after the second and third passes. Furthermore, Nagarajan et al [15, 16] argued that flow localization would not favour the formation of new precipitates because most new nucleation sites will be located close to the first group of precipitates, around which the supersaturation could be lower than the average.

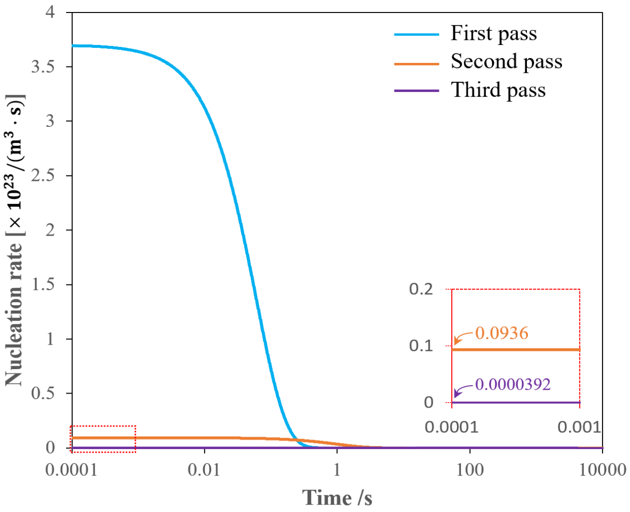

Fig. 3-8: Nucleation rates predicted by the model for three passes at 700℃. The inset (for enlargement) shows nucleation rates for the second and third passes. The area under the curve indicates the number density of precipitates.

The extended annealing conditions (F4, S4 and T4) were designed to investigate the effect of deformation. By comparing F4 and S3 one can determine, for the same total annealing time, what effect the application of a second deformation pass had on the kinetics. Similarly, comparing S4 and T3 provides an insight into the effect of the third deformation pass. For F4-S3, the precipitate size distributions of these two conditions are almost identical to each other. The difference in microhardness is thus solely due to increased dislocation density. For S4-T3, the precipitate size distributions are similar but the micro-hardness of T3 is slightly lower than that of S4 which might indicate that the dislocation network could help the coarsening of precipitates. With long time annealing, the walls or boundaries of microbands are getting diffused and gradually the microstructure tends to evolve toward cell-like structures as seen, for instance, in Fig. 3-3(c) and Fig. 3-3(f). These trends are due to the accelerated dislocation climb at elevated temperatures. The dislocations inside the walls can recover readily, but precipitates will stay aligned as they were (see Fig. 3-4(b)).

3.5 Conclusion

Precipitation behavior in a nickel-based alloy during multi-pass deformation has been investigated. The interactions between deformation, annealing and precipitation were studied using TEM and microhardness tests. The results were summarized as followed:

1. The microstructural features after deformation are microbands, cell structures and dislocation tangles.
2. Precipitation heterogeneously nucleates on randomly distributed dislocations or microbands. The typical "*cube-on-cube*" orientation relationship between precipitates and the matrix has been observed. The formation of precipitates was observed only after the first pass during the multi-pass deformation and annealing process.
3. Deformation will facilitate nucleation and growth of precipitates. Recovery will always decrease the hardness by the annealing-out of dislocations. However, precipitation could strengthen the material if precipitation coarsening is not dominant.
4. The size and number density of precipitates were measured quantitatively which show good agreements with the precipitation model predictions.

3.6 Reference

[1] X.P. Ma, C.L. Miao, B. Langelier, S. Subramanian, Suppression of strain-induced precipitation of NbC by epitaxial growth of NbC on pre-existing TiN in Nb-Ti microalloyed steel, Materials & Design 132 (2017) 244-249.

[2] P. Gong, E.J. Palmiere, W.M. Rainforth, Dissolution and precipitation behaviour in steels microalloyed with niobium during thermomechanical processing, Acta Mater 97 (2015) 392-403.

[3] C. Solenthaler, M. Ramesh, P.J. Uggowitzer, R. Spolenak, Precipitation strengthening of Nb-stabilized TP347 austenitic steel by a dispersion of secondary Nb(C,N) formed upon a short-term hardening heat treatment, Materials Science and Engineering: A 647 (2015) 294-302.

[4] E.V. Pereloma, A.G. Kostryzhev, A. AlShahrani, C. Zhu, J.M. Cairney, C.R. Killmore, S.P. Ringer, Effect of austenite deformation temperature on Nb clustering and precipitation in microalloyed steel, Scripta Mater 75 (2014) 74-77.

[5] A.G. Kostryzhev, A. Al Shahrani, C. Zhu, J.M. Cairney, S.P. Ringer, C.R. Killmore, E.V. Pereloma, Effect of niobium clustering and precipitation on strength of an NbTi-microalloyed ferritic steel, Materials Science and Engineering: A 607 (2014) 226-235.

[6] M. Nöhrer, W. Mayer, S. Primig, S. Zamberger, E. Kozeschnik, H. Leitner, Influence of Deformation on the Precipitation Behavior of Nb(CN) in Austenite and Ferrite, Metallurgical and Materials Transactions A 45(10) (2014) 4210-4219.

[7] T.H. Zhou, D. Overby, P. Badgley, C. Martin-Root, X. Wang, S.L. Liang, H. Zurob, Study of processing, microstructure and mechanical properties of hot rolled ultra-high strength steel, Ironmaking & Steelmaking 46(6) (2019) 535-541.

[8] F.J. Humphreys, M. Hatherly, Recrystallization and Related Annealing Phenomena, Pergamon, Oxford, 1996.

[9] T. Gladman, The physical metallurgy of microalloyed steels, The Institute of Materials, London, 1997.

[10] A.T. Davenport, L.C. Brossard, R.E. Miner, Precipitation in microalloyed high-strength low-alloy steels, Jom-Us 27(6) (1975) 21-27.

[11] H.S. Zurob, Effects of precipitation, recovery and recrystallization on the microstructural evolution of the microalloyed austenite, McMaster University, 2003.

[12] A. Deschamps, Y. Bréchet, Influence of predeformation and agEing of an Al–Zn–Mg alloy—II. Modeling of precipitation kinetics and yield stress, Acta Mater 47(1) (1998) 293-305.

[13] B. Dutta, E.J. Palmiere, C.M. Sellars, Modelling the kinetics of strain induced precipitation in Nb microalloyed steels, Acta Mater 49(5) (2001) 785-794.

[14] H.S. Zurob, C.R. Hutchinson, Y. Bréchet, G. Purdy, Modeling recrystallization of microalloyed austenite: effect of coupling recovery, precipitation and recrystallization, Acta Mater 50(12) (2002) 3075-3092.

[15] V. Nagarajan, E.J. Palmiere, C.M. Sellars, New approach for modelling strain induced precipitation of Nb(C,N) in HSLA steels during multipass hot deformation in austenite, Mater Sci Tech 25(9) (2009) 1168-1174.

[16] V. Nagarajan, A new approach for modelling strain induced precipitation of niobium carbonitrides in austenite during multipass hot rolling, University of Sheffield, 2011.

[17] W. Charnock, J. Nutting, The Effect of Carbon and Nickel upon the Stacking-Fault Energy of Iron, Metal Science Journal 1(1) (1967) 123-127.

[18] P.J. Hurley, P.D. Hodgson, B.C. Muddle, A study of deformation substructures in austenite using a model Ni-30 wt.% Fe alloy, Scripta Mater 45(1) (2001) 25-32.

[19] T. Malis, S.C. Cheng, R.F. Egerton, EELS LOG-RATIO TECHNIQUE FOR SPECIMEN-THICKNESS MEASUREMENT IN THE TEM, Journal of Electron Microscopy Technique 8(2) (1988) 193-200.

[20] G.J. Jones, R.K. Trivedi, Lateral Growth in Solid-Solid Phase Transformations, Journal of Applied Physics 42(11) (1971) 4299-4304.

[21] D. Kuhlmann-Wilsdorf, Theory of plastic deformation: - properties of low energy dislocation structures, Materials Science and Engineering: A 113 (1989) 1-41.

[22] J.C. Huang, G.T. Gray, Microband formation in shock-loaded and quasi-statically deformed metals, Acta Metallurgica 37(12) (1989) 3335-3347.

[23] L.E. Murr, A. Ayala, C.S. Niou, Microbands and shear-related microstructural phenomena associated with impact craters in 6061-T6 aluminum, Mat Sci Eng a-Struct 216(1-2) (1996) 69-79.

[24] B. Gonzalez, L.E. Murr, O.L. Valerio, E.V. Esquivel, H. Lopez, Microbands and microtwins associated with impact craters in copper and brass targets: the role of stacking fault energy, Mater Charact 49(4) (2002) 359-366.

[25] L.E. Murr, E.V. Esquivel, Observations of common microstructural issues associated with dynamic deformation phenomena: Twins, microbands, grain size effects, shear bands, and dynamic recrystallization, J Mater Sci 39(4) (2004) 1153-1168.

[26] J.D. Yoo, K.T. Park, Microband-induced plasticity in a high Mn-Al-C light steel, Mat Sci Eng a-Struct 496(1-2) (2008) 417-424.

[27] Z.W. Wang, H.B. Bei, I. Baker, Microband induced plasticity and the temperature dependence of the mechanical properties of a carbon-doped FeNiMnAlCr high entropy alloy, Mater Charact 139 (2018) 373-381.

[28] E. Nes, W.B. Hutchinson, A.A. Ridha, On the Formation of Microbands During Plastic Straining of Metals, in: H.J. McQueen, J.P. Bailon, J.I. Dickson, J.J. Jonas, M.G. Akben (Eds.), Strength of Metals and Alloys (ICSMA 7), Pergamon1985, pp. 57-62.

[29] Thermo-Calc software package, http://www.thermocalc.com/, 2019.

[30] M. Perez, Gibbs-Thomson effects in phase transformations, Scripta Mater 52(8) (2005) 709-712.

CHAPTER 4: NbC precipitation during two-pass hot deformation of a nickel-based model alloy: experiments and modelling[6]

4.1 Introduction

During the thermomechanical controlled processing of microalloyed steel, microalloying carbonitride precipitates can be utilized to alter the softening kinetics and tune the microstructure [1-7]. For instance, abnormal grain growth will be inhibited by the Zener pinning force from precipitates when using proper temperature during heat treatments [8]. The distribution of particles in the matrix is of great importance, which determines the effectiveness of pinning to boundary migration [9] or changes the effective obstacle spacing for strengthening [10]. As already known, strain-induced precipitates nucleate on dislocations heterogeneously. Therefore, the spatial distribution of precipitates is largely relying on the configuration of dislocation structures. The structure is normally a mixture of dislocation features which consist of dislocation tangles, cell structure and microbands and so on.

In order to investigate the hot-working microstructure of steels, nickel-rich or nickel-based model alloys, of which austenite can be retained down to room temperature, are anticipated. The dislocation structure formed during hot and/or cold deformation can be preserved, which makes it possible to study the interactions between dislocations and precipitates. Nagarajan et al [11, 12] observed the microbands structure and precipitates with a Fe-30wt%Ni model alloy in a temperature range from 850°C to 1000°C. Microbands are the major feature after hot deformation, without the evidence of the formation of cell structures. Jiang et al [13] studied the nickel-based superalloy and showed similar microbands structures. However, stacking fault energy (SFE) is also important to the variation of microstructure, i.e. high SFEs favor the formation of cell structure and low

---

[6] This chapter is based on our journal publication: Shenglong Liang, Xiang Wang, Carmen Andrei and Hatem S. Zurob, NbC precipitation during two-pass hot deformation of a nickel-based model alloy: experiments and modelling, in preparation.

SFEs for twinning [14]. A Ni-30wt%Fe model with a stacking fault energy of about 60~70 mJ/m^2 is believed to be close to that of austenite of microalloyed steels [15], in the same temperature range. Our previous work [16] focused on the room-temperature (RT) deformation and subsequent annealing as well as NbC precipitation behavior of such a model alloy. Nevertheless, according to Kocks and Mecking [17], the deformed microstructure depends on temperature and strain rate due to the work-hardening and dynamic recovery effects during deformation. Thus, the microstructure after hot deformation will be preserved and investigated using transmission electron microscopy. As an important aspect for the modelling of thermomechanical processing [18], precipitation behavior during hot working should be investigated thoroughly following microstructural evolution.

As compared to our previous work [16], the major focuses of the current one will be on: (a) the microstructure after hot deformation and its evolution during annealing; (b) both precipitate spatial and size distribution and growth/coarsening during isothermal holding and (c) the effects of microstructural changes on mechanical properties, for the first and second passes. The results from room-temperature deformation and hot working will be compared and discussed as well.

4.2 Experimental

The present work was carried out using an austenitic nickel-based model alloy (Ni-30wt%Fe-0.33wt%Nb-0.03wt%C). The as-received material was machined into cylinders of 5 mm in diameter and 10 mm in height and deformation was conducted with a Bahr dilatometer DIL 805. Specimens were heated up to 900℃ for 5 mins in order to dissolve pre-existing precipitates and homogenize the microstructure, cooled down to the deformation temperature of 700℃ for 20 secs, and then deformed with a strain of 0.25 and strain rate of 0.8 s^{-1}, followed by helium quench. A sample with additional 45 mins annealing was obtained in order to study the microstructure evolution during isothermal holding. Similar treatments were conducted for the second pass (with 5 mins and 60 mins annealing after the deformation). The detailed scheme for two-pass deformation and annealing is presented in Fig. 4-1.

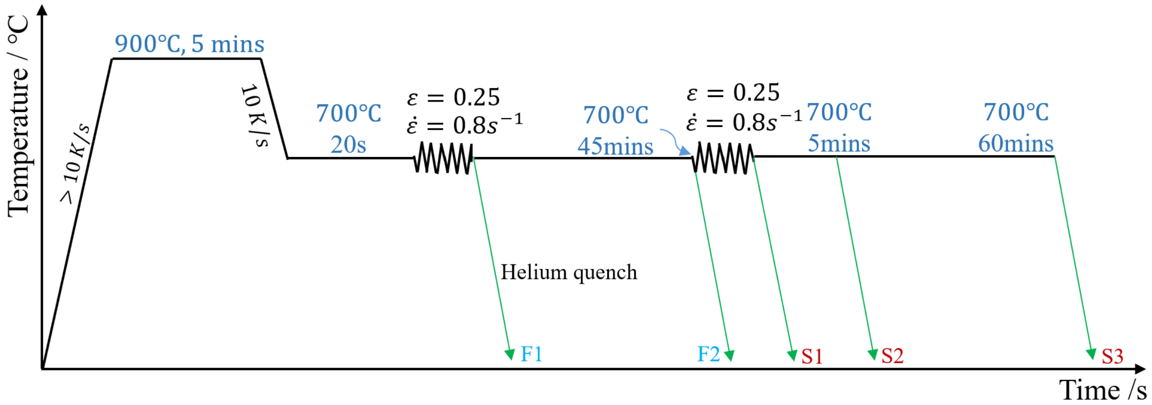

Fig. 4-1: Two-pass hot-deformation scheme at 700°C. Samples were quenched with helium at maximum speed.

The load force was recorded for each deformation pass and converted to true stress-strain flow curves. Vickers microhardness (Hv) was measured for each annealing condition with a load of 300 grams. TEM foils were prepared by sectioning the tensile samples parallel to the longitudinal direction, grinding down to below 100 μm in thickness and finally twin-jet electropolishing in a solution of 5% perchloric acid in methanol at -30°C and 35 Volts. For carbon replica, the samples were polished with 1μm diamond paste and slightly etched with a solution of 2 mL glycerol, 8 mL hydrochloric acid, 6 mL nitric acid and 4 mL glacial acetic acid, followed by a carbon layer coating under vacuum. Carbon coatings were then detached by dissolving the matrix using 8% nital solution (pure ethanol) and picked up with copper grids. TEM observations were performed with a Philips CM12 and a JEOL 2010F operated at 120 kV and 200 kV, respectively.

4.3 Results

4.3.1 Mechanical properties

Vickers microhardness of each sample condition was measured at room-temperature and presented in Fig. 4-2(a). As can be seen, the microhardness of the as-received material is about 160 Hv and it increased to 252 Hv after the first pass deformation and then dropped to 225 Hv with 45 mins annealing at 700°C. After the second pass deformation, the microhardness increased to 280 Hv and dropped to 261 Hv with 5 mins annealing at 700°C, and further decreased to 245 Hv with 60 mins annealing at 700°C. The flow stress for each pass deformation is plotted in Fig. 4-2(b). For the first pass deformation, the as-received material yielded at 105 MPa and work-hardened to 450 MPa with a strain of 0.25. However, the yielding stress was 370 MPa and increased to 490 MPa gradually.

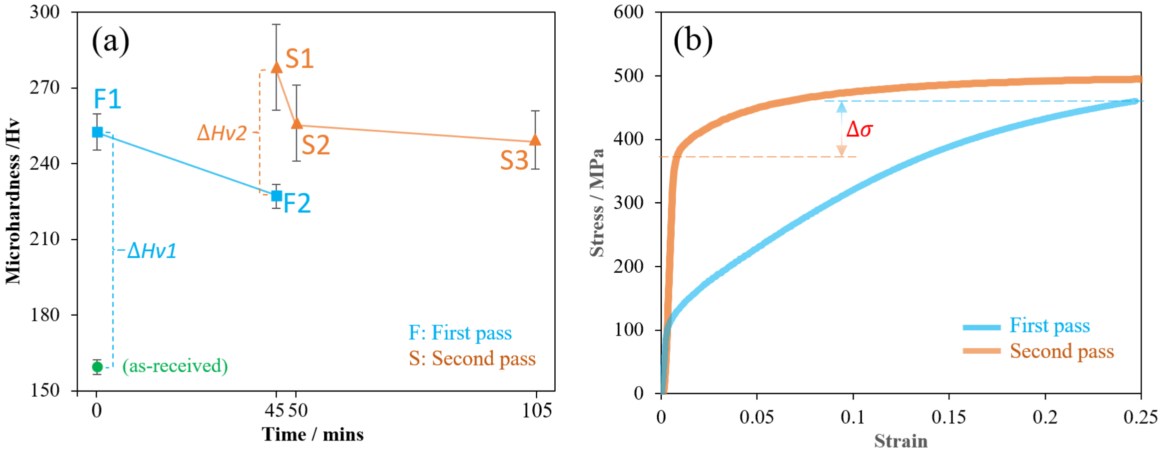

Fig. 4-2: (a) Microhardness evolution of two-pass deformation and annealing conditions as well as the as-received material, microhardness was measured at room temperature and (b) flow stress of two-pass hot deformations to a strain of 0.25.

4.3.2 Microstructure

The microstructure right after the first pass hot deformation is shown in Fig. 4-3. As it can be observed, the major feature is the development of cell-like structures in Fig. 4-3(a). These are composed of the curvy boundaries with relatively high dislocation density and regions of much less dislocations. Microbands that are roughly 0.2 ~ 0.5 μm can be seen occasionally as shown in Fig. 4-3(b). The microband boundaries are almost parallel to the {111} plane. In some areas inside the microbands or in-between, dislocation tangles or individuals can be observed such as in Fig. 4-3(c) and (d). Fine precipitates can be located on dislocations. In order to confirm the nature of precipitates, high angle annular dark field analysis in scanning TEM mode (STEM-HAADF) was performed (Fig. 4-3(e)). The niobium carbides precipitates (white particles) are sitting on dislocations (white lines).

With additional 45 mins annealing after the deformation, the general observation shows similar microstructure. However, well-defined microband structures such as in Fig. 4-3(b) were getting rare. Almost all the boundaries tended to form cell-like structure, as shown in Fig. 4-4(a). In Fig. 4-4(b), tangled or individual dislocations can still be seen uniformly almost everywhere. Further detailed investigation showed that some dislocations were pinned by precipitates; while other precipitates did not interact with any dislocations (as shown by the red arrows in Fig. 4-4(c)) which indicates the break-away and annihilation of dislocations during recovery.

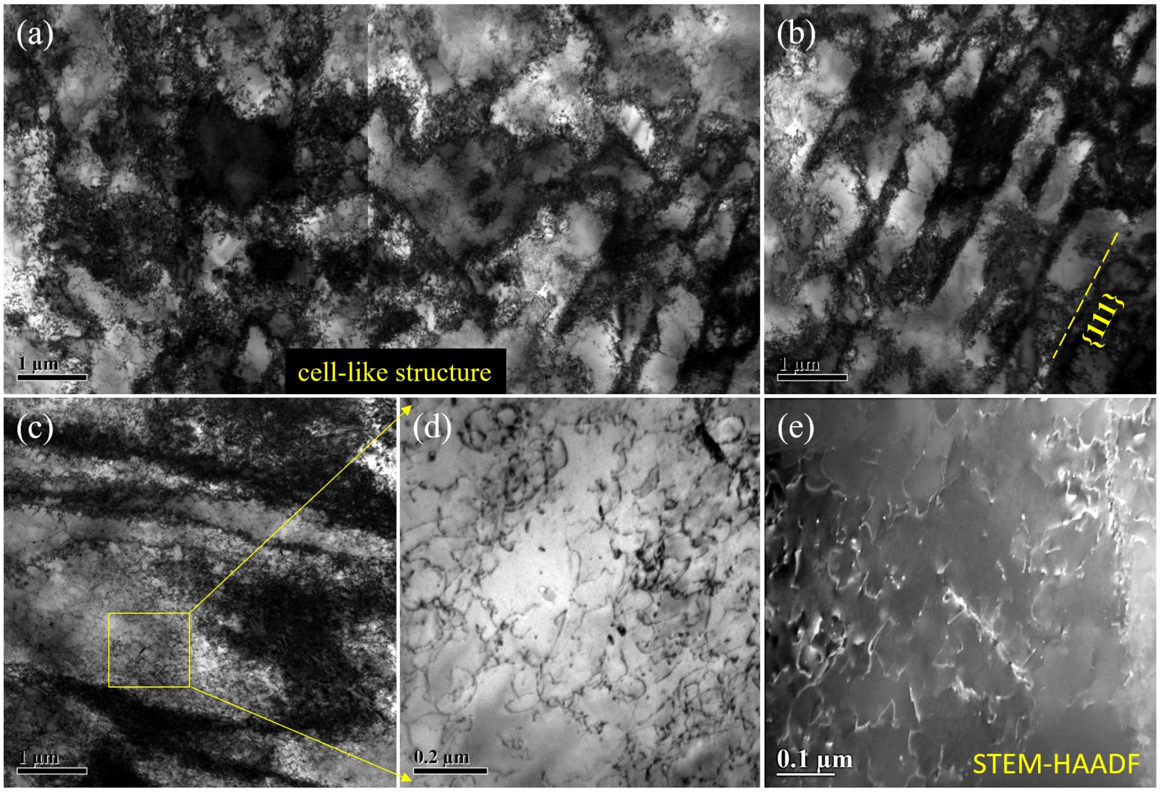

Fig. 4-3: Microstructure after the first pass deformation with a strain of 0.25 at 700°C: (a) frequently observed cell-like structure; (b) band structures along {111} plane trace; (c) diffuse band structures and dislocation tangles; (d) precipitates on dislocation tangles in square area in (c) and (e) precipitates and dislocations confirmed in STEM-HAADF mode.

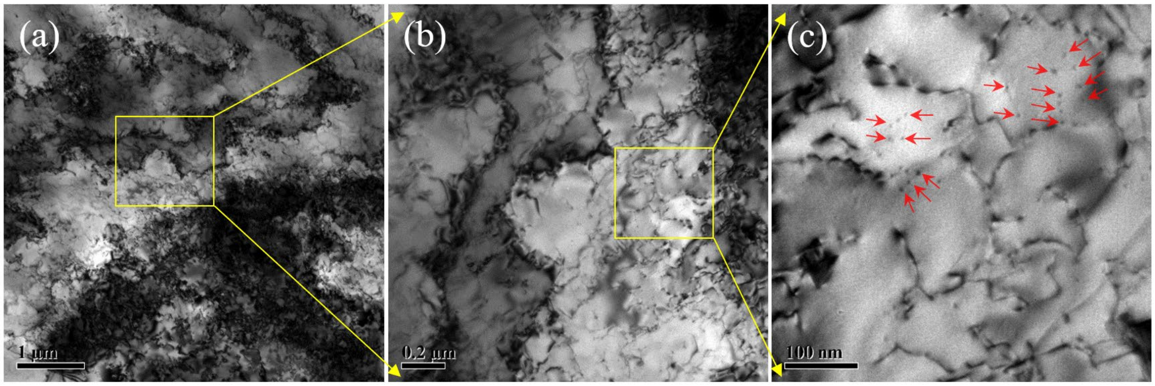

Fig. 4-4: Microstructure with 45 mins annealing at 700℃ after the first pass deformation: (a) the band structure with cell-like structure formation tendency; (b) part of the serrated microband boundaries in (b); and (c) precipitates and pinned dislocations.

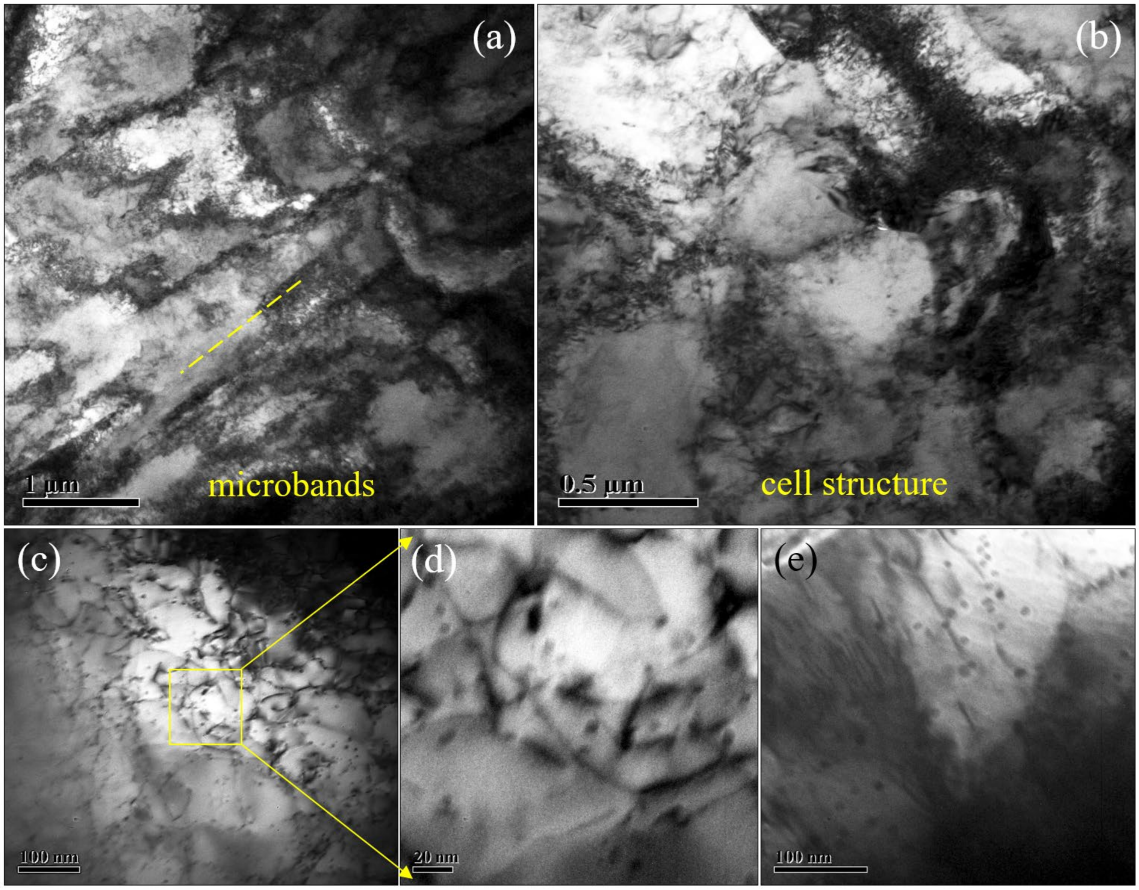

Fig. 4-5: Microstructure after the second pass deformation and annealing for 5 mins at 700℃: (a) microband structure with cell formation tendency; (b) relatively well-defined cell structure; (c) dislocations interacting with some of the precipitates; (d) a zoom-in of the square area in (c) and (e) growing precipitates with extended 60 mins annealing at 700℃.

The microstructure after the second pass deformation and annealing is quite similar to that in the first pass. As shown in Fig. 4-5, microbands with cell formation tendency were frequently observed. Pure cell structures were also observed in some areas without any trace of the microband walls. Moreover, as can be seen in Fig. 4-5(c) and (d), dislocations seem to be pinned by some of the precipitates as well. It has to be mentioned that the distribution of precipitates is locally inhomogeneous depending on the landscape of dislocations after the deformation. The precipitates grew to relatively larger sizes after 60 mins annealing at 700°C as shown in Fig. 4-5(c).

4.3.3 Precipitation evolution

Precipitates were observed on dislocations right after the first pass hot deformation, which is different from the case with room-temperature deformation followed by annealing at 700°C in our previous work [16]. The precipitate size was measured to be the diameter of the particles using carbon replica technique in conventional TEM and more than 150 particles were counted and measured as can be seen in Fig. 4-6(a). Niobium was confirmed by energy dispersive spectroscopy (EDS) obtained within TEM as shown in Fig. 4-6(b). In Fig. 4-7, the evolution of precipitate size of each condition is demonstrated. The average diameter of precipitates is 1.64 nm after the first pass deformation (F1) and then it increased to about 3.25 nm with 45 mins annealing at 700°C. The size distribution of precipitates after the second pass hot deformation (S1) is similar to that of the annealed condition in the first pass, with an average diameter of 3.07 nm. The size increased to 4.35 nm and 5.87 nm after 5 mins and 60 mins annealing at 700°C, respectively. The average number density of the precipitates for the deformed sample (F1) was also estimated, using high angle annular dark field analysis in scanning TEM mode (STEM-HAADF) (e.g. Fig. 4-3(e)), and the density was measured to be around $(0.88 \pm 0.27)\times10^{22}$ / m^3. The details can be found in Appendix VII.

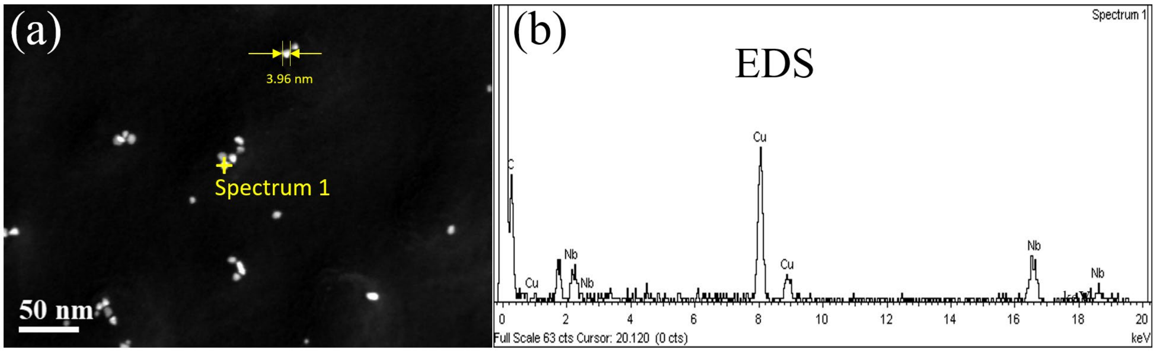

Fig. 4-6: (a) NbC precipitate size measurement by carbon replica in STEM-HAADF (e.g. for the sample S1) and (b) Nb confirmed by energy dispersive spectroscopy (EDS).

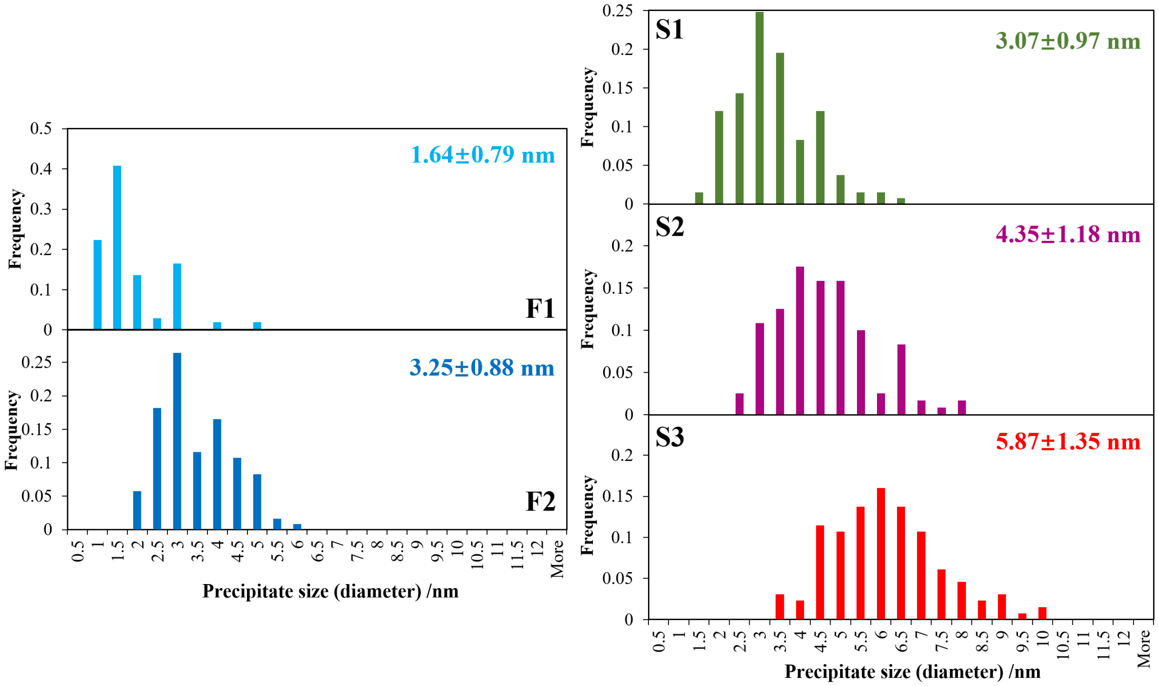

Fig. 4-7: Precipitate size (diameter) distribution evolution for the first pass (F1, F2) and second pass (S1, S2, S3). The average diameter and standard deviation of the distribution was calculated.

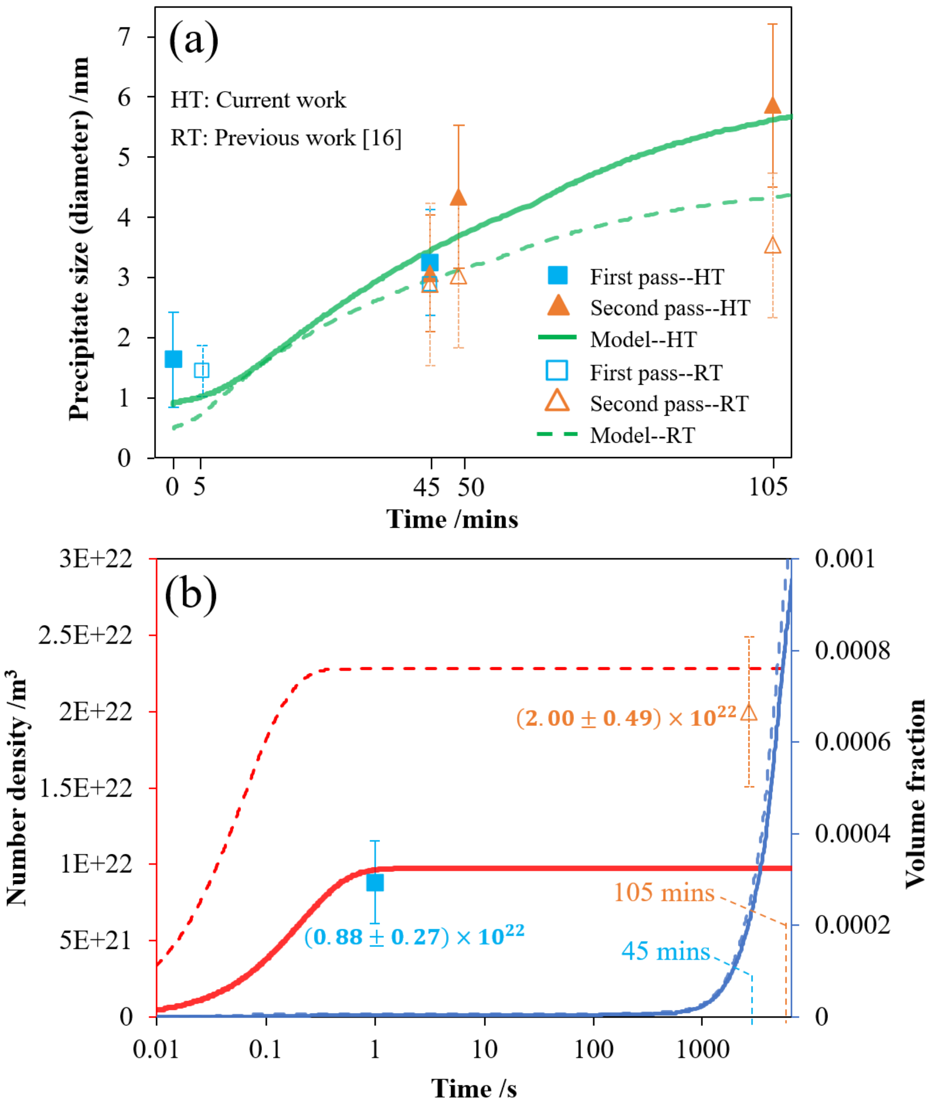

Fig. 4-8: Experimental and simulated results for the size, number density and volume fraction of precipitates: (a) precipitate size (diameter) evolution and (b) number density and volume fraction, for high-temperature deformation (HT, solid lines or solid symbols) and room-temperature deformation (RT, dash lines or hollow symbols).

4.3.4 Modelling of precipitation kinetics

Having the nucleation of precipitates on individual dislocations been confirmed by TEM, the precipitation kinetics will be modelled again using the classical model with an initial stage of nucleation and growth followed by a stage of growth and coarsening [19, 20]. The criterion proposed by Deschamps and Bréchet [19] for the transition from nucleation-growth to growth-coarsening stage was adopted. Then the model was implemented and run at 700°C. As we can see in Fig. 4-8, the precipitate size grew from about 0.95 nm to 5.65 nm after 105 mins, and the number density was predicted to be 0.93×10^{22} / m^3 which is close to the measured number of $(0.88 \pm 0.27)\times10^{22}$ / m^3. The number density profile indicates that the coarsening stage was not reached within the two-pass annealing time and the precipitates kept growing. The volume fraction of NbC precipitates were approaching 0.0010 which is about two-thirds of the equilibrium volume fraction calculated by Thermo-Calc [21]. The results for room-temperature deformation and annealing (dash lines or hollow symbols) from our previous work were also included which will be discussed in the next session.

4.4 Discussions

4.4.1 Microstructure evolution

As shown in Fig. 4-3, the hot-deformed microstructure consists of mainly cell-like structures and some ill-defined or diffuse microbands made of dense dislocation walls (DDWs) [22]. Dislocation tangles or individuals can be observed in regions with lower dislocation density. Compared to our previous work [16] with room-temperature deformation, cell-like structures are more abundant with hot deformation, which is due to the thermally-activated process of dislocation climb. DDWs tend to organize into Low energy dislocation structure (LEDS) as described by Kuhlmann and Wilsdorf [23]. The hot-deformed microstructural feature is similar to the annealed condition after room temperature deformation in our previous work. However, interestingly, well-defined and clean microband structures were observed with hot deformation of a Fe-30wt%Ni model alloy by Nagarajan et al [11, 12]. This might be explained by the low stacking fault energy (SFE) of the Fe-30wt%Ni model alloy compared to our Ni-30wt%Fe model alloy according to Charnock and Nutting [15]. In alloys with low SFEs, dislocations tend to dissociate into partial dislocations and encounter more difficulty to form cell structures during recovery

[14]. Different dislocation patterns, i.e. dislocation tangles, cell structures or microbands and so on will alter the precipitation distribution in the matrix. With additional 45 mins annealing at 700°C, the relatively straight or diffuse microband walls were getting rare. Instead, they all exhibit the tendency of forming cell structures as shown in Fig. 4-4. The microstructure after the second pass deformation and annealing is quite similar to that in the first pass as shown in Fig. 4-5. Serrated microbands and cell-like structures are also frequently observed, as well as the grown precipitates sitting in the matrix. No recrystallization was observed for both passes during the isothermal annealing. However, it must be pointed out that a relatively low temperature of 700°C was used for our previous room-temperature deformation or the hot-deformation work. The deformed microstructure at higher temperatures (e.g. 1000°C) might be different and further experiments are needed in order to elucidate the effect of temperature on hot deformation of the model alloy.

4.4.2 Strain-induced precipitation

Strain-induced precipitation is very fast with hot deformation. As shown in Fig. 4-3(d) and (e), precipitates formed even right after the first pass deformation. The deformation time is about 0.3 sec and the effective time could be around 1.0 sec considering the cooling within the bulk material by the helium quenching. The measured average size is 1.64 nm which is relatively larger than 0.95 nm predicted by the precipitation model. This might be due to the limitation of our TEM equipment for resolving fine particles below 1 nm using foil samples. Overall, the model predictions agree well with the experimental results for both the precipitate size and number density.

By comparing the size distribution of F2 and S1 as well as considering the growth of the particle size, a second class of nucleation following the second pass hot deformation did not occur. Only the first class of precipitates nucleated after the first pass deformation and kept growing during annealing, which is consistent with our previous calculation of the nucleation rate for the subsequent passes where the nucleation free energy barrier increased largely with the depletion of Nb and C solutes by precipitation. The results for room-temperature deformation and annealing in our previous work were included for comparison.

As shown in Fig. 4-8, the number density for RT is higher than that with high-temperature (HT, 700°C) deformation, leading to a faster growth rate for hot-deformation and annealing conditions, which is reasonable for such a niobium diffusion-controlled process.

4.4.3 Mechanical response

In Fig. 4-2, the microhardness change ($\Delta Hv1$) after the first pass deformation is larger that ($\Delta Hv2$) for the second pass. This is due to the partial recovery of the stored energy from the first pass deformation during 45 mins annealing at 700°C. As shown in Fig. 4-2(b), the yielding stress decreased ($\Delta\sigma$) by about 80 MPa, which is a net effect of recovery and precipitation hardening. Recovery kept reducing the dislocation density and thus lowering the yielding strength while the growth of precipitates was strengthening the material.

4.5 Conclusion

Precipitation behavior in a nickel-based model alloy during two-pass hot deformation has been investigated. The interactions between deformation, annealing and precipitation were studied using TEM and microhardness tests. The results were obtained and summarized as followed:

1. The microstructural features after hot deformation are mainly composed of cell-like structures, as well as some microbands and dislocation tangles/individuals. This is different from the as-deformed microstructure at room temperature.

2. Precipitation heterogeneously nucleates on randomly distributed dislocations and the process is instantaneous (~ 1.0 sec). The formation of precipitates was observed only after the first pass during the two-pass deformation and annealing process.

3. Recovery will always decrease the hardness and yielding strength by the annealing-out of dislocations, while precipitation could strengthen the material during the growth stage.

4. The precipitation model predictions of the size and number density of precipitates show good agreements with quantitatively measured experimental results for hot-deformation and annealing of the model alloy.

4.6 Reference

[1] L. Llanos, B. Pereda, B. López, Interaction Between Recovery, Recrystallization, and NbC Strain-Induced Precipitation in High-Mn Steels, Metallurgical and Materials Transactions A 46(11) (2015) 5248-5265.

[2] C.L. Miao, C.J. Shang, H.S. Zurob, G.D. Zhang, S.V. Subramanian, Recrystallization, Precipitation Behaviors, and Refinement of Austenite Grains in High Mn, High Nb Steel, Metall Mater Trans A 43a(2) (2012) 665-676.

[3] T.N. Baker, Microalloyed steels, Ironmaking & Steelmaking 43(4) (2016) 264-307.

[4] E.V. Pereloma, A.G. Kostryzhev, A. AlShahrani, C. Zhu, J.M. Cairney, C.R. Killmore, S.P. Ringer, Effect of austenite deformation temperature on Nb clustering and precipitation in microalloyed steel, Scripta Mater 75 (2014) 74-77.

[5] A.G. Kostryzhev, A. Al Shahrani, C. Zhu, J.M. Cairney, S.P. Ringer, C.R. Killmore, E.V. Pereloma, Effect of niobium clustering and precipitation on strength of an NbTi-microalloyed ferritic steel, Materials Science and Engineering: A 607 (2014) 226-235.

[6] N. Isasti, D. Jorge-Badiola, M.L. Taheri, P. Uranga, Microstructural and precipitation characterization in Nb-Mo microalloyed steels: Estimation of the contributions to the strength, Metals and Materials International 20(5) (2014) 807-817.

[7] A. Pandit, A. Murugaiyan, A.S. Podder, A. Haldar, D. Bhattacharjee, S. Chandra, R.K. Ray, Strain induced precipitation of complex carbonitrides in Nb–V and Ti–V microalloyed steels, Scripta Mater 53(11) (2005) 1309-1314.

[8] T.H. Zhou, H.S. Zurob, Abnormal and post-abnormal austenite grain growth kinetics in Nb-Ti microalloyed steels, Can Metall Quart 50(4) (2011) 389-395.

[9] E. Nes, N. Ryum, O. Hunderi, On the Zener drag, Acta Metallurgica 33(1) (1985) 11-22.

[10] T.H. Courtney, Mechanical behavior of materials, McGraw-Hill, New York, 1990.

[11] V. Nagarajan, A new approach for modelling strain induced precipitation of niobium carbonitrides in austenite during multipass hot rolling, University of Sheffield, 2011.

[12] V. Nagarajan, E.J. Palmiere, C.M. Sellars, New approach for modelling strain induced precipitation of Nb(C,N) in HSLA steels during multipass hot deformation in austenite, Mater Sci Tech 25(9) (2009) 1168-1174.

[13] H. Jiang, J. Dong, M. Zhang, L. Zheng, Z. Yao, Hot deformation characteristics of Alloy 617B nickel-based superalloy: A study using processing map, Journal of Alloys and Compounds 647 (2015) 338-350.

[14] F.J. Humphreys, M. Hatherly, Recrystallization and Related Annealing Phenomena, Pergamon, Oxford, 1996.

[15] W. Charnock, J. Nutting, The Effect of Carbon and Nickel upon the Stacking-Fault Energy of Iron, Metal Science Journal 1(1) (1967) 123-127.

[16] S. Liang, X. Wang, H.S. Zurob, NbC precipitation during multi-pass deformation of a nickel-based model alloy: Experiments and modelling, Materials Science and Engineering: A 772 (2020) 138748.

[17] U.F. Kocks, H. Mecking, Physics and phenomenology of strain hardening: the FCC case, Prog. Mater. Sci. 48(3) (2003) 171-273.

[18] H.S. Zurob, C.R. Hutchinson, Y. Bréchet, G. Purdy, Modeling recrystallization of microalloyed austenite: effect of coupling recovery, precipitation and recrystallization, Acta Mater 50(12) (2002) 3075-3092.

[19] A. Deschamps, Y. Bréchet, Influence of predeformation and agEing of an Al–Zn–Mg alloy—II. Modeling of precipitation kinetics and yield stress, Acta Mater 47(1) (1998) 293-305.

[20] B. Dutta, E.J. Palmiere, C.M. Sellars, Modelling the kinetics of strain induced precipitation in Nb microalloyed steels, Acta Mater 49(5) (2001) 785-794.

[21] Thermo-Calc software package, http://www.thermocalc.com/, 2019.

[22] J.C. Huang, G.T. Gray, Microband formation in shock-loaded and quasi-statically deformed metals, Acta Metallurgica 37(12) (1989) 3335-3347.

[23] D. Kuhlmann-Wilsdorf, Theory of plastic deformation: - properties of low energy dislocation structures, Materials Science and Engineering: A 113 (1989) 1-41.

CHAPTER 5: Use of in-situ laser-ultrasonics measurements to develop robust models combining deformation, recovery, recrystallization and grain growth[7]

5.1 Introduction

Grain size control during the thermomechanical controlled processing (TMCP) [1] of hot-rolled steels is of great importance for achieving high strength and toughness. During roughing, grain size is refined through the multi-pass deformation using a reversing mill [2]. Higher grain boundary surface area per unit volume (S_V) [3] is usually obtained through pancaking of the austenite grains during finishing [4]. The abundance of nucleation sites leads to the refinement of ferrite grain size during the phase transformation from austenite to ferrite.

Grain size evolution during TMCP is essentially linked to the recrystallization kinetics [5] within the interpass time. Many studies have employed the double-hit method [6-8] to measure the softening fraction as a function of holding time and gain an insight into the recrystallization kinetics of a certain deformation condition. The double-hit deformation method requires several specimens and different holding times in order to measure the softening fraction, which then needs to be related to the recrystallized fraction using various assumptions and/or approximations [6]. An alternative method of monitoring the microstructure evolution is that of stress relaxation [9], which is more efficient, in terms of the number of specimens needed. In both tests, however, information on the grain size is not directly available. Observation of the as-quenched specimens using traditional optical metallography could be used to study the grain size, provided that the prior austenite grain boundaries can be accurately revealed by chemical or thermal etching. Recent advances in

---

[7] This chapter is based on the submitted journal publication: Shenglong Liang, Daniel Levesque, Nicolas Legrand and Hatem S. Zurob, use of in-situ laser-ultrasonics measurements to develop robust models combining deformation, recovery, recrystallization and grain growth, submitted.

EBSD [10] have also made it possible to reconstruct the prior austenite grains from the as-quenched martensitic structure. These metallographic approaches, however, are often very difficult and time consuming. Furthermore, none of the metallographic methods can provide in-situ information on grain-size evolution.

The recently developed laser-ultrasonics (LUS) technique [11, 12] makes it possible to measure the evolution of grain size in-situ, with a resolution of 0.1 sec [13, 14]. This technique is based on the generation and detection of ultrasonic waves travelling through the thickness of the sample and bouncing back and forth at its two surfaces. The amplitude attenuation of the ultrasonic wave due to the scattering by the microstructure, can be correlated to the grain size of the material. Strong attenuation corresponds to large grain size and weak attenuation corresponds to small grain size. This correlation has been quantified for several materials including steels [13, 15, 16], nickel alloys [17], cobalt alloys [18], titanium alloys [19] and pure copper [20] and so on.

The availability of the LUS data provides a unique opportunity to validate microstructure evolution models. The onset of recrystallization and subsequent grain growth can be clearly discerned from the experimental data. Early models, such as the pioneering work of Sellars et al [21-23] can describe the overall recrystallization kinetics of a specific grade. However, different parameters need to be fitted when the grade or temperature regime changes (e.g. [24]), thus limiting the predictive capability of these semi-empirical models. Physically-based models [25-28] which are based on the interactions of recovery, recrystallization, grain growth and precipitation have the potential to predict trends associated with changes in chemistry and temperature. The models captured the nucleation and growth of recrystallized grains as well as subsequent (normal) grain growth kinetics. The effects of solutes such as microalloying elements (Nb, Ti) were considered through the solute drag [29, 30] and Zener pinning effects [31]. Other modelling approaches include cellular automaton [32, 33] or phase field simulations coupled with crystal plasticity theory [34]. These models offer additional benefits at the expense of the computation time. All these models require validation data which includes both information of the evolution of the flow stress and information on the evolution of the grain [35]. In the present work, we carried our simultaneous measurements of the flow stress using the stress relaxation method and the grain-size using the laser-ultrasonics method, on two C-Mn steels with different levels of Nb. The data is used to validate our earlier modelling work.

5.2 Experimental

Two C-Mn steel grades were used in this work. In order to illustrate the effect of microalloying additions on microstructure evolution, the compositions of the two steels only differed in terms of the Nb contents, as shown in Table 5-1. The first steel (C-Mn) does not contain any Nb, while the second steels (C-Mn-Nb) contained 0.05 wt% Nb. Cylindrical specimens with a diameter of 10 mm and a height of 15 mm were used. A Gleeble 3500 thermo-mechanical simulator equipped with a laser-ultrasonics system was used for the heat treatment and high temperature deformation simulation (Fig. 5-1). The ultrasonic wave was set up to travel perpendicular to the Gleeble compression axis as shown in Fig. 5-1(a). The specimens were held at 1200°C for 3 mins in order to dissolve pre-existing precipitates and homogenize the microstructure, and then cooled down to the deformation temperatures of 950°C or 1050°C. The specimens were deformed to strains of 0.15, 0.25, 0.35, at a strain rate of 1 s^{-1}. Strains in this range are sufficient to trigger static recrystallization, but not large enough to lead to dynamic recrystallization. After deformation, the displacement was kept constant and the stress relaxation was measured up to 200 secs. At the end of the stress relaxation test, the specimens were helium quenched to room temperature. The detailed deformation scheme is presented schematically in Fig. 5-1(b).

The grain size evolution was simultaneously measured using the laser-ultrasonics system, which was installed on the Gleeble. To generate the ultrasonic wave, a short (5 ns), energetic (150 mJ), green (532 nm) light pulse from a frequency-doubled Nd:YAG laser was employed. The detection is made using a long-pulse Nd:YAG laser operating at 1064 nm (infrared), with a pulse duration of 50 μs and a pulse energy of 70 mJ. A confocal Fabry–Perot interferometer was employed with a detection bandwidth of 75 MHz.

The amplitude of ultrasonic waves of longitudinal mode will decay while travelling through the bulk material due to scattering by the microstructure. The frequency-dependent attenuation $\alpha(f)$ can be measured and correlated to the grain size using the single echo attenuation method in which the variation in amplitude between the first echo and a reference echo is measured as a function of frequency *f*. The reference echo of low attenuation is taken at room temperature at the beginning and is used to remove the diffraction effect in the calculation of attenuation at high temperature. The ultrasonic frequency content used for grain size measurements is typically from 2 to 30 MHz. The basic equation used to interpret ultrasonic attenuation of longitudinal waves is:

$$\alpha(f) = a + bf^3 \qquad (5-1)$$

where, the first term, a, is related to ultrasound absorption (considered independent of frequency) and amplitude variations from one laser shot to another, and the second term is related to scattering. The a and b values are treated as fitting parameters in Eq. $(5-1)$. Also, a calibration curve was built between the scattering parameter, b, and austenite grain size measured by metallography after quench on a series of steel samples of different grades in the range of 900 to 1250°C. Such calibration curve is used to convert fitted parameter b with austenite grain size. More details about the laser-ultrasonics measurement technique is available in the literature [13, 14, 16, 17, 36, 37].

Table 5-1: Alloy chemistry for two C-Mn steels (in wt%)

Grade name	C	Mn	Si	Nb
C-Mn	0.03	1.82	0.68	0.00
C-Mn-Nb	0.03	1.82	0.68	0.05

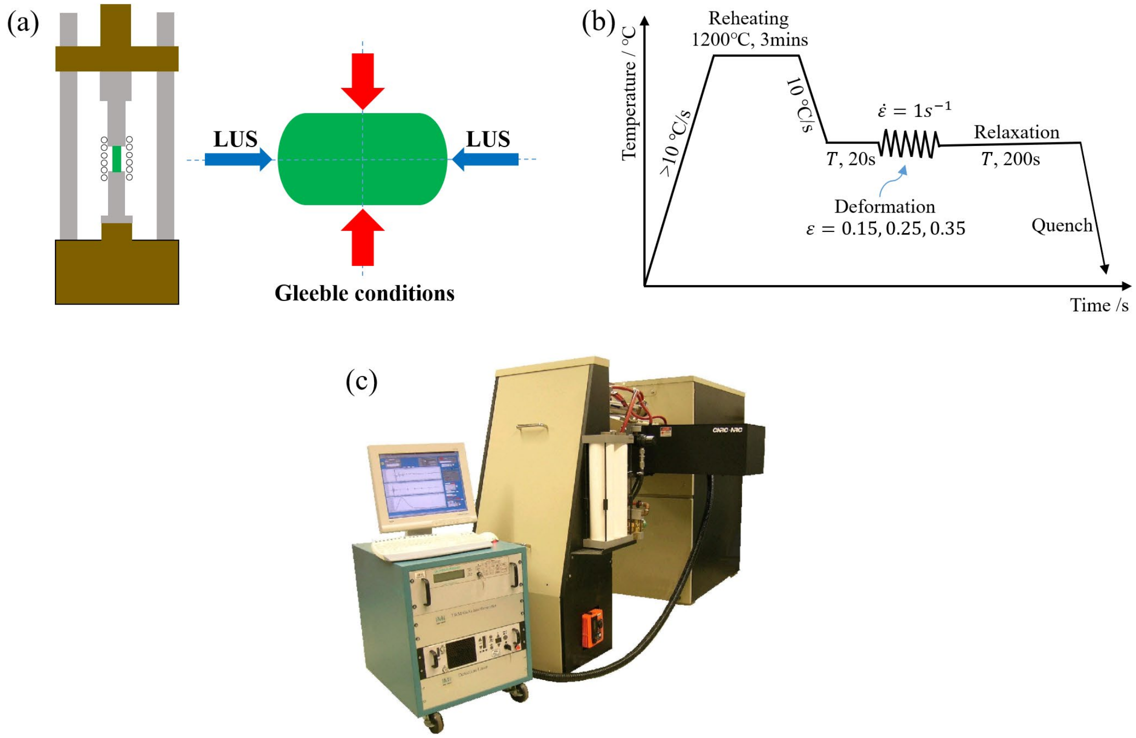

Fig. 5-1: (a) Schematic Gleeble 3500 simulator system with loading axis and laser-ultrasonics setups; (b) detailed schedule for reheating, deformation and relaxation and (c) Gleeble 3500 equipped with laser-ultrasonics system used in the present work.

5.3 Results

As presented in Fig. 5-2(a), the C-Mn steel was deformed to a strain of 0.25 at 950°C. The flow stress reached maximum 126 MPa. The displacement was then held constant and the stress relaxation was monitored as shown in Fig. 5-2(b). During the initial stages of stress relaxation the stress decreases linearly with the logarithmic of time as would be expected due to recovery [5]. The deviation from linearity indicates the onset of recrystallization [38] or precipitation [39]. In Fig. 5-2(b), the stress relaxation curve can be divided into three stages indicating recovery, recrystallization and grain growth [38]. The onset of recrystallization can be determined by the extrapolation of the first and second stages. The onset time, t_{onset}, is around 1.8 secs for the C-Mn specimen that was deformed to a strain of 0.25 at 950°C. The grain size evolution obtained from the LUS data is shown in Fig. 5-2(c). A constant initial grain size of 150 µm is initially observed. The grain size then drops, likely as a result of the formation of new nuclei and the onset of recrystallization [14]. The drop is observed at the same time which corresponds to the onset of recrystallization based on the stress relaxation data. After reaching a minimum grain size of about 105 µm, the grain size starts to gradually increase. The initial part of the increase in the averaged grain size is due to the consumption of the residual unrecrystallized portion, while curvature-driven grain growth is probably responsible for the increase in grain size at long times. The effects of strain, temperature and Nb content on the stress relaxation and grain size evolution are shown in Figs. 5-4, 5-5, 5-6 and 5-7 and discussed in the next sections.

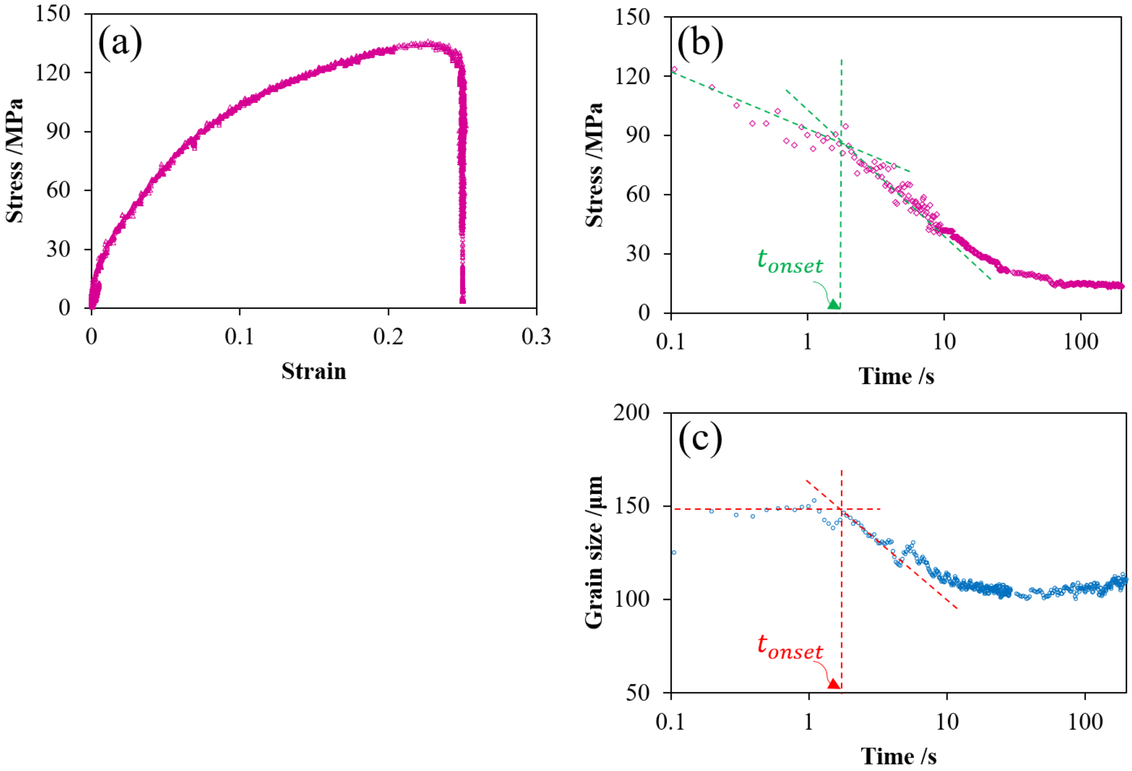

Fig. 5-2: Deformation, stress relaxation and laser ultrasonic measurement for the C-Mn steel at 950°C: (a) Stress-strain curve to a strain of 0.25; (b) stress relaxation curve and (c) grain size evolution converted from LUS data.

5.4 Modelling

5.4.1 Formulation of models

The essence of thermomechanical controlled processing is the mutual interactions between recovery, recrystallization, grain growth and precipitation after hot working. Each component constitutes our so-called TMP models under development, which includes the constitutive equation, the recovery model, the recrystallization model and the grain growth model. Some of the model parameters/constants will be tabulated in Table 5-2 at the end of the section.

5.4.1.1 Constitutive equation

Choosing a suitable constitutive equation is crucial to modelling the microstructure evolution because the stored energy can be deduced from the flow stress. From Yoshie's formulation [40], the flow stress depends on the strain, strain rate, austenite grain size, temperature and Nb concentration. Medina et al [41-43] proposed another formulation that capture the flow stress dependence on major alloying element additions through an apparent activation energy term. In what follows, the constitutive equation was adopted for modelling flow stress behavior in hot working as followed:

$$\sigma = B[1 - \exp(-C\varepsilon)]^m \qquad (5-2)$$

where, B, C and m are fitting parameters as functions of major alloying elements such as C, Mn, Si, Mo, Nb, V and Ti as demonstrated by Medina et al [41-43].

5.4.1.2 Recovery model

The annihilation and rearrangement of dislocations will contribute to the decay of the stress during the stress-relaxation test. As in the previous work [38], the stress relaxation as a result of recovery was described using the model by Verdier et al [44]:

$$\frac{d\sigma_i}{dt} = -\frac{64}{9{M_T}^3{\alpha_T}^2}\frac{\sigma_i^2}{E}\upsilon_D \exp\left(\frac{-U_0}{k_b T}\right)\sinh\left(\frac{\sigma_i V}{k_b T}\right) \qquad (5-3)$$

where, σ_i is the internal stress due to dislocations, M_T is the Taylor factor, α_T is a constant of the order of 0.15, E is the Young's modulus, υ_D is the Debye frequency, k_b is the Boltzmann's constant, U_0 and V are the activation energy and activation volume, respect-tively. The activation volume is based on an earlier study [38], in which a semi-empirical expression was developed considering the effects of dislocation density, solute content and temperature:

$$V = b^3/[0.45b\sqrt{\rho} + 0.042(C_{Nb})^{0.3333} + 0.0035(C_{Mn})^{0.5} + 0.0075(C_{Al})^{0.3333} + 0.0058(C_{Si})^{0.3333} + (4700.00 - 2.5T) \times 10^{-5}] \qquad (5-4)$$

where, b is the Burgers vector, ρ is the dislocation density, C_i is the alloying composition of Nb, Mn, Al and Si in wt%, and T is the temperature in Kelvin.

5.4.1.3 Recrystallization model

Several approaches could be used to describe recrystallization kinetics [21, 26, 32, 45]. In the present discussion we used the model of Rehman et al [45] because it can predict the recrystallization incubation time, as well as, the nucleation rate and growth rate. Nucleation was assumed to take place at grain boundaries (Fig. 5-3(a)) by the mechanism of strain induced boundary migration (SIBM) [5]. It was assumed that subgrains/cells within the deformed microstructure bulge into the neighbouring grains once the size of the subgrain is large enough for the driving force, *G(t)*, to overcome the curvature term [46]:

$$r(t)_c = \frac{2\gamma_b}{G(t)} \qquad (5-5)$$

where, γ_b is the grain boundary energy and r is the subgrain size. The incubation time and subsequent nucleation rate are determined by the competition between the decay of *G(t)* as a result of recovery, which leads to an increase in $r(t)_c$ and the increase of the subgrain size as a result of subgrain growth. The time evolution of the average subgrain radius $r(t)$ has been described by [45] as:

$$< r(t) > = < r_0 > + \int_0^t \frac{2}{l} D_{bulk} sinh\left(K_{ad}\sigma b^2 \frac{l}{k_b T}\right) dt \qquad (5-6)$$

where, r_0 is the average subgrain size after deformation which inversely depends on stress, l is the activation length, D_{bulk} is the bulk diffusion coefficient, K_{ad} is a fitting parameter in the model, σ is the applied stress and b is the Burgers vector. The recrystallizing grains grow at a rate of:

$$v = M(t)G(t) \qquad (5-7)$$

where, $G(t)$ is the instantaneous driving force for grain boundary migration, and $M(t)$ is the instantaneous grain boundary mobility. The mobility is calculated using Cahn's model [25, 30]:

$$\frac{1}{M} = \frac{1}{M_i} + \sum_j \alpha_j C_j \qquad (5-8)$$

where,

$$\alpha_j = \frac{\delta N_0 (k_b T)^2}{E_b D_{cb}} \left(\sinh\left(\frac{E_b}{k_b T}\right) - \frac{E_b}{k_b T}\right) \qquad (5-9)$$

and M is the high angle grain boundary mobility, M_i is the intrinsic mobility of the solute-free material, C_j is the concentration of impurity j in the matrix, δ is the width of the grain boundary, N_0 is the number of atoms per unit volume, E_b is the solute-boundary interaction energy and D_{cb} is the average value of the diffusion coefficient in the vicinity of the grain boundary.

During the course of recrystallization, new strain-free grains grow into the interior of the prior deformed grain from grain boundaries. In Fig. 5-3(b), one grain profile in partial recrystallization is presented schematically. The average grain size GS_{ave} of the partially recrystallized material is a volume average of the recrystallized grains and unrecrystallized portion, and it can be calculated as (see derivations in Appendix VIII):

$$GS_{ave} = X \cdot GS_{rex} + (1 - X)^{\frac{4}{3}} \cdot D_0 \qquad (5-10)$$

where, X is the recrystallization fraction, GS_{rex} is the grain size of the recrystallizing grains and D_0 is the original grain size before deformation. A simple rule of mixture is then used to calculate the flow stress, σ, during recrystallization:

$$\sigma = X \cdot \sigma_{rex} + (1 - X) \cdot \sigma_{rec} \qquad (5-11)$$

where, σ_{rex} and σ_{rec} are the flow stresses of the recrystallized and unrecrystallized material, respectively. In this way, the grain size and flow stress can be related to the recrystallized fraction. For simplicity, it was assumed curvature-driven grain-growth can begin once recrystallization is complete (i.e. when X is equal to unity).

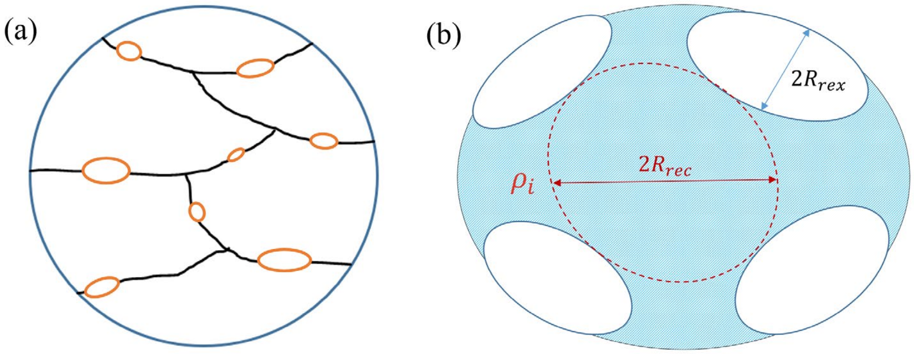

Fig. 5-3: Schematic diagrams showing (a) the number of nuclei for recrystallization forming at grain boundaries and (b) one of the scenarios regarding grain profile in partial recrystallization of the deformed grain. R_{rex} and R_{rec} are the radius for the recrystallized grains and unrecrystallized region, respectively. ρ_i is the instantaneous dislocation density in the unrecrystallized region which can be predicted by the recovery model.

5.4.1.4 Grain growth model

Most statistical grain growth theories fall into the category of mean field theories within which the average of the growth behavior is utilized to represent the whole assembly. Two commonly used models are the drift model by Hillert [47] and the diffusion model by Louat [48]. During the grain growth, the larger grains will grow, and small grains will shrink. As a result, the grain size of the whole assembly increases with time. In order to quantify the kinetics, Hillert [47] developed a statistical theory of grain growth based on the Ostwald ripening treatment by Lifshitz and Slyozov [49]. This treatment leads to the widely used formulation:

$$\overline{D}^2 - \overline{D}_0^2 = \omega M \gamma_b t \qquad (5-12)$$

where, $\overline{D}$ is the average diameter of the grains, $\overline{D}_0$ is the original average grain size and ω is a coefficient in the model. The differential format of the grain growth equation with Zener pining effect [31] considered can be written as:

$$\frac{dD}{dt} = 2M\left(\frac{\omega}{4}\frac{\gamma_b}{D} - \frac{3f\gamma_b}{2r}\right) \quad (5-13)$$

where, f and r are the volume fraction and average radius of precipitates, respectively.

Table 5-2: TMP model parameters

Symbol	Physical Meaning	Value
k_b	Boltzmann's constant	$1.38 \times 10^{-23}\ m^2 \cdot kg \cdot s^{-2} \cdot K^{-1}$
U_0	Activation energy	285,000 J/mole [50]
M_T	Taylor factor	3.1
α_T	Alpha factor	0.15 [26]
υ_D	Debye frequency	2×10^{12} s^{-1} [26]
μ	Shear modulus	$81 \times 10^9[0.91 - (T(K) - 300)/1810]$ Pa [51]
b	Burgers vector	0.25 nm
K_{ad}	Fitting parameter for subgrain growth	7.29
γ_b	Grain boundary energy	1.3115-0.0005T [26]
D_{bulk}	Bulk diffusion coefficient	0.00007exp(-285000/(RT)) [45]
ω	Coefficient for grain growth	1.58
V	Activation volume	
l	Activation length	
σ	Applied stress	
σ_i	Internal stress	
ρ	Dislocation density	
$r(t)$	Subgrain size	
C_j	Alloying content in wt%	
D	Grain size in diameter	

5.4.2 Modelling results

The above microstructure evolution models were used to describe stress relaxation and grain-size data measurements. Fig. 5-4 is a comparison of the model results and the experimental data for the C-Mn steel deformed to a strain of 0.25 and held isothermally at 950°C and 1050°C. Overall, good agreements are observed between the model and experimental results. After 1.8 secs of isothermal holding at 950°C and 0.8 sec at 1050°C, the stress relaxation data starts to deviate from the logarithmic behaviour expected when recovery is the dominant softening mechanism [5]. As pointed out earlier, the deviation is attributed to the onset of recrystallization. The model accurately captures the onset of recrystallization as demonstrated by the good agreement between the model and experimental stress relaxation data. The secondary axes on Fig. 5-4(c) and (f) show the predicted evolution of recrystallized fraction at 950°C and 1050°C. Recrystallization completed in about 97.0 secs at 950°C and 179.0 secs at 1050°C, respectively. Similar results are observed for a deformation strain of 0.35, as shown in Fig. 5-5. At 950°C, recrystallization started at 0.8 sec and completed at 30.0 secs. However, the onset and completion time of recrystallization at 1050°C are 0.11 sec and 18.2 secs, respectively. The secondary axes on Figs. 5-5(c) ~ (f) also show the predicted evolution of recrystallized fraction at 950°C and 1050°C, respectively. The experimental trends in terms of constitutive behavior, stress relaxation, the onset and completion of recrystallization and the recrystallized grain size are quantitatively captured by the model as shown by the blue curves in Figs. 5-4 and 5-5.

In Fig. 5-6, the grain size evolution of the C-Mn steel is plotted as a function of deformation strain (0.15, 0.25, 0.35) and temperature (950°C, 1050°C). The simulated grain size and the predicted number density of nuclei of recrystallization by the model have also been presented. For the low strain of 0.15, the grain size dropped after about 8.5 sec at 950°C and reached a ~40% partial recrystallization as shown by the secondary axis. However, at 1050°C, grain size increased parabolically at the beginning, followed by a gradual slow-down behavior. No recrystallization occurred at the condition. This is consistent with the nuclei density prediction by the model. For intermediate (0.25) and high (0.35) strain, the onset of recrystallization occurred at earlier time and the average grain size was reduced with increasing strain. In comparison, increasing the temperature reduced the time for the onset of recrystallization, but resulted in an increase in the average grain size. Effects of strain and temperature on recrystallization will be discussed further in the next section.

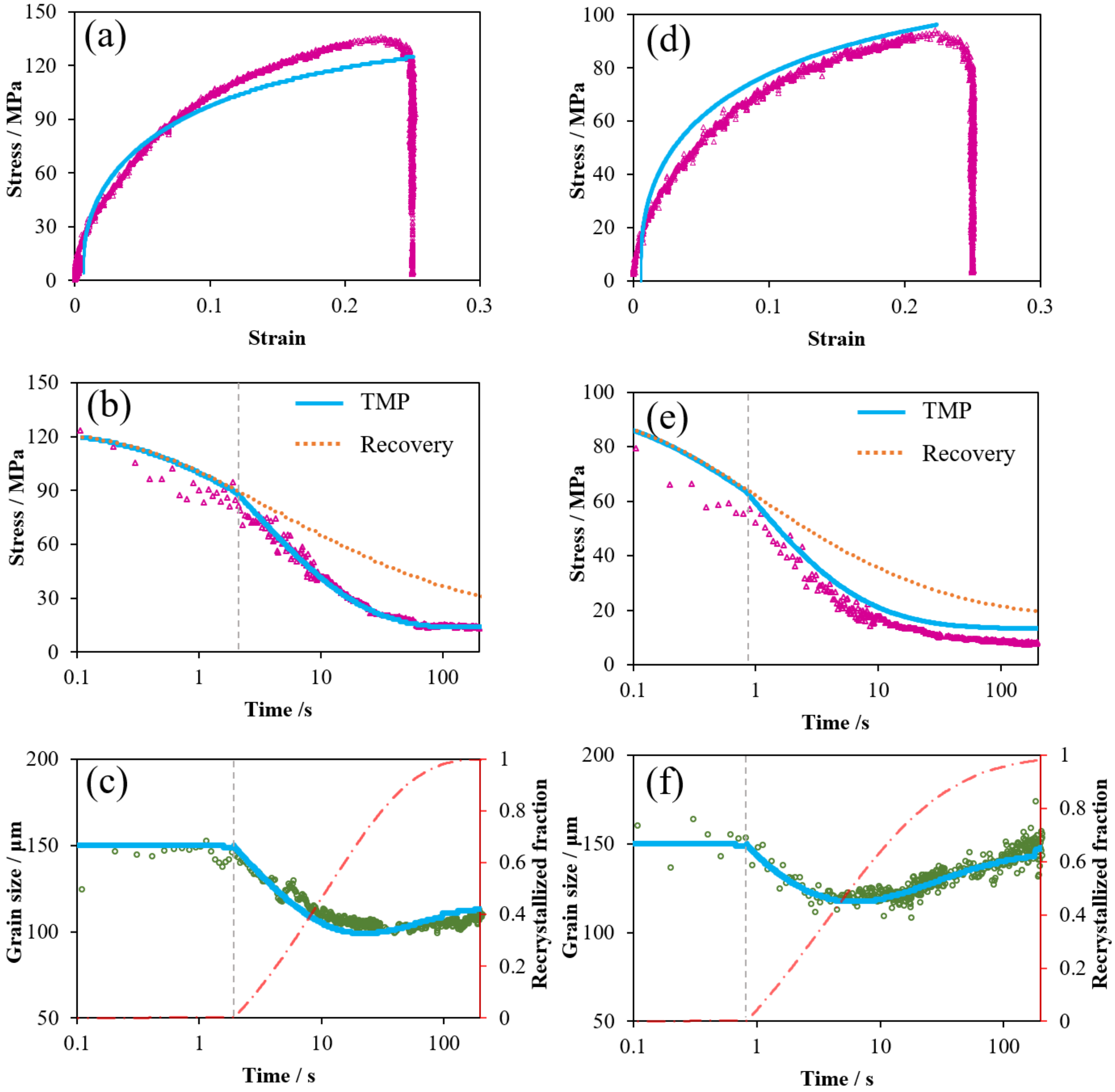

Fig. 5-4: Comparisons between stress relaxation and laser-ultrasonics measurements and TMP models for the C-Mn steel with a strain of 0.25 at 950°C: (a) stress-strain curve; (b) stress relaxation data and (c) grain size evolution, and at 1050°C (d) stress-strain curve; (e) stress relaxation data and (f) grain size evolution. TMP predictions are presented as blue curves, along with the recovery model plotted in (b) and (e). Bottom figures are showing grain size evolution as well as recrystallization fraction. The onsets of recrystallization are marked with vertical dotted grey lines.

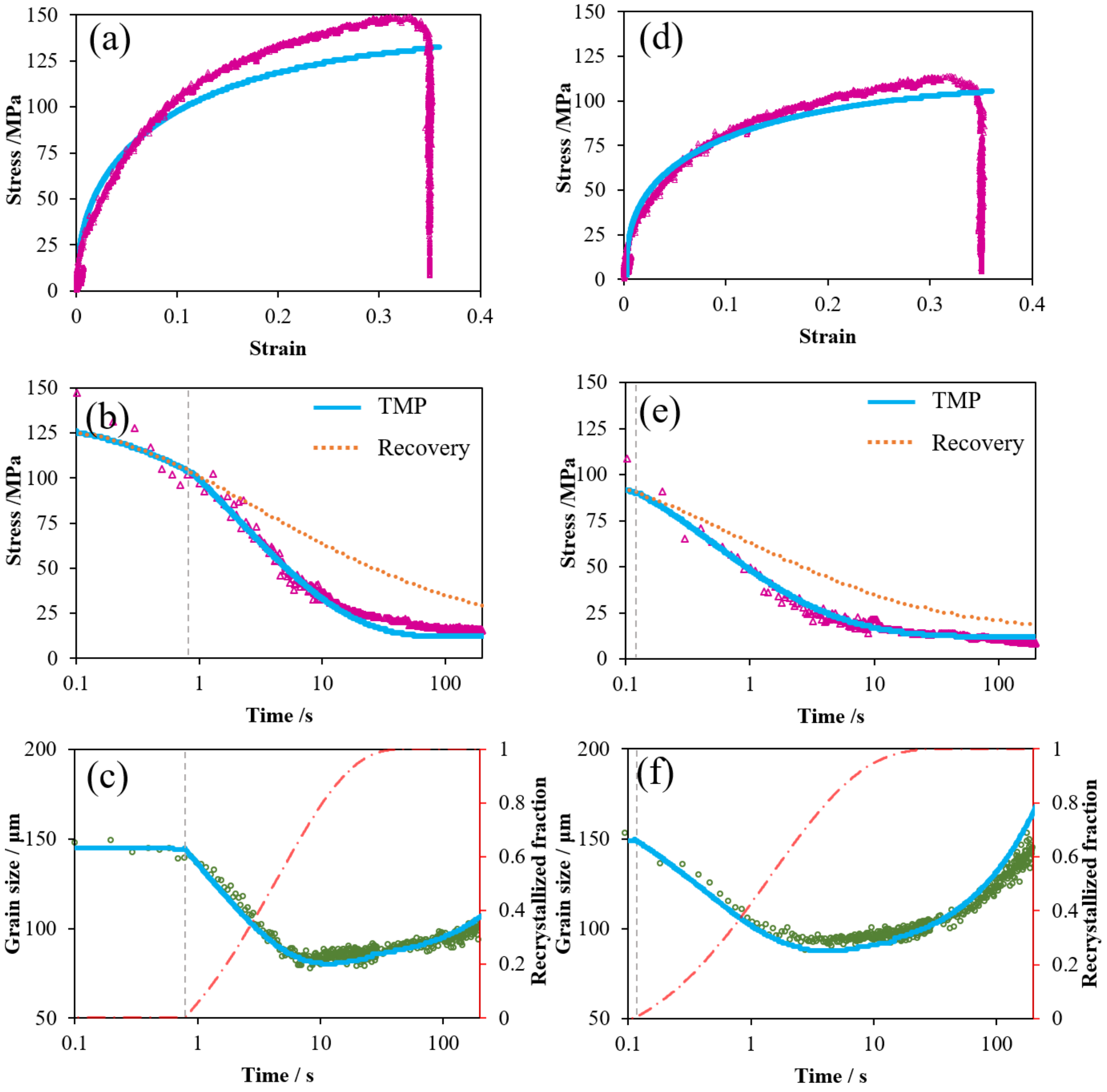

Fig. 5-5: Comparisons between stress relaxation and laser-ultrasonics measurements and TMP models for the C-Mn steel with a strain of 0.35 at 950°C: (a) stress-strain curve; (b) stress relaxation data and (c) grain size evolution, and at 1050°C (d) stress-strain curve; (e) stress relaxation data and (f) grain size evolution. TMP predictions are presented as blue curves, along with the recovery model plotted in (b) and (e). Bottom figures are showing grain size evolution as well as recrystallization fraction. The onsets of recrystallization are marked with vertical dotted grey lines.

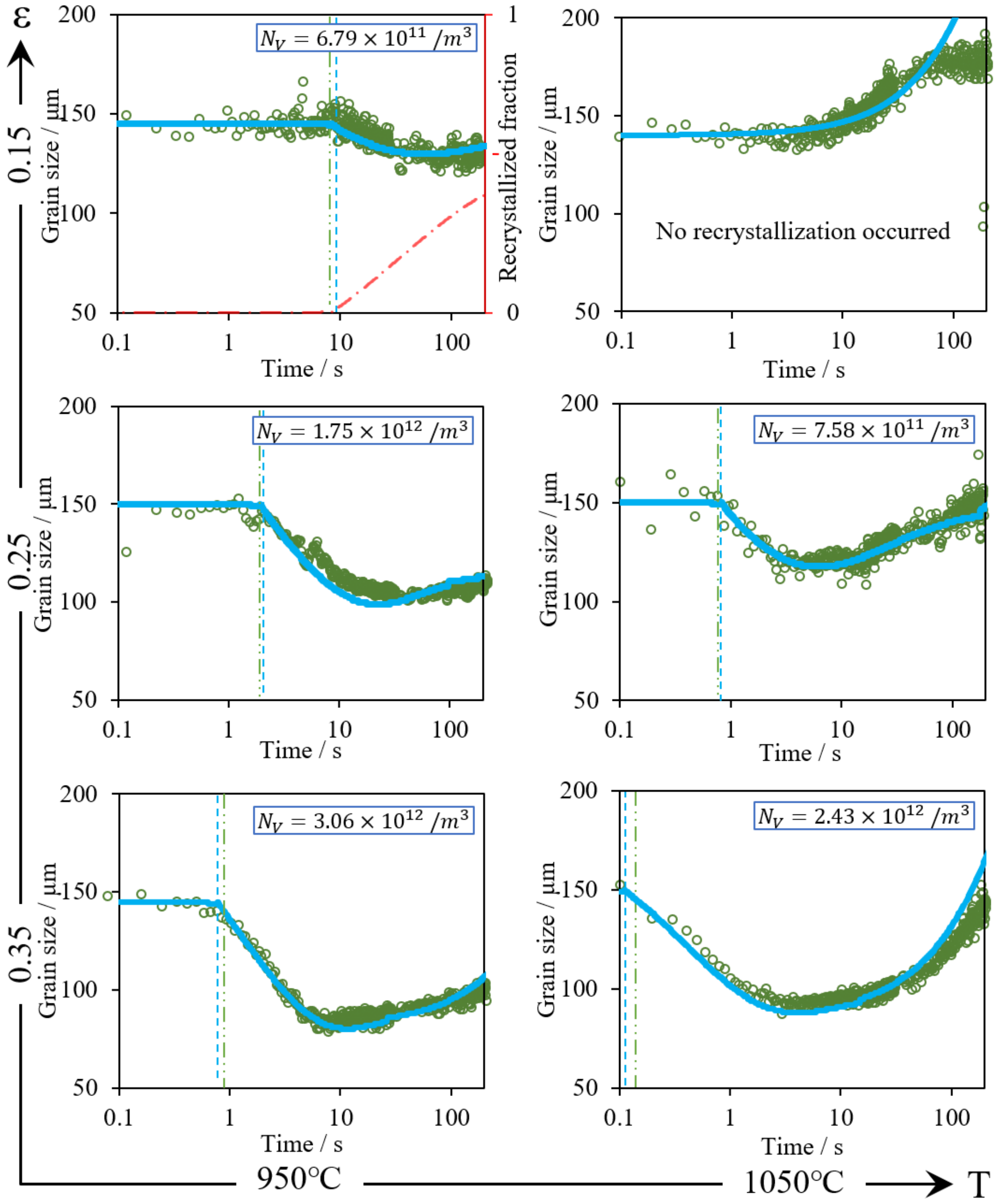

Fig. 5-6: Grain size evolution of the C-Mn steel by LUS as a function of deformation strain (0.15~0.35) and temperature (950°C and 1050°C). The onsets of recrystallization predicted by the model and determined from the LUS data were marked with two different vertical dotted lines, respectively.

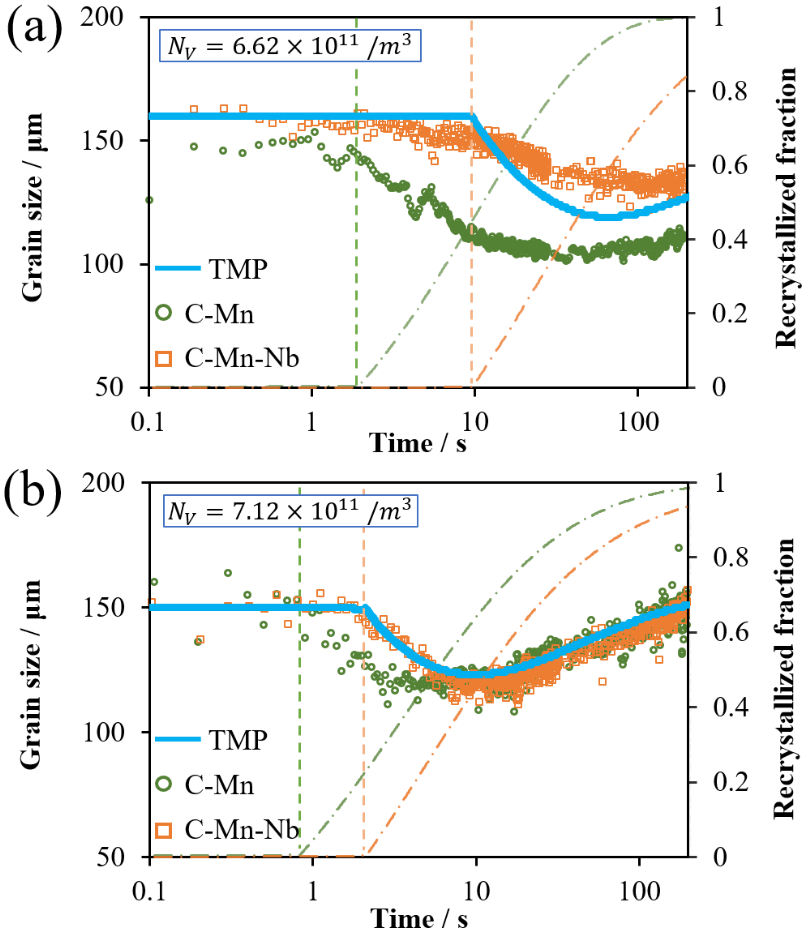

Fig. 5-7: Grain size evolution and the TMP model prediction for C-Mn-Nb steel at a strain of 0.25 at: (a) 950°C and (b) 1050°C. Grain size evolution for C-Mn steel was also included for comparison. The onsets of recrystallization for each alloy condition were marked with vertical dotted lines, respectively.

The effect of Nb on grain size evolution was also investigated with the C-Mn-Nb steel at 950°C and 1050°C for a strain of 0.25, as shown in Fig. 5-7. The experimental data shows a delay in the onsets of recrystallization due to the addition Nb. The delay is more prominent at lower temperature. These results are summarized in Table 5-3. The grain growth data shows that the recrystallized C-Mn-Nb steel has a larger grain size compared to that of the C-Mn steel at 950°C. The two steels have a comparable grain size at 1050°C. The model captures these experimental trends. Moreover, the recrystallized fractions by the model indicate only partial recrystallization occurred for both temperatures.

Table 5-3: Onsets of recrystallization for C-Mn and C-Mn-Nb steels as a function of strain, temperature and microalloying of niobium (Experiment / TMP model, in seconds)

	950°C	**1050°C**
C-Mn_0.15	$8.1^{-0.4}_{+1.2}$ / 8.5	∞ / ∞
C-Mn_0.25	$1.8^{-0.1}_{+0.3}$ / 1.9	$0.8^{-0.0}_{+0.1}$ / 0.8
C-Mn_0.35	$0.8^{-0.0}_{+0.1}$ / 0.8	$0.1^{-0.0}_{+0.0}$ / 0.1
C-Mn-Nb_0.25	$9.0^{-0.5}_{+1.5}$ / 9.6	$2.0^{-0.1}_{+0.3}$ / 1.8

Note: The lower and upper bounds of onsets are represented by " - " and " + " signs.

5.5 Discussion

5.5.1 Correlation between LUS measurement and stress relaxation

The stress relaxation curve can be divided into three segments: recovery, recrystallization and grain growth. The rate of stress decay (or the stored energy dissipating rate) is different for each stage. During recovery, dislocations annihilate and rearrangement lead to gradual, logarithmic, decay of the flow stress [5]. However, following the onset of recrystallization, the stored energy is dissipated more quickly due to the replacement of the deformed, high dislocation density grains, with the new, low dislocation density, recrystallized grains. This is marked by a rapid drop of the stress as shown in Fig. 5-2(b). The grain size evolution deduced from the laser-ultrasonics measurements in Fig. 5-2(c) shows that the grain size is constant at the beginning and then start to decrease due to the onset of recrystallization. The transition time from recovery to recrystallization is identical to that identified in the stress relaxation test. This correlation can also be observed in Figs. 5-4 and 5-5. During the final stage of grain-growth, only minor changes are observed in the stress-relaxation curve. The laser-ultrasonics measurements, however, clearly show the continued evolution of the grain size during this stage.

5.5.2 Nucleation and growth of recrystallization

The nucleation of recrystallization requires the development of low energy regions that are separated from high energy regions by a grain boundary. The development of these low energy regions/nuclei is facilitated by the recovery of the deformed structure. For low deformation strains ($0.1 < \varepsilon < 0.4$), strain induced boundary migration is the dominant nucleation mechanism for recrystallization [5, 28, 52]. Recovery would increase the critical subgrain size (Eq. $(5-5)$) needed for grain boundary bulging making recrystallization more difficult. Subgrain growth, however, can locally allow some subgrains to reach the critical size leading to nucleation at these sites. The onset of recrystallization for C-Mn and C-Mn-Nb as a function of strain, temperature and microalloying of niobium has been tabulated in Table 5-3. Increasing the applied strain, increasing the temperature and lowering the Nb content would all reduce the time for the onset of recrystallization. These trends are nicely captured by the model as shown in Table 5-3. The predicted number of nuclei per unit volume has been added in Figs. 5-6 and 5-7. With increasing strain at the same temperature or with decreasing temperature at the same strain, more recrystallization nuclei were predicted. As can be seen, the grain size will be reduced with higher number density of nuclei formed during recovery.

5.5.3 Effect of deformation strain and temperature

It is evident that with increasing strain or lower temperature, more nuclei for recrystallization were nucleated and the onset of recrystallization was shortened, leading to reduced grain size, from Table 5-3 and Figs. 5-6 and 5-7. Theoretically, higher deformation strain introduces more stored energy (high dislocation density) into the material, leading to a higher driving force for the migration of low angle grain boundaries as per Eq. $(5-6)$. This favors the nucleation of many new strain-free grains, which results in a higher number density of nuclei and a smaller recrystallized grain size. Temperature has two competing effects. On the one hand, it increases the mobility of subgrain boundaries, which shortens the transition from recovery to recrystallization as shown in Table 5-3; on the other hand, it facilitates the dissipation of stored energy due to recovery, thus reducing the number density of nuclei and leading to a larger grain size as shown in Fig. 5-6. For the low strain (0.15) and high temperature (1050°C) deformation of the C-Mn steel, there is no noticeable nucleation event and the grain size evolution is dominated by curvature driven grain growth, thus explaining the parabolic behaviour in Fig. 5-6.

5.5.4 Effect of microalloying niobium

The presence of Nb in steel modifies both the recovery and recrystallization kinetics. The interaction of Nb with dislocations and grain boundaries depends on whether Nb is present in solution or as carbonitrides $Nb(C_xN_{1-x})$. For the C-Mn-Nb steel considered here, no precipitation was predicted using a classical strain-induced precipitation model [53, 54]. Therefore, all of the Nb is present in solution. From our previous work [38, 45], niobium can slow down the cell/subgrain evolution by decreasing the distance between pinning centres. Nb is also expected to reduce the global recovery kinetics by decreasing the activation volume for the recovery process. The net effect, however, is a delay in the onset of recrystallization. Solute Nb would also interact with high angle grain boundaries. This can slow down the growth of recrystallizing grains and reduce the rate of grain growth. This effect is captured using Cahn's solute drag model [25, 30], where the binding energy of Nb to the austenite grain boundaries was assumed to be 20 kJ/mol. This effect is responsible for the longer recrystallization completion times in the C-Mn-Nb steel as shown in Fig. 5-7, compared to the C-Mn steel at the same temperature. Analysis of the model suggests that fewer nuclei were formed in the C-Mn-Nb steel at 950℃, which led to the larger grain size compared to the C-Mn steel. However, the two steels had a comparable recrystallized grain size at 1050℃. The alloying effect of Nb was reflected by the difference of the recrystallized fraction curves. For the present alloys, Nb is present in solid solution at both temperatures and the results are consistent with the general predictions of solute drag theory.

5.6 Conclusion

A physics-based model that captures the processes of recovery, recrystallization and grain growth have been validated against in-situ measurements of stress and the grain size evolution.

(1) A good agreement was obtained between the time for the onset of recrystallization as estimated from both the stress relaxation test and the in-situ laser-ultrasonics measurements.

(2) Solute Nb was observed to delay both the onset and completion of recrystallization. The retarding effect of Nb on recrystallization was more prominent at lower temperature.

(3) The proposed model can capture the onset and completion of recrystallization, as well as the grain growth kinetics as a function of strain, temperature and Nb content for the range of conditions considered here.

5.7 Reference

[1] I. Tamura, H. Sekine, T. Tanaka, C. Ouchi, Thermomechanical Processing of High-Strength Low-Alloy Steels, Elsevier1988.

[2] Q.Y. Sha, Z.Q. Sun, L.F. Li, Refinement of coarse grained austenite in Nb-V-Ti microalloyed steel during roughing rolling, Ironmaking & Steelmaking 42(1) (2015) 74-80.

[3] A. Yoshie, M. Fujioka, Y. Watanabe, K. Nishioka, H. Morikawa, Modelling of Microstructural Evolution and Mechanical Properties of Steel Plates Produced by Thermo-Mechanical Control Process, Isij Int 32(3) (1992) 395-404.

[4] S. Vervynckt, K. Verbeken, B. Lopez, J.J. Jonas, Modern HSLA steels and role of non-recrystallisation temperature, International Materials Reviews 57(4) (2012) 187-207.

[5] F.J. Humphreys, M. Hatherly, Recrystallization and Related Annealing Phenomena, Pergamon, Oxford, 1996.

[6] A.I. Fernandez, B. Lopez, J.M. Rodriguez-Ibabe, Relationship between the austenite recrystallized fraction and the softening measured from the interrupted torsion test technique, Scripta Mater 40(5) (1999) 543-549.

[7] J.S. Perttula, L.P. Karjalainen, Recrystallisation rates in austenite measured by double compression and stress relaxation methods, Mater Sci Tech 14(7) (1998) 626-630.

[8] O. Kwon, A.J. Deardo, On the recovery and recrystallization which attend static softening in hot-deformed copper and aluminum, Acta Metallurgica Et Materialia 38(1) (1990) 41-54.

[9] S. Vervynckt, K. Verbeken, P. Thibaux, Y. Houbaert, Characterization of the Austenite Recrystallization by Comparing Double Deformation and Stress Relaxation Tests, Steel Res Int 81(3) (2010) 234-244.

[10] G. Miyamoto, N. Iwata, N. Takayama, T. Furuhara, Mapping the parent austenite orientation reconstructed from the orientation of martensite by EBSD and its application to ausformed martensite, Acta Mater 58(19) (2010) 6393-6403.

[11] C. Scruby, L. Drain, Laser Ultrasonics: Techniques and Applications, Adam Hilger, Bristol, 1990.

[12] J.-P. Monchalin, Laser-ultrasonics: from the laboratory to industry, Review of Progress in Quantitative Nondestructive Evaluation 23A, in: D.O. Thompson, D.E. Chimenti (Eds.) AIP Conf. Proc., New York, 2004, pp. 3-31.

[13] M. Maalekian, R. Radis, M. Militzer, A. Moreau, W.J. Poole, In situ measurement and modelling of austenite grain growth in a Ti/Nb microalloyed steel, Acta Mater 60(3) (2012) 1015-1026.

[14] S. Sarkar, A. Moreau, M. Militzer, W.J. Poole, Evolution of austenite recrystallization and grain growth using laser ultrasonics, Metall Mater Trans A 39A(4) (2008) 897-907.

[15] S.E. Krüger, G. Lamouche, J.-P. Monchalin, R. Kolarik, G. Jeskey, M. Choquet, On-line Monitoring of Wall Thickness and Austenite Grain Size on a Seamless Tubing Production Line at the Timken Company, AISTech - Iron and Steel Tech. Conf. Proc. (2005) 25-31.

[16] G. Jeskey, J. Monchalin, R. Li, E. Damm, G. Lamouche, S. Krüger, M. Choquet, Thickness and Grain Size Sensor for On-line Seamless Steel Tubing Process Control, Mater Sci Tech (2004).

[17] T. Garcin, J.H. Schmitt, M. Militzer, In-situ laser ultrasonic grain size measurement in superalloy INCONEL 718, Journal of Alloys and Compounds 670 (2016) 329-336.

[18] M. Keyvani, T. Garcin, D. Fabregue, M. Militzer, K. Yamanaka, A. Chiba, Continuous Measurements of Recrystallization and Grain Growth in Cobalt Super Alloys, Metall Mater Trans A 48A(5) (2017) 2363-2374.

[19] F. Dong, X.C. Wang, Q. Yang, H.Q. Liu, D. Xu, Y.Z. Sun, Y.J. Zhang, R.J. Xue, S. Krishnaswamy, In-situ measurement of Ti-6Al-4V grain size distribution using laser-ultrasonic technique, Scripta Mater 154 (2018) 40-44.

[20] M. Keyvani, Laser ultrasonic investigations of recrystallization and grain growth in cubic metals, The University of British Columbia, 2018.

[21] C.M. Sellars, Modeling microstructural development during hot-rolling, Mater Sci Tech 6(11) (1990) 1072-1081.

[22] C.M. Sellars, Computer modeling of hot-working processes, Mater Sci Tech 1(4) (1985) 325-332.

[23] C.M. Sellars, J.A. Whiteman, Recrystallization and grain growth in hot rolling, Metal Science 13(3-4) (1979).

[24] P.D. Hodgson, Microstructure modelling for property prediction and control, Journal of Materials Processing Technology 60(1-4) (1996) 27-33.

[25] H.S. Zurob, Y. Bréchet, G. Purdy, A model for the competition of precipitation and recrystallization in deformed austenite, Acta Mater 49(20) (2001) 4183-4190.

[26] H.S. Zurob, C.R. Hutchinson, Y. Bréchet, G. Purdy, Modeling recrystallization of microalloyed austenite: effect of coupling recovery, precipitation and recrystallization, Acta Mater 50(12) (2002) 3075-3092.

[27] H.S. Zurob, Effects of precipitation, recovery and recrystallization on the microstructural evolution of the microalloyed austenite, McMaster University, 2003.

[28] H.S. Zurob, Y. Bréchet, J. Dunlop, Quantitative criterion for recrystallization nucleation in single-phase alloys: Prediction of critical strains and incubation times, Acta Mater 54(15) (2006) 3983-3990.

[29] M. Hillert, B. Sundman, A treatment of the solute drag on moving grain boundaries and phase interfaces in binary alloys, Acta Metallurgica 24(8) (1976) 731-743.

[30] J.W. Cahn, The impurity-drag effect in grain boundary motion, Acta Metallurgica 10(9) (1962) 789-798.

[31] E. Nes, N. Ryum, O. Hunderi, On the Zener drag, Acta Metallurgica 33(1) (1985) 11-22.

[32] D.S. Svyetlichnyy, Modelling of the microstructure: From classical cellular automata approach to the frontal one, Computational Materials Science 50(1) (2010) 92-97.

[33] M. Kuehbach, G. Gottstein, L.A. Barrales-Mora, A statistical ensemble cellular automaton microstructure model for primary recrystallization, Acta Mater 107 (2016) 366-376.

[34] T. Takaki, Y. Tomita, Static recrystallization simulations starting from predicted deformation microstructure by coupling multi-phase-field method and finite element method based on crystal plasticity, Int. J. Mech. Sci. 52(2) (2010) 320-328.

[35] N. Legrand, N. Souto, E. Poliak, D. Levesque, S.E. Krüger, Combination of metallurgical models and laser ultrasonic techniques for microstructure monitoring in hot rolling, 3rd International Symposium on Ultrasound for Metals, Stockholm, 2017.

[36] M. Militzer, T. Garcin, W.J. Poole, In-situ measurements of grain growth and recrystallization by laser ultrasonics, Mater Sci Forum 753 (2013) 25-30.

[37] D. Levesque, S.E. Krüger, G. Lamouche, R. Kolarik, II, G. Jeskey, M. Choquet, J.P. Monchalin, Thickness and grain size monitoring in seamless tube-making process using laser ultrasonics, NDT & E International 39(8) (2006) 622-626.

[38] S. Liang, F. Fazeli, H.S. Zurob, Effects of solutes and temperature on high-temperature deformation and subsequent recovery in hot-rolled low alloy steels, Materials Science and Engineering: A (2019) 138324.

[39] W.J. Liu, J.J. Jonas, A stress-relaxation method for following carbonitride precipitation in austenite at hot-working temperatures, Metallurgical Transactions a-Physical Metallurgy and Materials Science 19(6) (1988) 1403-1413.

[40] A. Yoshie, T. Fujita, M. Fujioka, K. Okamoto, H. Morikawa, Formulation of flow stress of Nb added steels by considering work-hardening and dynamic recovery, Isij Int 36(4) (1996) 467-473.

[41] S.F. Medina, C.A. Hernandez, General expression of the Zener-Hollomon parameter as a function of the chemical composition of low alloy and microalloyed steels, Acta Mater 44(1) (1996) 137-148.

[42] S.F. Medina, C.A. Hernandez, The influence of chemical composition on peak strain of deformed austenite in low alloy and microalloyed steels, Acta Mater 44(1) (1996) 149-154.

[43] C.A. Hernandez, S.F. Medina, J. Ruiz, Modelling austenite flow curves in low alloy and microalloyed steels, Acta Mater 44(1) (1996) 155-163.

[44] M. Verdier, Y. Bréchet, P. Guyot, Recovery of AlMg alloys: Flow stress and strain-hardening properties, Acta Mater 47(1) (1998) 127-134.

[45] M.K. Rehman, H.S. Zurob, A Novel Approach to Model Static Recrystallization of Austenite During Hot Rolling of Nb Microalloyed Steel. Part I: Precipitate-Free Case, Metall Mater Trans A 44a(4) (2013) 1862-1871.

[46] J.E. Bailey, P.B. Hirsch, The recrystallization process in some polycrystalline metals, Proceedings of the Royal Society of London. Series A. Mathematical and Physical Sciences 267(1328) (1962) 11.

[47] M. Hillert, On the theory of normal and abnormal grain growth, Acta Metallurgica 13(3) (1965) 227-238.

[48] N.P. Louat, On the theory of normal grain growth, Acta Metallurgica 22(6) (1974) 721-724.

[49] I.M. Lifshitz, V.V. Slyozov, The kinetics of precipitation from supersaturated solid solutions, Journal of Physics and Chemistry of Solids 19(1) (1961) 35-50.

[50] J. Fridberg, L.E. Torndahl, M. Hillert, Diffusion in iron, Jernkont. Ann. 153 (1969) 263.

[51] H.J. Frost, M.F. Ashby, Deformation-mechanism maps : the plasticity and creep of metals and ceramics, Pergamon Press, Oxford, 1982.

[52] S.P. Bellier, R.D. Doherty, Structure of deformed aluminum and its recrystallization-Investigations with transmission kossel diffraction, Acta Metallurgica 25(5) (1977) 521-538.

[53] A. Deschamps, Y. Bréchet, Influence of predeformation and agEing of an Al–Zn–Mg alloy—II. Modeling of precipitation kinetics and yield stress, Acta Mater 47(1) (1998) 293-305.

[54] S. Liang, X. Wang, H.S. Zurob, NbC precipitation during multi-pass deformation of a nickel-based model alloy: Experiments and modelling, Materials Science and Engineering: A 772 (2020) 138748.

CONCLUDING REMARKS

The aim of the current project was to develop robust models combining deformation, precipitation, recovery, recrystallization and normal grain growth, which can predict the microstructural evolution and mill load force during thermomechanical processing of microalloyed steels. However, the mutual interactions between precipitation, recovery, recrystallization and grain growth are complicated undoubtedly. To accomplish this objective, each component has been investigated individually such as the strain-induced precipitation behavior during multi-pass deformation and annealing of a Nickel-based model alloy, the alloy effects of major alloying elements on recovery, and the grain size evolution during recrystallization and grain growth stages. In-situ stress relaxation tests after straining and in-situ laser-ultrasonics measurements of grain size evolution were largely relied on for such investigations, as well as conventional transmission electron microscopic studies for microstructural features and precipitation behavior. The following conclusions can be drawn here:

- The alloying effects of Mn, Si and Al on the high temperature flow stress, recovery and the onset of recrystallization have been investigated. A pragmatic formulation for activation volume term was developed that accounts for the effect of solute content and temperature on the recovery kinetics. Lower temperatures or richer solute concentration will retard recovery and mitigate dynamic recovery during hot deformation. The effects on recovery process of studied elements suggest that Al has the most prominent effect (per mass%) and the weakest effect for Mn. The time for the onset of recrystallization varies depending on the degree of recovery. Generally, higher temperatures or less alloying elements lead to shorter transition time from recovery to recrystallization. This suggests that during nucleation, recovery helps recrystallization, in contrast to growth conditions where recovery and recrystallization compete for the stored energy.
- Precipitation behavior in a nickel-based alloy during multi-pass deformation has been investigated. The interactions between deformation, annealing and precipita-

tion were studied using TEM and microhardness tests. The microstructural features after room-temperature deformation are microbands, cell structures and dislocation tangles. Precipitation nucleates on randomly distributed dislocations or microbands, heterogeneously. The typical "*cube-on-cube*" orientation relationship between precipitates and the matrix has been observed. The formation of precipitates was observed only after the first pass during the multi-pass deformation and annealing process. Deformation will facilitate the nucleation and growth of precipitates. Recovery will always decrease the hardness by the annealing-out of dislocations. However, precipitation could strengthen the material if precipitation coarsening is not dominant. In contrast to the room-temperature case, the as-deformed microstructure for hot deformation followed by annealing consists of serrated microbands with the tendency to form cell-like structures, and pure cell structures, which is due to the dynamic recovery during hot deformation. The precipitates were observed right after the hot deformation and grew to larger sizes with further annealing. The nucleation of a new class of precipitates did not occur for the second-pass deformation. For both cases, the size distribution and number density of precipitates were measured quantitatively, which show good agreements with the model predictions.

- ❖ A physically-based model that captures the processes of recovery, recrystallization and grain growth has been validated against in-situ measurements of stress and the grain size evolution. A very good agreement was obtained between the time for the onset of recrystallization as estimated from the stress relaxation tests and the in-situ laser-ultrasonics measurements. Solute Nb was observed to delay both the onset and completion of recrystallization. The retarding effect of Nb on recrystallization was more prominent at lower temperature. The proposed model can capture both the onset and completion of recrystallization, as well as the grain growth kinetics as a function of strain, temperature and niobium content for the range of conditions considered.

The aim to develop such models has been accomplished successfully during the course of Ph.D studies. The current TMP models have been advanced and compared to the previous ones (Appendix IX), and potential model applications such as for ultra-high strength steel development (Appendix X) are valuable. There are, however, remaining challenges to be taken up for thermomechanical processing of microalloyed steels, such as how to consider the strain accumulation during partial recrystallization for both multi-pass roughing and finishing regimes or how to deal with the bi-modal distribution of grain size microstructure scenario, etc. And the advancement of modern TEM equipment renders the possibility to quantify the precipitate very precisely during thermomechanical processing, which can improve the precipitation model predictions. These topics will be visited with interests and passions, in the near future.

—Stay Hungry. Stay Foolish—

APPENDIXES

Appendix I: Rolling Mill Configuration

Typical mill layouts consist of reheating furnace, rough rolling, finish rolling, controlled cooling and coiling stages. A coil box might exist between the rough rolling and finish rolling. A schematic diagram is shown in Fig. A1.

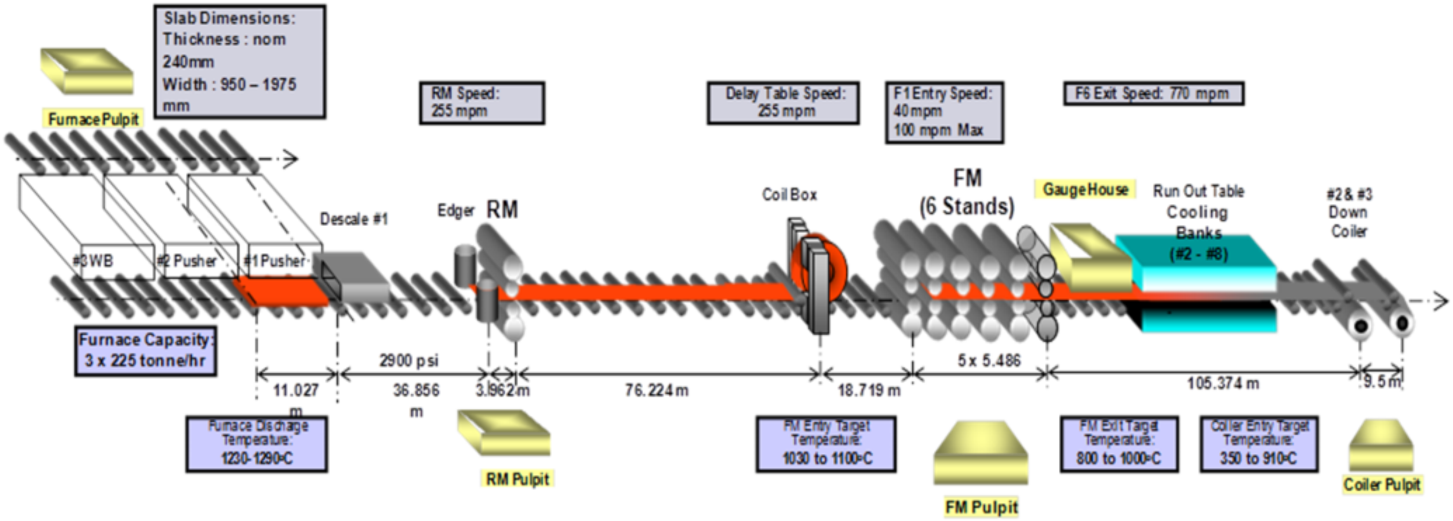

(courtesy of Dr. Tom Zhou at Stelco)

Fig. A1: Schematic rolling mill configuration of reheating, roughing, finishing, cooling and coiling.

Appendix II: Driving Force for Carbonitride in Austenite

Let us assume the formation of δ moles of precipitate MC_xN_{1-x} from one mole of austenite. The reaction can be expressed as:

$$\gamma_0 \rightarrow \delta MC_xN_{1-x} + (1-2\delta)\gamma \qquad \text{A.}(1)$$

where, δ moles of precipitate MC_xN_{1-x} contains 2δ moles of atoms due to the two sublattice crystal structure, γ_0 is the supersaturated matrix and γ is the austenite after precipitation. x in MC_xN_{1-x} means the site fraction of carbon in the interstitial sublattice.

The Gibbs energy change with the reaction is given by:

$$\Delta G = \delta G_{MC_xN_{1-x}} + (1-2\delta)G_\gamma - G_{\gamma_0} \qquad \text{A.}(2)$$

where, $G_{MC_xN_{1-x}}$, G_γ and G_{γ_0} are the molar Gibbs energy of carbonitride, γ and γ_0. The Gibbs energy change with the reaction can also be represented with the concentrations and chemical potential of each component.

$$\Delta G = \delta\left[\mu_M^{MC_xN_{1-x}} + x\mu_C^{MC_xN_{1-x}} + (1-x)\mu_N^{MC_xN_{1-x}}\right] + (1-2\delta)\left[C_M^\gamma\mu_M^\gamma + C_C^\gamma\mu_C^\gamma + C_N^\gamma\mu_N^\gamma\right] - \left[C_M^{\gamma_0}\mu_M^{\gamma_0} + C_C^{\gamma_0}\mu_C^{\gamma_0} + C_N^{\gamma_0}\mu_N^{\gamma_0}\right] \qquad \text{A.}(3)$$

where, $\mu_i^{MC_xN_{1-x}}$, μ_i^γ and $\mu_i^{\gamma_0}$ are the chemical potentials of the elements i. C_i^γ and $C_i^{\gamma_0}$ are the molar fraction concentration of elements i in remaining and supersaturated austenite, respectively.

Considering the mass balance, we will have

$$C_M^{\gamma_0} = \delta + (1-2\delta)C_M^\gamma \qquad \text{A.}(4)$$

$$C_C^{\gamma_0} = x\delta + (1-2\delta)C_C^\gamma \qquad \text{A.}(5)$$

$$C_N^{\gamma_0} = (1-x)\delta + (1-2\delta)C_N^\gamma \qquad \text{A.}(6)$$

Substituting mass balance equations and noting that the precipitation amount is small, then we can write the Gibbs energy change as:

$$\Delta G = \delta\left[\mu_M^{MC_xN_{1-x}} - \mu_M^{\gamma_0}\right] + x\delta\left[\mu_C^{MC_xN_{1-x}} - \mu_C^{\gamma_0}\right] + (1-x)\delta\left[\mu_N^{MC_xN_{1-x}} - \mu_N^{\gamma_0}\right] \qquad \text{A.}(7)$$

Considering the equilibrium between the austenite and precipitate, i.e. the chemical potential is the same for the elements i in both phases:

$$\mu_i^{MC_xN_{1-x}} = \mu_i^{\gamma_e} \qquad \text{A.}(8)$$

Then,

$$\Delta G = \delta[(\mu_M^{\gamma_e} - \mu_M^{\gamma_0}) + x(\mu_C^{\gamma_e} - \mu_C^{\gamma_0}) + (1-x)(\mu_N^{\gamma_e} - \mu_N^{\gamma_0})] \qquad \text{A.}(9)$$

If the ideal solution is assumed, then we can write down the chemical potential with respect to the concentration of elements i as:

$$\mu_i = \mu_i^* + RTlnC_i \qquad \text{A.}(10)$$

Then the Gibbs energy change now can be expressed as:

$$\Delta G = -RT\delta\left[ln\frac{C_M^{\gamma_0}}{C_M^{\gamma_e}} + xln\frac{C_C^{\gamma_0}}{C_C^{\gamma_e}} + (1-x)ln\frac{C_N^{\gamma_0}}{C_N^{\gamma_e}}\right] = -RT\delta\left[ln\frac{C_M^{\gamma_0}{C_C^{\gamma_0}}^x{C_N^{\gamma_0}}^{1-x}}{C_M^{\gamma_e}{C_C^{\gamma_e}}^x{C_N^{\gamma_e}}^{1-x}}\right] \qquad \text{A.}(11)$$

As we also know, for the carbonitride, the relationship between the equilibrium concentrations of elements M, C, N and their solubility products of carbides and nitrides:

$$xK_{MC} = C_M^{\gamma_e}C_C^{\gamma_e} \qquad \text{A.}(12)$$

$$(1-x)K_{MN} = C_M^{\gamma_e}C_N^{\gamma_e} \qquad \text{A.}(13)$$

Substituting equilibrium concentrations with the solubility products, we will have

$$\Delta G = -RT\delta\left[ln\frac{C_M^{\gamma_0}{C_C^{\gamma_0}}^x{C_N^{\gamma_0}}^{1-x}}{[xK_{MC}]^x[(1-x)K_{MN}]^{1-x}}\right] \qquad \text{A.}(14)$$

Usually, the Gibbs energy change per unit volume of the precipitate, i.e. the driving force for the precipitation per unit volume can then be written as:

$$\Delta G = -\frac{RT}{V_P}\left[ln\frac{C_M^{\gamma_0}{C_C^{\gamma_0}}^x{C_N^{\gamma_0}}^{1-x}}{[xK_{MC}]^x[(1-x)K_{MN}]^{1-x}}\right] \qquad \text{A.}(15)$$

where, V_P is the molar volume of the carbonitride MC_xN_{1-x}

Appendix III: Logarithmic Decay in Recovery

In the recovery session, it is assumed that relaxation rate of the internal stress occurs by thermally activated mechanisms as:

$$\frac{d\sigma_i}{dt} = -Kexp\left(\frac{-U(\sigma_i)}{kT}\right) \qquad \text{A. (16)}$$

$$U(\sigma_i) = U_0 - V\sigma_i \qquad \text{A. (17)}$$

where, K is a constant, $U(\sigma_i)$ is the activation energy which decreases linearly with the stress, V is the activation volume of the elementary recovery events. Then,

$$\frac{d\sigma_i}{dt} = -Kexp\left(-\frac{U_0 - V\sigma_i}{kT}\right) \quad = -Kexp\left(-\frac{U_0}{kT}\right) \cdot exp\left(\frac{V\sigma_i}{kT}\right) \qquad \text{A. (18)}$$

$$d\sigma_i \cdot exp\left(-\frac{V\sigma_i}{kT}\right) = -Kexp\left(-\frac{U_0}{kT}\right)\ dt \qquad \text{A. (19)}$$

$$-\frac{kT}{V} d\left(exp\left(-\frac{V\sigma_i}{kT}\right)\right) = -Kexp\left(-\frac{U_0}{kT}\right)\ dt \qquad \text{A. (20)}$$

$$exp\left(-\frac{V\sigma_i}{kT}\right) = \frac{KV}{kT} exp\left(-\frac{U_0}{kT}\right)\ t + C \qquad \text{A. (21)}$$

At the beginning of the stress relaxation (i.e. $t = 0$), we have:

$$C = exp\left(-\frac{V\sigma_0}{kT}\right). \qquad \text{A. (22)}$$

Therefore,

$$exp\left(-\frac{V\sigma_i}{kT}\right) = \frac{KV}{kT} exp\left(-\frac{U_0}{kT}\right)\ t + exp\left(-\frac{V\sigma_0}{kT}\right) \qquad \text{A. (23)}$$

By rearranging the equation, then we can have:

$$\frac{V(\sigma_0 - \sigma_i)}{kT} = \ln\left(1 + \frac{KV}{kT} exp\left(\frac{V\sigma_0 - U_0}{kT}\right)\ t\right) \qquad \text{A. (24)}$$

Finally, the internal stress during the recovery softening can be written as:

$$\sigma_i = \sigma_0 - \frac{kT}{V} \ln\left(1 + \frac{t}{t_0}\right) \qquad \text{A. (25)}$$

$$t_0 = \frac{kT}{KV} \exp\left(\frac{U_0 - V\sigma_0}{kT}\right) \qquad \text{A. (26)}$$

Appendix IV: Johnson-Mehl-Avrami-Kolmogorov (JMAK) Model

The classical JMAK recrystallization model employs several important assumptions:

1. Nuclei are randomly distributed in the material.
2. Nucleation rate, $\dot{N}$, is constant during the course of recrystallization.
3. Nuclei grow into the deformed matrix with a constant growth rate $\dot{G}$.

Under these assumptions, the extended recrystallized volume fraction, V_{EX}, is readily calculated. This quantity is defined as the recrystallized volume fraction in the absence of any impingement effects and without taking account of the progressive consumption of the deformed material. It is simply calculated as:

$$V_{EX} = \int_0^t V\dot{N}dt' \qquad \text{A.}(27)$$

where, V is the volume of nuclei formed from t' to t. This could be expressed as: $f\dot{G}^3(t-t')^3$, where f is the shape factor ($4\pi/3$ for spheres). Thus:

$$V_{EX} = \int_0^t f\dot{G}^3(t-t')^3\dot{N}V_0dt' = \frac{f\dot{G}^3V_0t^4\dot{N}}{4} \qquad \text{A.}(28)$$

During the time interval *dt*, the extended volume increases by dV_{EX}. As the untransformed fraction of material is $1-X$, where the recrystallization fraction $X = V/V_0$, and then we have:

$$dV = (1-X)dV_{EX} \qquad A.(29)$$

$$V_{EX} = \int_0^{V_{EX}} dV_{EX} = \int_0^V \frac{dV}{1-\frac{V}{V_0}} = -V_0\ ln\left(1-\frac{V}{V_0}\right) \qquad \text{A.}(30)$$

Then,

$$\frac{V}{V_0} = 1 - exp\left(-\frac{V_{EX}}{V_0}\right) \qquad \text{A.}(31)$$

$$X = 1 - exp\left(-\frac{f\dot{N}\dot{G}^3t^4}{4}\right) \qquad \text{A.}(32)$$

which is the commonly used expression for the recrystallized fraction as a function of time under the assumption of constant nucleation and growth rate. Another interesting limiting case is that of site saturated nucleation, in which the nuclei are assumed to be present at time $t = 0$. In this case, the extended recrystallized volume fraction, V_{EX}, is given by:

$$V_{EX} = NV \qquad \mathrm{A}.(33)$$

where, N is the total number of nucleation sites per unit volume at time $t = 0$, and V is the volume of recrystallized grain, for a spherical grain, which is equal to

$$V = \frac{4\pi}{3}\dot{G}^3 t^3 \qquad \mathrm{A}.(34)$$

Using the same derivation described above, the actual recrystallized fraction is found to be:

$$X = 1 - exp\left(-\frac{4\pi N\dot{G}^3 t^3}{3}\right) \qquad \mathrm{A}.(35)$$

In practice, the JMAK equation is commonly written in the generalized form:

$$X = 1 - exp(-Bt^n) \qquad \mathrm{A}.(36)$$

Appendix V: Recovery Model Fitting

The recovery kinetics of each condition (various types of model alloys deformed at various temperatures) was fitted with Verdier's recovery model (initial solid portion) through the activation volume term [Eqs. (2-4) & (5-4)].

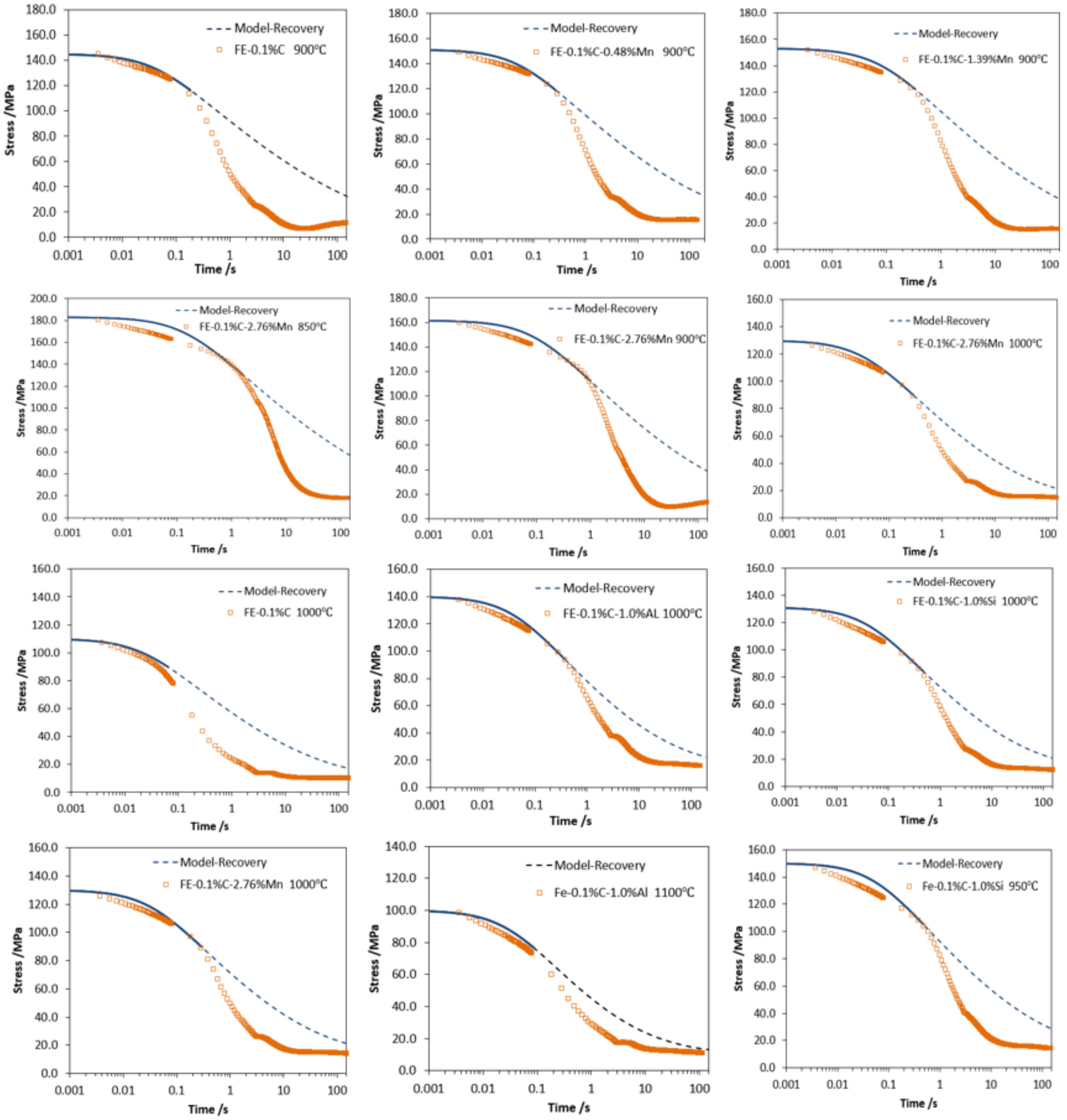

Fig. A2: Recovery data fitting using Verdier's recovery model for all testing conditions (alloy composition and annealing temperatures are shown respectively). The solid part of the recovery model predictions attempted to fit the experimental recovery data.

Appendix VI: Multi-pass Precipitation

The deformation & annealing scheme is shown in part A, while carbon replica examples of specified conditions in part B and precipitate number density estimated by STEM in part C, for multi-pass precipitation behavior investigation (Room-Temperature Deformation and Annealing).

Part A: Deformation & Annealing Scheme.

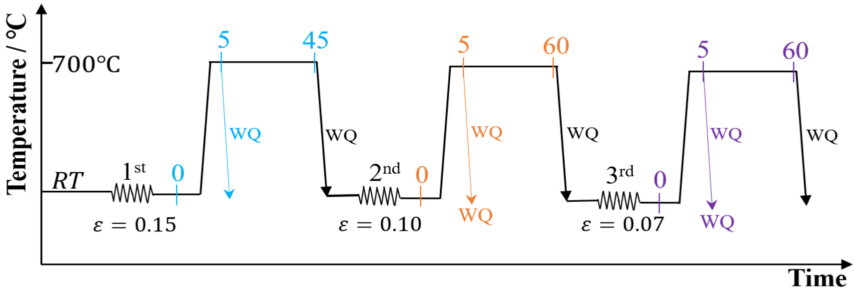

Fig. A3: Deformation and annealing conditions for three passes. Specimen was deformed at room temperature and annealed at 700°C for different times followed by quenching.

Part B: Carbon Replica Examples for All Conditions.

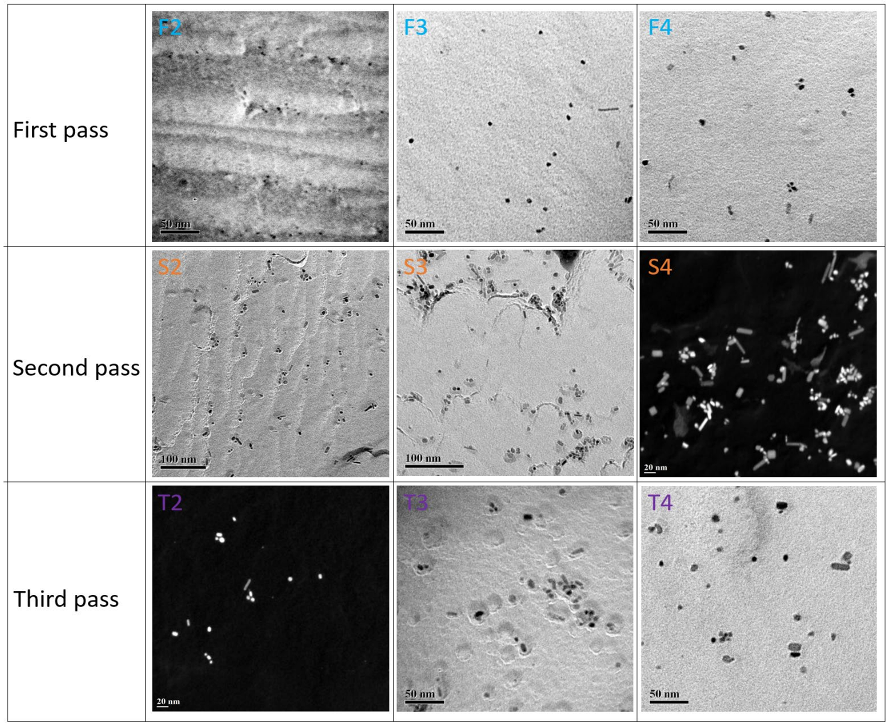

Fig. A4: Precipitate size measurements by carbon replica for all conditions (F2-F4, S2-S3, T3-T4) of three passes. The meaning of designations has been demonstrated in the context of the manuscript.

C: Number Density Calculation by TEM-STEM

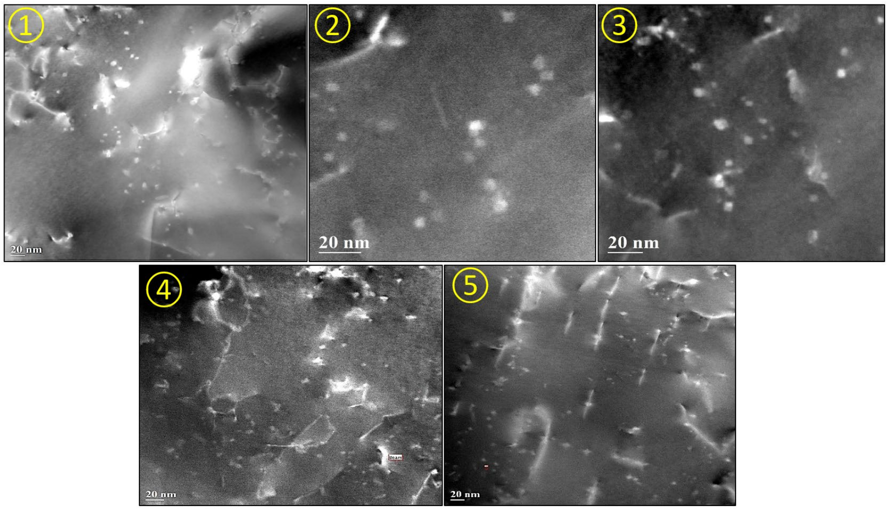

Fig. A5: NbC precipitates in STEM mode for position 1 to 5. The average thickness of the foil was measured to be about 75nm.

Table A1: Average number density and its standard deviation for all five estimated positions.

Position	**Number of particles**	**Number density /m^3**
1	175	1.46×10^{22}
2	30	2.26×10^{22}
3	40	2.06×10^{22}
4	187	1.56×10^{22}
5	205	2.64×10^{22}
Average number density:		2.00×10^{22}
Standard deviation:		0.49×10^{22}

Appendix VII: Two-pass Precipitation

The number density of precipitates was estimated by STEM, for two-pass precipitation behavior investigation (Hot-Deformation and Annealing).

Number Density Calculation by TEM-STEM

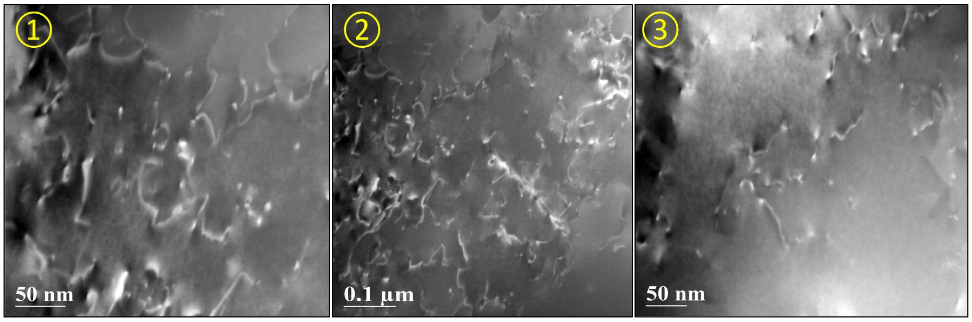

Fig. A6: NbC precipitates in STEM mode for position 1 to 3. The average thickness of the foil was measured to be about 75nm.

Table A2: Average number density and its standard deviation for all three estimated positions.

Position	Number of particles	Number density $/m^3$
1	90	1.16×10^{22}
2	252	0.87×10^{22}
3	75	0.62×10^{22}
Average number density:		0.88×10^{22}
Standard deviation:		0.27×10^{22}

Appendix VIII: Average Grain Size Estimation

The average grain size, GS_{ave}, of the partially-recrystallized material is approximately a volume average of the recrystallized grains and unrecrystallized portion of the deformed grain with respect to the recrystallization fraction X:

$$GS_{ave} = X \cdot GS_{rex} + (1 - X) \cdot GS_{unrex} \qquad \text{A.}(37)$$

For the unrecrystallized volume, we have

$$\frac{4}{3}\pi\left(\frac{GS_{unrex}}{2}\right)^3 = (1 - X) \cdot \frac{4}{3}\pi\left(\frac{D_0}{2}\right)^3 \qquad \text{A.}(38)$$

Then,

$$GS_{unrex} = (1 - X)^{\frac{1}{3}} \cdot D_0 \qquad \text{A.}(39)$$

Therefore,

$$GS_{ave} = X \cdot GS_{rex} + (1 - X)^{\frac{4}{3}} \cdot D_0 \qquad \text{A.}(40)$$

The approximation is relatively accurate due to the fact that laser signals are less sensitive to deformations (pancaking of grains and increase of dislocation density) at least for strains less than 0.35, as compared to the orientation change (more scattering to the laser signal) of those recrystallized volume during recrystallization. Thus, the spherical approximation of grain size evolution worked well with the laser-ultrasonics measurements.

Appendix IX: TMP Models Comparison and Advancement

A comparison was carried out between the laser-ultrasonics (LUS) measurements of grain size and thermomechanical processing models of Sellars [Eq. (1-57) & Eq. (1-58)], Rehman [Ph.D. Thesis, McMaster, 2013] and the current TMP models, with the C-Mn steel (in Chapter 5) deformed at 950°C and 1050°C with a strain of 0.25. As can be seen in Figs. A7(a) and (b), the Sellars' semi-empirical models matched TMP models well at 950°C, in terms of the recrystallized fraction; however, at 1050°C, both Rehman's and Sellars' models predicted faster kinetics compared to TMP models. TMP models were also compared to ArcelorMittal models, with their published modelling and experimental data of recrystallized fraction. The alloy chemistry and parameters were presented below in Fig. A7(c). Both models worked well with the experimental data. Other in-house models such as at Tata steel may also be used to compare such predictions if an access is possible. Overall, the current version of TMP models has been well developed and validated against in-situ stress relaxation tests and laser-ultrasonics measurements for grain size.

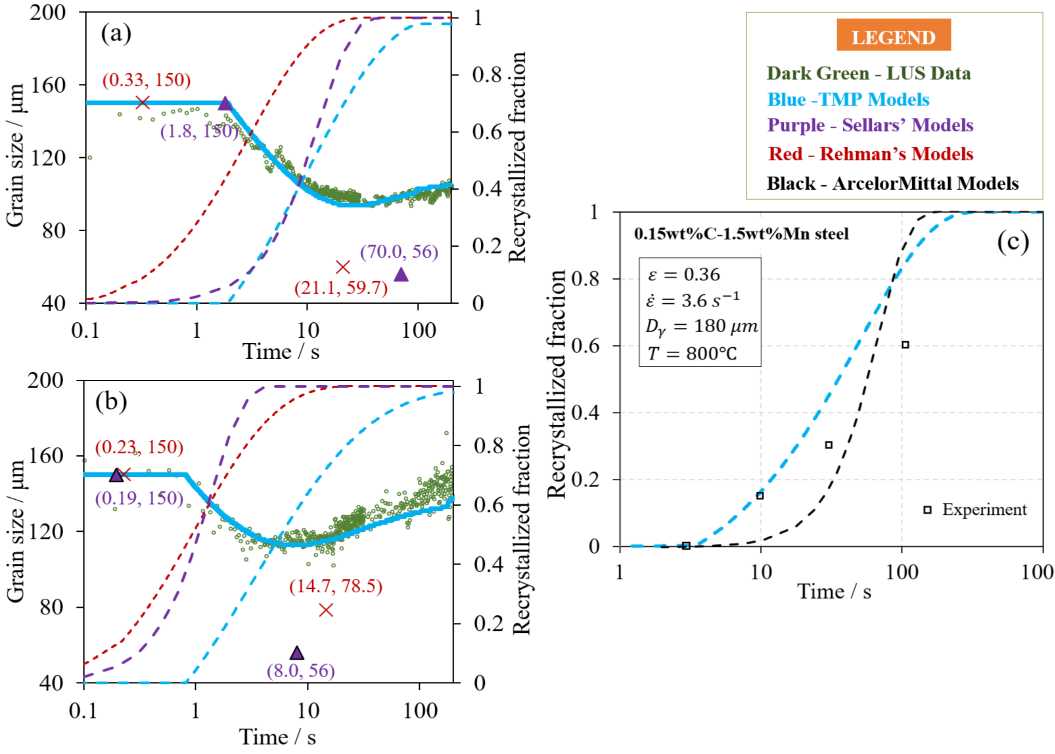

Fig. A7: Grain size evolution data by the laser-ultrasonics measurement as compared with model predictions from Sellars', Rehman's and TMP models at (a) 950℃ (b) 1050℃ of the C-Mn steel deformed to strain of 0.25; (c) comparison between TMP models and ArcelorMittal models.

Appendix X: Ultra-high Strength Steel Development

Taylor & Francis
Taylor & Francis Group

Ironmaking & Steelmaking
Processes, Products and Applications

ISSN: 0301-9233 (Print) 1743-2812 (Online) Journal homepage: https://www.tandfonline.com/loi/yirs20

Study of processing, microstructure and mechanical properties of hot rolled ultra-high strength steel

Tihe Zhou, David Overby, Peter Badgley, Chris Martin-Root, Xiang Wang, Shenglong Liang & Hatem Zurob

To cite this article: Tihe Zhou, David Overby, Peter Badgley, Chris Martin-Root, Xiang Wang, Shenglong Liang & Hatem Zurob (2019) Study of processing, microstructure and mechanical properties of hot rolled ultra-high strength steel, Ironmaking & Steelmaking, 46:6, 535-541, DOI: 10.1080/03019233.2018.1468652

To link to this article: https://doi.org/10.1080/03019233.2018.1468652

IRONMAKING & STEELMAKING
2019, VOL. 46, NO. 6, 535–541
https://doi.org/10.1080/03019233.2018.1468652

The Institute of Materials, Minerals and Mining
Taylor & Francis
Taylor & Francis Group

Study of processing, microstructure and mechanical properties of hot rolled ultra-high strength steel

Tihe Zhou[a], David Overby[a], Peter Badgley[a], Chris Martin-Root[a], Xiang Wang[b], Shenglong Liang[b] and Hatem Zurob[b]

[a]Research Department, Stelco Inc., Hamilton, ON, Canada; [b]Department of Materials Science and Engineering, McMaster University, Hamilton, ON, Canada

ABSTRACT

Hot rolled ultra-high strength steel with a gauge range of 3–10 mm (0.118″–0.395″) was developed using conventional slab caster and hot strip mill technology at Stelco Inc. (Stelco) to meet standard industry specifications along with additional unique customer requirements. The effects of chemical composition, steelmaking and hot rolling process parameters on microstructure, precipitation behaviour, and mechanical properties were studied. Both Grade 90 (620 Mpa, Stelco trademarked STELMAX^{TM}90) and Grade 100 (690 MPa, STELMAX^{TM}100) products met strength requirements in longitudinal and transverse directions. Furthermore, these ultra-high strength steels exhibited excellent ductility, impact toughness, edge stretchability and bendability. The enhanced mechanical properties are the results of chemistry design and carefully controlling austenite/ferrite grain size and precipitation behaviour at different processing stages. These newly developed steels have extensive applications in automobile safety components, light-weight construction, piping/tubing and offshore structures.

ARTICLE HISTORY
Received 14 March 2018
Accepted 18 April 2018

KEYWORDS
Ultra-high strength steel; microstructure; precipitation; mechanical properties; bendability; edge stretchability; toughness

Introduction

High strength low alloy steels (HSLA) that contain small amounts of alloy elements, including Ti, V or Nb, have been developed for many years and are widely used in modern industry [1,2]. Ultra-high strength steels (UHSS) are the next step forward in the development of higher strength steels. The aim of these developments is for these steels to have superior strength-ductility balance as compared to conventional HSLA steels. UHSS encompasses several steel families including HSLA, Dual Phase, Complex Phase, Martensitic and Transformation Induced Plasticity Steel. The designation of UHSS is arbitrary due to the fact that there is no universally accepted strength level for this class of steels [3]. However, according to ASTM A1011 and A1018 specifications, steels with yield strength of at least 620 MPa (90 ksi) and tensile strength of more than 690 MPa (100 ksi) are considered to be UHSS. In recent years, great efforts have been put into the development of UHSS for applications within the automotive and structural sectors with end products being truck frames, crane booms and frames, lift brackets and piping/tubing. The higher strength of UHSS, which is utilised in lightweight structures, can reduce structure costs, and increase the service life of the devices, as well as improve the devices' performance together with reducing environmental impacts [4,5].

UHSS are conventionally manufactured from hot rolled strip/plate by reheating, quenching and tempering. For safety-critical components, some customers require that the steel must meet minimum yield strength in both longitudinal and transverse directions while exhibiting good ductility, toughness, edge stretchability and bendability. Stelco has successfully achieved hot rolled ultra-high strength levels for a gauge range of 3–10 mm (0.118″–0.395″). Using the successful developments of STELMAX^{TM}90 and STELMAX^{TM}100 will also help Stelco to develop hot roll higher strength UHSS with minimum yield strength of 760 MPa (STELMAX^{TM}110) and 830 MPa (STELMAX^{TM}120).

Chemistry design

The chemistry design of UHSS is a critical part of meeting the required strength levels necessary to optimise the contributions of each strengthening mechanism while balancing weldability, bendability, toughness and edge stretchability. The yield strength σ_y of microalloyed steels is derived from the strengthening mechanisms including solid solution strengthening (σ_{ss}), precipitation strengthening (σ_p), dislocation hardening (σ_d), transformation strengthening (σ_{tr}) and grain size refinement (σ_{gs}). The relationship between yield strength and these strengthening mechanisms can be summarised as [6,7]:

$$\sigma_y = \sigma_i + \sigma_{ss} + \sigma_p + \sigma_d + \sigma_{tr} + \sigma_{gs} \qquad (1)$$

where σ_i is between 40 and 74 MPa at 273 K [6]. The principal strengthening mechanisms in microalloyed steels were assumed to be mainly grain refinement, solid solution strengthening and precipitation strengthening [7,8]. It has been well established that, of all the above of strengthening mechanisms, only finer grain size can increase both strength and toughness in microalloyed steels. It has also been suggested that a bimodal grain size distribution is the best strategy to optimise both strength and ductility in low alloy steels [9]. Solid solution strengthening is introduced by substitutional and interstitial elements such as Mn, Mo, Cr, Ni, Si, N and C; however, in order to improve weldability and formability, C concentration is typically restricted to 0.09% maximum.

CONTACT Tihe Zhou tom.zhou@stelco.com

Table 1. Chemical composition of STELMAX^{TM}90, 100 and 110.

Max (wt-%)	C	Mn	P	S	Si	V	Cb	Ti	Al	Ca	Mo/Cr/Ni
STELMAX^{TM}90	0.08	1.50	0.020	0.005	0.25	0.01	0.08	0.08	0.07	0.01	0.10
STELMAX^{TM}100	0.09	2.00	0.020	0.005	0.30	0.01	0.09	0.12	0.07	0.01	0.15
STELMAX^{TM}110*	0.09	2.00	0.020	0.005	0.30	0.01	0.09	0.12	0.07	0.01	0.25

*STELMAX^{TM}110 is in the trial stage.

Precipitation strengthening is realised by the addition of Ti and Nb in combination with C and N to form complex precipitates Ti(N,C) and Nb(N,C). To prevent precipitating large TiN particles at high temperature, which might damage bendability and edge stretchability, N is often limited to 0.007% maximum. Ca is also added to modify inclusion shape for improved formability. A comparison of chemistry design for different UHSS grades is listed in Table 1.

Processing parameters

Steelmaking and casting process

All UHSS grades developed at Stelco utilise 260 ton basic oxygen furnaces (BOF), combining molten iron with scrap steel and other required alloys. Before molten iron is transferred to the BOF vessel, *Hot Metal Rotary Lance Desulphurization* technology is used to improve ultra-low sulphur capability for UHSS. The concentration of sulphur is controlled to under 0.005% which is essential to reduce the volume of inclusions and to improve slab internal quality. The liquid steel is further refined using both *RHOB Vacuum Degasser* and a *Ladle Treatment Station* to remove hydrogen form the liquid steel and to ensure temperature and chemical homogeneity. The hydrogen concentration is between 0.0001 and 0.0002% which would eliminate hydrogen embrittlement for our UHSS grades.

After liquid conditioning, the steel is cast in a curved mould, twin strand continuous caster. Stelco's caster is capable of casting high alloy grades due to its split roll design (for segments from 4 to 14) and its air mist cooling. The solidified slabs are torch cut to length according to customer requirements. All UHSS slabs are stack cooled indoors with slow cooling rate to prevent slab cracking and slabs have to be conditioned before being transferred to hot strip rolling.

Reheating, thermomechanical processing and coiling

The first step of thermomechanical processing is to reheat the slab to the desired temperature. The reheating temperature has to balance the dissolution of microalloy particles (formed during the solidification of the casting process) and controlling austenite grain coarsening. In order to prevent excessive austenite coarsening inside during reheating, Ti is added to retard austenite grain growth. According to the solubility of Nb and Ti in UHSS, the reheating furnace temperature is set between 1250 and 1280°C for both STELMAX^{TM}90 and 100 products to avoid abnormal grain growth [10]. After reheating, the slab is fed into a reversing rougher mill where the slab is reduced from the original slab thickness to a predetermined transfer bar thickness. This reduction is typically performed in seven roughing passes and is designed to refine austenite grain size. Stelco utilises a coil box between the roughing and finishing mills. This unique step in the hot rolling process promotes a homogeneous austenite grain microstructure and uniform temperature profile from head to tail and from edge to edge before entering the finishing mill. The six-stand finishing mill further refines austenite grains and produces 'pancake' austenite grains which are essential to refine alpha ferrite during the austenite to ferrite phase transformation. In addition, controlling finishing and coiling temperatures within-coil and from coil to coil is also important to ensure consistent mechanical properties. For heavy gauge products, coiling temperature is typically reduced to improve mechanical property capability.

Microstructure

Examples of optical microstructures taken of STELMAX^{TM}90 and 100 (at 3.20 and 6.20 mm thickness) are summarised in Figures 1 and 2, respectively. Both microstructures are

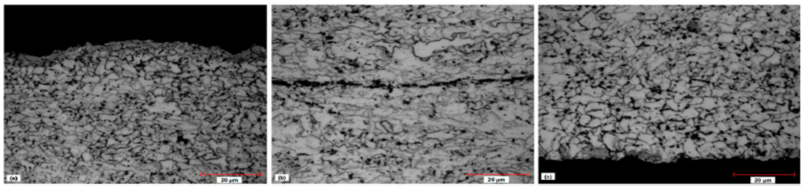

Figure 1. Microstructure of STELMAX^{TM}90 at (a) top surface, (b) centreline and (c) bottom. Etched using 3% nital.

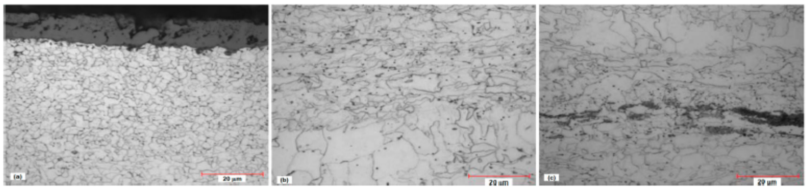

Figure 2. Microstructure of STELMAX^{TM}100 at (a) top surface, (b) quarter thickness and (c) centreline. Etched using 3% nital.

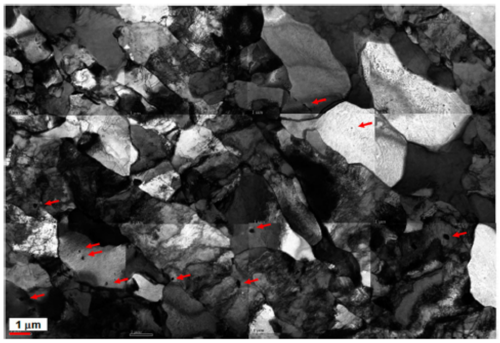

Figure 3. TEM thin-foil montage images of ferrite and precipitated particles in STELMAX^{TM}100.

composed of equiaxed ferrite, carbides and complex precipitates. The white microstructure component is ferrite and the dark particles are precipitates and carbides. STELMAX^{TM}90 exhibited an uniform grain size about 3.3 μm from the top surface to bottom. STELMAX^{TM}100 showed around 1 μm grain size at the surface and approximately 7.9 μm grain size at the quarter position.

To obtain a clear impression of finer ferrite morphology, TEM bright-field was used to characterise STELMAX^{TM}100 microstructure. Figure 3 indicated that ferrite grain size is in the range of 1 μm to several micrometren and fine precipitated particles (marked by arrow) are homogeneously and randomly distributed along the grain boundaries and inside the grain. The very fine ferrite grain size is the results of austenite deformation and recrystallisation, and precipitation of carbides and nitrides occurring at different processing stages. These small ferrite grain sizes in both STELMAX^{TM}90 and 100 confirmed that the importance of grain size as a method to increase strength in UHSS as described in Equation (1).

Micro-cleanness and centreline segregation

Internal cleanness was measured on as-hot rolled samples according to ASTM E45, using image analysis. The ratings of non-metallic inclusions of STELMAX^{TM}90 and 100 are listed in Tables 2 and 3, respectively. Both grades were deemed to be clean, with a maximum rating of 1.0 for any inclusion type.

The centreline of both grades appeared to show a measure of chemical segregation (Figures 1(b) and 2(c)). However, energy dispersive spectroscopy (EDS) mapping at the steel strip centre position was unable to resolve the chemical segregation within its detection limits (Figure 4). Instead of distinguishing a gradient of chemical composition, titanium nitrides and a niobium-rich phase were detected. However, these particles do indicate segregation occurred during the solidification process.

Precipitation behaviour

UHSS ferrite grain refinement is achieved by two mechanisms: fine recrystallised austenite grains formed during hot rolling at intermediate temperatures and precipitation after the austenite to ferrite phase transformation. To investigate precipitation behaviour at different stages during the process, samples were taken after roughing and after coiling. The roughing sample was taken from a 34 mm transfer bar air cooled from around 1100°C down to room temperature. An extraction replica technique was used to examine the precipitate particles. The replicas were examined on a PHILIP CM 12 and a JEOL 2010F electron microscope equipped with an EDS X-ray spectrometer.

The morphology and size of precipitates in STELMAX^{TM}100 roughing and coiling samples at different magnifications are shown in Figures 5 and 6, respectively. Figure 5 indicates that there are very few fine precipitates after roughing and coarse particles (average particle size 71 nm) are uniformly distributed with square/quasi-square and irregular shapes. These coarse particles are the result of slow cooling of the transfer bar. However, in spite of uniformly distributed coarse precipitates in coiling samples (average particle size 65 nm), non-uniform distributed nanoscale precipitates (average particle size 4.3 nm) with square or quasi-square shape (Figure 6(b)) and local area interphase precipitates with row arrangement (Figure 6(c)) were observed at high magnification.

Precipitation of carbides and nitrides occurs at each stage of processing UHSS grades. To better understand precipitation behaviour, examples of large, medium and fine non-uniform distributed particles and their EDS analysis from STELMAX^{TM}100 coiling samples are summarised in Figure 7 accordingly (the Cu peaks in all spectra are from the replica holder and high C peaks are partially from C film). During the casting process, TiN particles may precipitate in the liquid phase (although this is undesirable), at the liquid/solid interface and in delta ferrite and austenite. These types of particles are shown in Figures 5 and 6(a). Figure 7(a,b) suggests that these coarse particles are rich in higher concentration of Ti and Nb. These precipitates are very stable and can effectively retard austenite coarsening during the reheating process [6,11]. After reheating, and

Table 2. Cleanness summary of STELMAX^{TM}90.

ASTM E45	Sulphide		Alumina		Silicate		Globular oxide	
Id	Thin	Heavy	Thin	Heavy	Thin	Heavy	Thin	Heavy
1	1.0	0	0.5	0	0	0	0	0
2	0.5	0	0.5	0	0	0	0	0

Table 3. Cleanness summary of STELMAX^{TM}100.

ASTM E45	Sulphide		Alumina		Silicate		Globular oxide	
Id	Thin	Heavy	Thin	Heavy	Thin	Heavy	Thin	Heavy
1	0.5	0	0	0	0	0	0	0
2	1.0	0	0	0	0	0	0.5	0

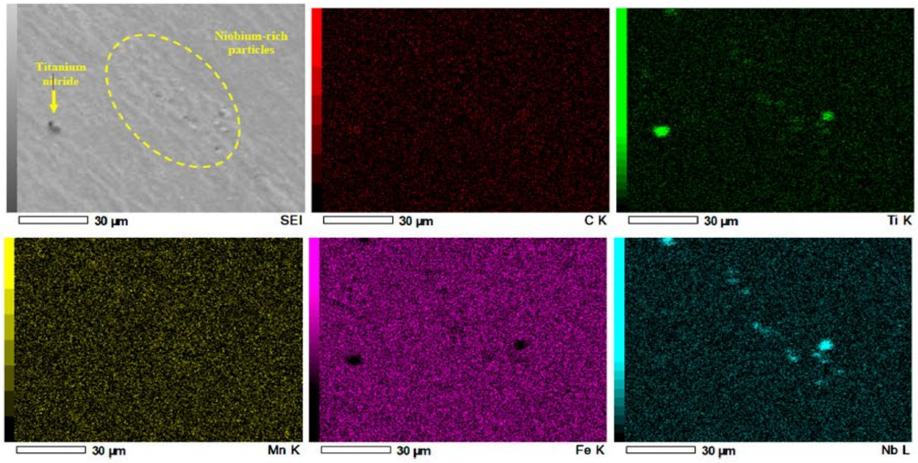

Figure 4. EDS maps taken at the centreline segregation of STELMAX^{TM}100. SE1, 15 kV.

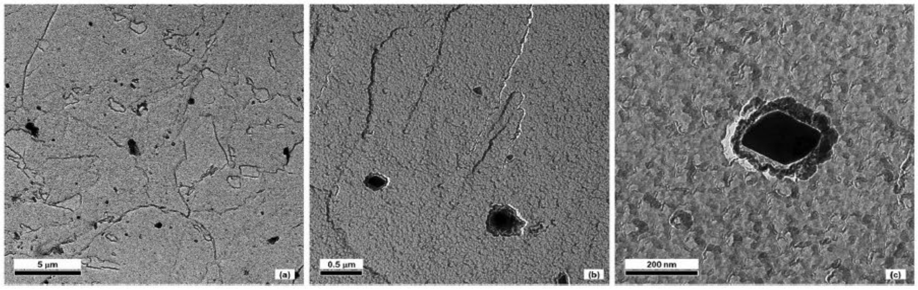

Figure 5. Precipitation behaviour after roughing STELMAX^{TM}100 (a) low magnification, (b) high magnification and (c) morphology of large particle.

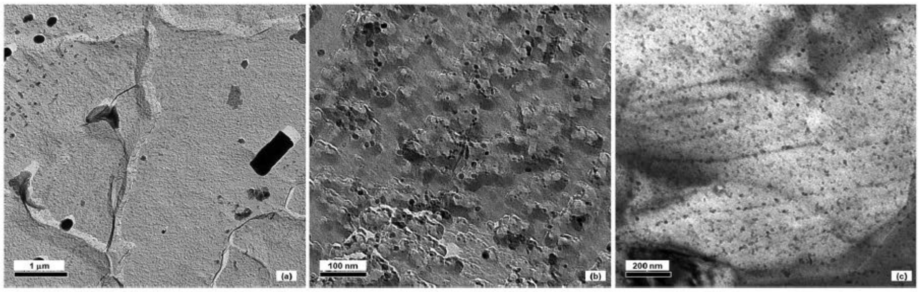

Figure 6. Precipitation behaviour after coiling STELMAX^{TM}100 (a) large particles, (b) fine non-uniform distributed particles and (c) interphase precipitation.

during roughing and finishing, complex precipitates (Ti, Nb)(C,N), Nb(C,N) are formed. These precipitates are strain induced and can refine austenite grain size and retard the recrystallisation of austenite. Figure 6(b) shows this type of precipitates. Figure 7(d,f) indicates medium and fine precipitates are rich in high concentration of Ti, Nb and Mo. Grain refinement of UHSS is primarily due to this group of particles. As acknowledged by Baker [6], large Ti–Nb particles with many smaller Nb-rich spheroids is the result of caps nucleating on more stable core precipitates. The epitaxial growth would obviate the need for strain induced mixed carbides, thus the increase in the volume fraction of precipitates can increase particle pinning force on boundary mobility, thereby retarding recrystallisation. After processing through the finishing mill, finer particles are formed during or after the austenite to ferrite phase transformation, on the austenite/ferrite interface and in ferrite. Dispersion strengthening (σ_p) in ferrite normally occurs through these changes, and a fine precipitate dispersion in STELMAX^{TM}100 is observed as shown in Figure 6(b,c). These finer

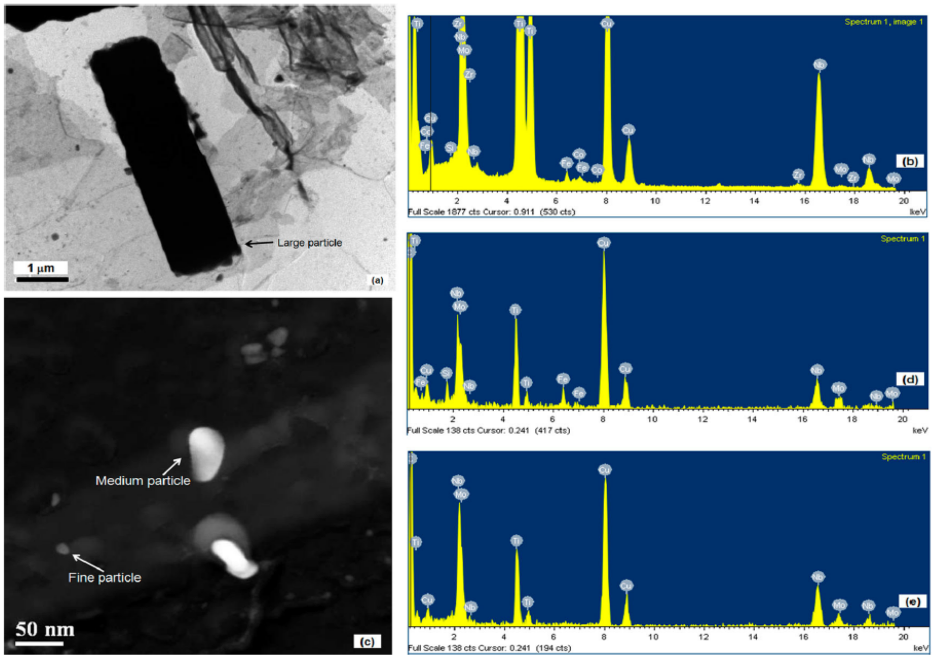

Figure 7. Precipitation EDS analysis after coiling STELMAX^{TM}100 (a) large particles, (b) EDS analysis of large particle, (c) medium and fine non-uniform distributed particles, (d) EDS analysis of medium particles and (e) EDS analysis of fine particles.

precipitates also can retard ferrite grain growth to achieve high strength with enhanced impact toughness.

Mechanical properties

Tensile properties

As-hot rolled mechanical properties for Stelco's UHSS grades met ASTM A1011 and A1018 specifications. Results are summarised in Tables 4 and 5. Both yield and tensile strength met the minimum requirement in both longitudinal and transverse directions. Elongation also easily met specification in longitudinal and transverse directions for both grades. In addition, the minor difference between longitudinal and transverse performance of elongation can be attributed to effective clean steel practices developed at Stelco.

Toughness

There is no toughness requirement for UHSS in either ASTM A1011 or A1018. However, some customers demand low-temperature toughness performance depending upon their application. Charpy V-notch (CVN) impact testing was conducted according to ASTM-E23. STELMAX^{TM}100 CVN curves for both longitudinal and transverse directions are shown in Figure 8. For each coil sample tested, the average absorbed energy value increased gradually from the lowest to the highest temperature. The CVN impact energy in L-direction at −45°C is about 40 J and about 30 J in the T-direction for half size samples. This high CVN absorbed energy is the result of fine ferrite grain size [6]. It is difficult to define a ductile to brittle transition as the reduction in CVN energy with lower temperature is quite gradual.

Table 4. STELMAX^{TM}90 mechanical properties.

		Yield strength		Tensile strength		Elongation (%)
Gr90 ASTM specification		Min 90ksi	Min 620MPa	Min 100ksi	Min 690Mpa	Min 16%
T-direction	Average	100	691	109	755	19
	Min–Max	97–103	667–708	107–110	738–760	18–20
L-direction	Average	97	669	107	737	20
	Min–Max	92–102	634–700	103–110	710–758	18–23

Table 5. STELMAX^{TM}100 mechanical properties.

		Yield strength		Tensile strength		Elongation (%)
Gr100 ASTM specification		Min 100ksi	Min 690Mpa	Min 110ksi	Min 760Mpa	Min 14%
T-direction	Average	110	759	120	828	21
	Min–Max	101–117	695–810	111–126	766–872	20–22
L-direction	Average	105	724	117	809	22
	Min–Max	101–110	699–756	111–124	771–852	21–23

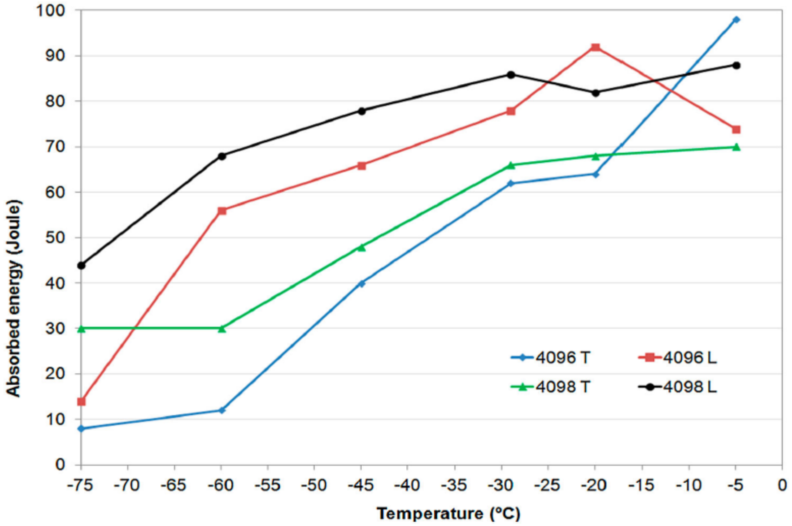

Figure 8. STELMAX^{TM}100 CVN impact energy curve.

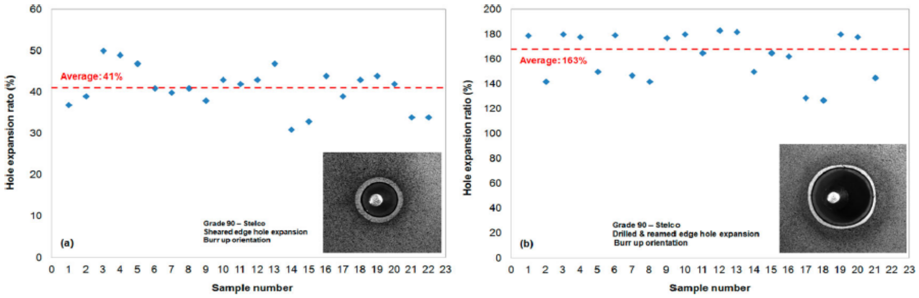

Figure 9. Summary of STELMAX^{TM}90 hole expansion test (a) sheared edge and (b) drilled edge.

Edge stretchability

Edge stretchability refers to a sheet's ability to resist edge cracking during complex shape forming and flanging. Edge stretchability is typically evaluated by measuring Hole Expansion Ratio (HER) with a hole expansion test [12,13]. Samples were prepared according to ISO/TS 16630, and testing was recorded using a Digital Image Correlation measurement system. Along with standard sheared edge samples, a group with drilled and reamed holes was tested (Figure 9). Note the significant increase in edge stretch capability of a machined edge compared to a punched edge. The average HER of sheared edge samples is 41%; however, the average of HER for a machined edge is 163%. The high value of HER for both sheared and drilled edges is due to the fact that STELMAX^{TM}90 has fine ferrite grain size and fine precipitates as shown in Figures 1, 2 and 6(b,c).

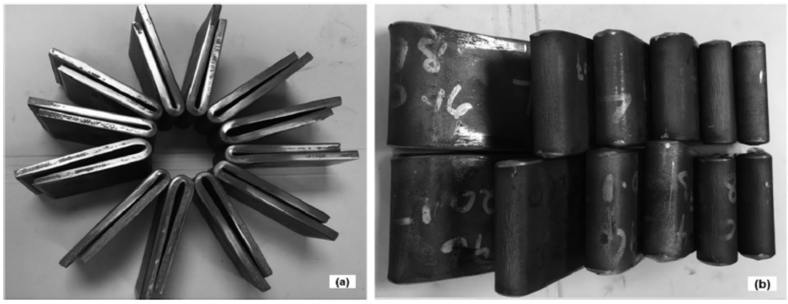

Figure 10. Summary of STELMAX^{TM}100 bending test (a) 180° degree bending (b) bending surface.

Bendability

High strength and formability are typically incompatible, i.e. as the strength increases, formability decreases [6,9]. Most applications for UHSS grades do not demand excellent formability, but there may be significant bending requirements. To determine UHSS ductility, bend strength and resistance to fracture, 12 samples were taken from STELMAX^{TM}100 (thickness 6.20 mm) in both longitudinal and transverse directions. Bend testing was conducted according to ASTM E290. Samples were bent flat on themselves. Bend test results are shown in Figure 10. There was no indication of cracking in either longitudinal or transverse directions (Figure 10(b)). Stelco's UHSS grades have high strength with good formability.

Stelco's STELMAX^{TM}90 and 100 with improved mechanical properties have been extensively utilised in automobile safety components, lift brackets and piping/tubing. They have the potential to replace heat treated material without compromising component performance. These successful developments will be used as a guide to develop even higher strength UHSS grades (i.e. STELMAX^{TM}110 and STELMAX^{TM}120).

Summary

(i) The chemistry design of UHSS is based on the grade and customer specifications to optimise the contributions of each strengthening mechanism. Solid solution strengthening is introduced by Mn, Si, C, Mo and Cr; precipitation strengthening is realised by Ti and Nb additions; and grain refinement is the contribution of solid solution and precipitate strengthening. Careful control of processing parameters through steelmaking, casting, reheating and rolling, along with controlling finishing and coiling temperatures are essential to consistently meet mechanical property requirements.

(ii) Both STELMAX^{TM}90 and 100 show ultra-fine ferrite grain size with complex precipitates. Ferrite refinement is a result of fine recrystalliszed austenite grains formed by hot rolling at intermediate temperatures, while ferrite grain growth is retarded by fine precipitates formed after the austenite to ferrite phase transformation.

(iii) TiN particles precipitated during the casting process can effectively retard austenite coarsening during reheating. Ti and Nb complex particles are strain induced and can refine austenite grain size and retard the recrystallisation of austenite during roughing and finishing. Finer, complex particles formed during or after the austenite to ferrite phase transformation further dispersion strengthen the ferrite.

(iv) Stelco's new STELMAX^{TM}90 and 100 show an excellent combination of high strength, ductility, impact toughness, edge stretchability and bendability.

Acknowledgements

The authors acknowledge the Canadian Centre for Electron Microscopy (CCEM) at McMaster University, Hot Strip Mill Operation Team and Quality Assurance Department at Stelco Inc. (Nanticoke, ON, Canada).

Disclosure statement

No potential conflict of interest was reported by the authors.

ORCID

Tihe Zhou http://orcid.org/0000-0002-0452-5520

References

[1] Gladman T. The physical metallurgy of microalloyed steel. London: Institute of Materials; 1997; P. 1–19.

[2] DeArdo AJ. Niobium in modern steels. Int Mater Rev. 2003;46(6):371–402.

[3] Chatterjee D. Behind the development of advanced high strength steel (AHSS) including stainless steel for automotive and structural applications – an overview. Mater Sci Metall Eng. 2017;4(1):1–15.

[4] Keeler S, Kimchi M. Advanced high strength steels application guidelines version 5.0. 2014; 1–276. Available at: http://www.autosteel.org.

[5] Klein M, Spindler H, Luger A, et al. Thermomechanically hot rolled high and ultra high strength steel grades – processing, properties and application. Mater Sci Forum. 2005;500–501:543–550.

[6] Baker TN. Microalloyed steels. Ironmak Steelmak. 2016;43(4):264–307.

[7] DeArdo AJ. Metallurgical basis for thermomechanical processing of microalloyed steels. Ironmak Steelmak. 2001;28(2):138–144.

[8] Vervynckt S, Verbeken K, Lopez B, et al. Modern HSLA steels and role of non-recrystallisation temperature. Int Mater Rev. 2012;57:187–207.

[9] Wang TS, Li Z, Zhang B, et al. High tensile ductility and high strength in ultrafine-grained low-carbon steel. Mater Sci Eng A. 2010;527:2798–2801.

[10] Zhou T, Zurob H. Abnormal and post-abnormal austenite grain growth kinetics in Nb-Ti microalloyed steels. Can Metall Q. 2011;50(4):389–395.

[11] Zhou T, Zurob H, Fox M. Austenite grain coarsening behavior in V-Ti microalloyed steels during reheating process. *Contributed Papers from Materials Science & Technology 2017*, Paper presented at MS&T17, Pittsburgh (PA). Warrendale (PA): Materials Science & Technology; P. 811–818;2017.

[12] Chen L, Kim JK, Kim SK, et al. Stretch-flangeability of high Mn TWIP steel. Steel Res Int. 2010;81:552–568.

[13] Yoon JI, Jung J, Kim JG, et al. Key factors of stretch-flangeability of sheet materials. J Mater Sci. 2017;52:7808–7823.